

UNIVERSITÉ DU QUÉBEC À TROIS-RIVIÈRES

EFFET DE LA MICROSTRUCTURE, MORPHOLOGIE ET
VARIATIONS CHIMIQUES DANS LES ALLIAGES
DE TYPE TIFE POUR LE STOCKAGE DE L'HYDROGÈNE

*EFFECT OF MICROSTRUCTURAL, MORPHOLOGICAL AND CHEMICAL
VARIATIONS ON TIFE-BASED ALLOYS FOR HYDROGEN STORAGE*

THÈSE PRÉSENTÉE
COMME EXIGENCE PARTIELLE DU
DOCTORAT EN SCIENCES DE L'ÉNERGIE ET DES MATÉRIAUX

PAR
ELENA ROSEMARIE ULATE KOLITSKY

MARS 2022

Université du Québec à Trois-Rivières

Service de la bibliothèque

Avertissement

L'auteur de ce mémoire ou de cette thèse a autorisé l'Université du Québec à Trois-Rivières à diffuser, à des fins non lucratives, une copie de son mémoire ou de sa thèse.

Cette diffusion n'entraîne pas une renonciation de la part de l'auteur à ses droits de propriété intellectuelle, incluant le droit d'auteur, sur ce mémoire ou cette thèse. Notamment, la reproduction ou la publication de la totalité ou d'une partie importante de ce mémoire ou de cette thèse requiert son autorisation.

UNIVERSITÉ DU QUÉBEC À TROIS-RIVIÈRES

DOCTORAT EN SCIENCES DE L'ÉNERGIE ET DES MATÉRIAUX (PH. D.)

Direction de recherche :

Jacques Huot Directeur de recherche

Bernard Tougas Codirecteur de recherche

Jury d'évaluation de la thèse :

Jacques Huot Directeur de recherche

Bernard Tougas Codirecteur de recherche

Jacques Goyette Président de jury

Jean-Louis Bobet Évaluateur externe

Young Whan Cho Évaluateur externe

Thèse soutenue le 23 février 2022.

“Yes, my friends, I believe that water will one day be employed as fuel, that hydrogen and oxygen which constitute it, used singly or together, will furnish an inexhaustible source of heat and light, of an intensity of which coal is not capable.”

– Jules Verne

ACKNOWLEDGEMENTS

First, I would like to thank Professor Jacques Huot, for being direct and tough, helping me learn how to be well informed in order to discuss my results and defend my point of view with one of the best in the field. I also want to express my sincere gratitude to Dr. Bernard Tougas, for his input and encouragement during my PhD. Also, for allowing me to work as an intern at the CMQ making, the past 3 year an exciting challenge. I would like to thank Dr. Renato Strozi, who helped me a lot when I started my PhD his friendship is one, I hold near and dear. I would like to thank all my colleagues that are and were part of the Huot's lab team who made coming to the lab fun and supported my mild caffeine addiction by always being available for a quick coffee run. I wish to thank my friends that made the trip up north (Nazareth, Mauricio and Veronica) your time here was truly appreciated, and I miss you all. I am also very thankful for my family, my parents two of the smartest people I know, my sister and her boyfriend who laugh at my stupid jokes and allow me to third wheel their life in general. My biggest thanks goes to Dr. Alvaro Macias who has been my #1 supporter and is off doing great things. I am so proud of you (and so is everyone else that knows you).

Last but definitely not least, to Dr. Michael Kolitsky who inspired me when I was only 8 years old. We had a 2-hour chat about the Human Genome Project, I confess, I did not understand much but I realized then and there I wanted to be as passionate about learning and discovering new things as he was and still is.

RÉSUMÉ

Ce projet se concentre sur l'amélioration de la cinétique de la première hydrogénation (activation) des alliages à base de TiFe. Plusieurs façons d'améliorer l'activation ont été étudiées. Premièrement, une méthode de synthèse industrielle, l'atomisation au gaz, a été utilisée pour déterminer si cette technique de synthèse pouvait générer un alliage à base de TiFe qui serait capable de s'activer à la température de pièces sous faible pression d'hydrogène. L'atomisation au gaz a été réalisée par le partenaire industriel GKN. L'atomisation au gaz est utilisée dans la métallurgie des poudres, mais en raison de son coût, elle n'était pas utilisée auparavant dans le développement d'alliages à base de TiFe pour le stockage de l'hydrogène. Deux compositions ont été atomisées au gaz, mais seuls les résultats pour TiFe + 2 % en poids de Mn + 4 % en poids de Zr sont présentés en raison des accords de confidentialité avec GKN. La poudre atomisée a été caractérisée, traitée mécaniquement et activée. La poudre atomisée présentait une microstructure extrêmement fine par rapport à son homologue produit par induction. À partir de ces résultats et de la comparaison avec des études antérieures, il a été conclu que l'atomisation au gaz est un bon candidat pour produire des alliages à base de TiFe qui présentent une bonne cinétique et une bonne capacité après exposition à l'air. De plus, le laminage à froid s'est avéré plus efficace que le broyage à billes en tant que technique de traitement régénératif pour les alliages TiFe exposés à l'air.

Une autre approche qui a été étudiée était l'effet du Ti surstœchiométrique sur TiFe + 4 % en poids de Zr. Les échantillons ont été produits par fusion à l'arc avec de petites variations sur le contenu en Ti, Ti_xFe_{2-x} + 4 % en poids Zr ($x = 1,1, 1,15, 1,2$). Toutes les compositions étudiées formaient des systèmes triphasiques avec une matrice TiFe, une phase de type Ti_2Fe et une phase cubique à corps centré riche en Ti. L'effet des phases secondaires sur la cinétique d'activation et la capacité réversible a été étudié. Le comportement d'hydrogénation de la phase de type Ti_2Fe n'avait pas été précédemment rapporté en raison de sa difficulté à être synthétisée. Toutes les phases ont formé des hydrures lors de l'activation. Cependant les phases secondaires ont formé des hydrures

stables qui n'ont pas été désorbés dans les conditions expérimentales (température ambiante, 0.1 bar). La stœchiométrie de l'hydrure stable formé par la phase de type Ti_2Fe a été calculée et est comprise entre $Ti_2FeH_{2.8}$ et Ti_2FeH_4 . La capacité réversible a été entièrement attribuée à la phase $TiFe$. De plus, il a été déterminé que l'augmentation de la quantité relative de titane rend l'alliage plus stable en augmentant légèrement la teneur en Ti dans la phase $TiFe$.

Finalement, l'effet de la surstœchiométrie du Ti sans Mn ou Zr a été étudié par fusion par induction de la composition $Ti_{1.2}Fe_{0.8}$. L'alliage présentait un système triphasé d'une phase principale $TiFe$ et des phases secondaires de type Ti_2Fe et d'une phase cubique à corps centré riche en Ti. Cependant, l'alliage $Ti_{1.2}Fe_{0.8}$ a nécessité un laminage à froid pour obtenir l'activation, mais l'a fait avec une bonne cinétique atteignant la saturation en environ 6 heures à température ambiante et 20 bars. Les résultats du $Ti_{1.2}Fe_{0.8}$ fondu par induction ont été comparés à des études précédentes qui rapportaient les mêmes phases secondaires. Un petit échantillon de 3 grammes de $Ti_{1.2}Fe_{0.8}$ a été synthétisé par fusion à l'arc et activé sans avoir besoin de laminage à froid. Cela montre comment la microstructure obtenue par fusion par induction n'est pas aussi avantageuse que la microstructure plus fine obtenue par fusion à l'arc, mais est toujours capable de s'activer. On conclut que la différence de microstructure est la cause des problèmes d'activation de l'échantillon fondu par induction.

La section de travaux futurs décrit plusieurs directions que l'étude des alliages à base de $TiFe$ pourrait prendre en compte pour tirer pleinement des recherches présentées dans la thèse. La voie d'atomisation au gaz nécessiterait des collaborateurs industriels, mais si elle était bien faite, elle donnerait des résultats nouveaux et intéressants sur l'effet de la solidification rapide sur les propriétés d'hydrogénation du $TiFe$. Le développement de traitements thermiques pour les lingots fondus par induction de $TiFe$ afin d'obtenir une microstructure qui correspond à la cinétique d'activation des échantillons fondus à l'arc serait une voie très bénéfique dans l'avancement de la mise à l'échelle industrielle des résultats obtenus à partir de petites tailles d'échantillons en laboratoire.

ABSTRACT

This project focuses on the improvement of the first-hydrogenation (activation) kinetics of TiFe-based alloys. Several ways to improve activation were investigated. First, an industrial synthesis method, gas atomization was used to determine if this synthesis technique could generate a TiFe-based alloy that would be able to activate under mild conditions. Gas atomization was performed by the industrial partner, GKN. Gas-atomization is used in powder metallurgy but due to its cost it was not previously used in the development of TiFe-based alloys for hydrogen storage. Two compositions were gas-atomized. However only the results for TiFe + 2 wt.% Mn + 4 wt.% Zr are presented here due to confidentiality agreements with GKN. The atomized powder was characterized, mechanically processed, and activated. The atomized powder presented an extremely refined microstructure compared to its induction-melted counterpart. Based on the results and the comparison with previous work it was concluded that gas-atomization is a good candidate to produce TiFe-based alloys that present good kinetics and capacity after air exposure. In addition, cold rolling was shown to be more effective than ball milling as a regeneration processing technique for air-exposed TiFe alloys.

Another approach that was studied was the effect of overstoichiometric-Ti on TiFe + 4 wt.% Zr. The samples were produced by arc-melting with small variations on the Ti content, $Ti_xFe_{2-x} + 4 \text{ wt.}\% \text{ Zr}$ ($x = 1.1, 1.15, 1.2$). All compositions studied formed three phase systems with a TiFe matrix a Ti_2Fe -like phase and a Ti-rich BCC phase. The effect of the secondary phases on the activation kinetics and reversible capacity was studied. The hydrogenation behavior of the secondary phases specifically the Ti_2Fe -like phase had not been previously reported due to its difficulty to be synthesized. All phases formed hydrides during activation. However, the secondary phases formed stable hydrides that were not desorbed under the experimental conditions (room temperature, 0.1bar). The stoichiometry of the stable hydride formed by the Ti_2Fe -like phase was calculated to be between $Ti_2FeH_{2.8}$ and Ti_2FeH_4 . The reversible capacity was fully attributed to the TiFe

phase. Additionally, it was determined that increasing the relative amount of titanium makes the alloy more stable by slightly increasing the Ti content in the TiFe phase.

Lastly, the effect of Ti overstoichiometry on TiFe without Mn or Zr was studied by induction-melting the composition $\text{Ti}_{1.2}\text{Fe}_{0.8}$. The alloy also presented a three-phase system of a main TiFe phase and secondary Ti_2Fe -like phase and a Ti-rich BCC. However, this alloy required cold rolling to achieve activation but did so with good kinetics reaching saturation in ~ 6 h at room temperature and 20 bar. The results of the induction melted $\text{Ti}_{1.2}\text{Fe}_{0.8}$ were compared to previous studies that reported similar secondary phases. A small 3-gram sample of $\text{Ti}_{1.2}\text{Fe}_{0.8}$ was synthesized by arc-melting and activated without the need for cold rolling. This shows how the microstructure obtained by induction melting is not as advantageous as the finer microstructure obtained by arc-melting but is still able to activate under mild conditions. The different microstructure is thought to be the cause for the activation issues of the induction-melted sample.

The future work section describes several directions that the study of TiFe-based alloys could go in to take full advantage of the research presented in the thesis. The gas-atomization route would require industrial collaborators but if done well would yield new and exciting results on the effect of rapid solidification on the hydrogenation properties of TiFe. Finally, the author's perspective on the direction of TiFe research is discussed and the importance of the reversible capacity from an industrial point of view.

TABLE OF CONTENTS

ACKNOWLEDGEMENTS	iv
RÉSUMÉ	v
ABSTRACT	vii
LIST OF TABLES	xii
LIST OF FIGURES	xiii
SECTION A	
CHAPTER I	
INTRODUCTION	2
1.1 Hydrogen storage.....	2
1.2 Metal Hydrides	3
1.2.1 Thermodynamics	5
1.2.2 Types of interstitial hydrides	6
1.3 TiFe.....	8
1.4 Research goals	11
1.5 Thesis structure.....	11
CHAPTER II	
EXPERIMENTAL DETAILS	13
2.1 Synthesis methods	13
2.1.1 Arc-melting.....	13
2.1.2 Gas-atomization.....	14
2.1.3 Induction melting.....	15
2.2 Processing methods	16
2.2.1 Cold Rolling.....	16
2.2.2 Ball milling	17
2.3 Characterization techniques.....	17
2.3.1 Scanning electron microscopy (SEM) and Energy dispersive X-Ray (EDS)	17
2.3.2 Sieverts-type apparatus	19
2.3.3 X-ray diffraction	21

CHAPTER III	
FIRST HYDROGENATION OF MECHANICALLY PROCESSED TIFE-BASED ALLOY SYNTHESIZED BY GAS ATOMIZATION	23
3.1 Authors contributions	23
3.2 Summary of the article	23
3.3 Results and discussion	24
3.3.1 Morphology	24
3.3.2 Chemical analysis	28
3.3.3 First hydrogenation	29
3.3.4 Structural characterization	31
3.3.5 Comparison with other works	34
3.4 Conclusions	35
CHAPTER IV	
HYDROGENATION OF TIXFE₂-X-BASED ALLOYS WITH OVERSTOICHIOMETRIC TI RATIO (X = 1.1, 1.15 AND 1.2)	37
4.1 Authors contributions	37
4.2 Summary of the article	37
4.3 Results and discussion	37
4.3.1 Morphology	38
4.3.2 Chemical analysis	40
4.3.3 Hydrogenation kinetics and PCI	42
4.3.4 Structural characterization	44
4.3.5 Comparison with previous works	49
4.4 Conclusions	51
CHAPTER V	
FIRST HYDROGENATION KINETICS OF INDUCTION MELTED TIFE + 20 WT.% TI (TI_{1.2}FE_{0.85}).....	52
5.1 Contribution des auteurs	52
5.2 Summary of the article	52
5.3 Results and discussion	53
5.3.1 Morphology	53
5.3.2 Chemical analysis	54
5.3.3 Activation kinetics	56

5.3.4	Structural characterization	58
5.3.5	Comparison with previous works	61
5.3.6	Conclusions.....	64
CHAPTER VI		
CONCLUSIONS		65
6.1	Conclusions	65
6.2	Future work.....	65
6.2.1	Study of gas-atomized TiFe based alloys TiFe + 4wt.% Zr + 2 wt.% Mn and Ti _{1.2} Fe	65
6.3	Perspective.....	66
SECTION B		
APPENDICES		
ARTICLES		74

LIST OF TABLES

Table		Page
1	Characteristic of interstitial and non-interstitial hydrides.....	4
2	List the most studied hydride forming compounds	8
3	Chemical composition, in at.%, of the gas atomized EDS analysis (uncertainty is ± 1 for all values).....	28
4	Rietveld refinement of TiFe-phase and amorphous peak for conditions (the uncertainty on the last significant digit is given by the number in parenthesis).....	33
5	Effect of cold rolling on TiFe + 2 wt.% Mn + 4 wt.% Zr alloys	35
6	EDS analysis of overstoichiometric-Ti, Ti_xFe_{2-x} + 4wt.% Zr ($x = 1.1, 1.15$ and 1.2)	42
7	Rietveld refinement of overstoichiometric-Ti, Ti_xFe_{2-x} + 4 wt.% Zr where, $x = 1.1, 1.15$ and 1.2 (the uncertainty on the last significant digit is given by the number in parentheses).....	46
8	Crystal structure parameters of cycled overstoichiometric-Ti, Ti_xFe_{2-x} + 4 wt.% Zr where, $x = 1.1, 1.15$ and 1.2 (the uncertainty on the last significant digit is given by the number in parenthesis).....	49
9	Summary of activation results of previous studies and current work.....	50
10	EDS analysis of induction melted $Ti_{1.2}Fe_{0.8}$ alloy (uncertainty is ± 1 for all values).....	56
11	Rietveld refinement of the as-cast induction melted $Ti_{1.2}Fe_{0.8}$ (the uncertainty on the last significant digit is given by the number in parenthesis).....	59
12	Crystal structure parameters of induction melted $Ti_{1.2}Fe_{0.8}$ cold rolled 5 passes (CR5) and CR5 post-activation (the uncertainty on the last significant digit is given by the number in parenthesis).....	60
13	Summary of activation results and phase fractions of previous studies and current work.....	62

LIST OF FIGURES

Figure		Page
1	Schematic representation of chemisorption in hydride formation.....	3
2	Schematic representation of Pressure-Composition-Isotherm (PCI) curve and the Van't Hoff Plot obtained from the PCI.....	6
3	Interstitial octahedral (O) and tetrahedral (T) sites in face centered cubic (fcc), hexagonal close packed (hcp) and body-centered cubic (BCC) lattices .	7
4	Arc-melting equipment.....	13
5	Diagram of atomization structure and processing basic design.....	14
6	CONSARC furnace	15
7	Schematic representation of cold rolling process	16
8	Schematic representation of cold rolling process	17
9	Schematic representation of scanning electron microscope (SEM)	18
10	Schematic representation of interactions that occur due to the incident electron beam with the surface	19
11	A schematic diagram of volumetric sorption apparatus	21
12	Visualization of the Bragg equation. Maximum scattered intensity is only observed when the phase shifts add to a multiple of the incident wavelength λ [65]	22
13	Backscattered electrons image of an atomized TiFe + 2 wt.% Mn + 4 wt.% Zr particle cross section. a) low - b) high magnification. Backscattered electron image induction melted TiFe + 2 wt.% Mn + 4 wt.% Zr c) low - d) high magnification	26
14	Morphology of atomized powder by processing: a) as atomized, b) cold rolled 1 pass (CR1), c) cold rolled 5 passes (CR5), d) ball milled 5 min, e) ball milled 10 min and f) ball milled 30 min.....	27
15	Backscattered electrons image of atomized particle cross section. Spectrum 1: matrix; spectrum 2: dark grey phase; spectrum 3: bright phase...	28

16	a) Activation under 20 bars of hydrogen pressure and at RT for all samples, b) long-term activation for BM5, BM10 and BM30	30
17	X-ray diffraction patterns of a) As-atomized powder, BM5, BM10, BM30, CR1 and CR5; b) CR5 before and after activation	32
18	Backscattered electron micrograph of overstoichiometric-Ti, $Ti_xFe_{2-x} + 4$ wt.% Zr ($x = 1.1, 1.15$ and 1.2).....	39
19	Secondary electron micrograph of $Ti_{1.1}Fe_{0.9} + 4$ wt.% Zr	40
20	Backscattered electrons image of overstoichiometric-Ti, $Ti_xFe_{2-x} + 4$ wt.% Zr ($x = 1.1, 1.15$ and 1.2). Spectrum 1: matrix; spectrum 2: grey region; spectrum 3: bright region.....	41
21	Activation of overstoichiometric-Ti, $Ti_xFe_{2-x} + 4$ wt.% Zr ($x = 1.1, 1.15$ and 1.2)	43
22	Pressure Composition Isotherm (23 °C) of overstoichiometric-Ti, $Ti_xFe_{2-x} + 4$ wt.% Zr ($x = 1.1, 1.15$ and 1.2).....	44
23	X-ray diffraction patterns of overstoichiometric-Ti, $Ti_xFe_{2-x} + 4$ wt.% Zr for $x = 1.1, 1.15$ and 1.2	45
24	X-ray diffraction patterns of the cycled overstoichiometric-Ti, $Ti_xFe_{2-x} + 4$ wt.% Zr ($x = 1.1, 1.15$ and 1.2).....	47
25	Backscattered electron micrograph of the induction melted $Ti_{1.2}Fe_{0.8}$ alloy	54
26	Backscattered electron micrograph of the induction melted $Ti_{1.2}Fe_{0.8}$ alloy and EDS point spectrums.....	55
27	Activation curve of $Ti_{1.2}Fe_{0.8}$ with and without cold rolling a) 20 hours, b) 3 hours	57
28	X-ray diffraction patterns of the induction melted $Ti_{1.2}Fe_{0.8}$	58
29	X-ray diffraction patterns of the induction melted $Ti_{1.2}Fe_{0.8}$ cold rolled 5 passes (CR5) and CR5 post-activation	60
30	Activation curve of the arc-melted $Ti_{1.2}Fe_{0.8}$	63
31	Backscattered electrons image of induction melted (a) and arc-melted (b) $Ti_{1.2}Fe_{0.8}$	63
32	X-ray diffraction patterns of the induction melted $Ti_{1.2}Fe_{0.8}$	64

SECTION A

CHAPTER I

INTRODUCTION

1.1 Hydrogen storage

The energy sector is now turning to green hydrogen as an alternative form of clean energy. Hydrogen possesses the highest energy density per unit mass in comparison with other fuels. However, its low volumetric density at room temperature and pressure make it difficult to store at high energy density per unit volume [1]. The development of hydrogen storage is a key requirement for the advancement of hydrogen and fuel cell technologies in applications such as stationary power, portable power, and transportation [2, 3]. Hydrogen storage methods can be classified into two categories: physical-based or material-based.

Physical storage is achieved in gas form by the use of high-pressure systems (350 – 700 bar) and/or in liquid form by the use of cryogenic temperatures, below the boiling temperature of hydrogen at atmosphere pressure ($-252.8\text{ }^{\circ}\text{C}$). Tanks storing compressed or liquefied hydrogen have high discharge rates and efficiencies of around 99%, making them appropriate for applications where a local stock of fuel needs to be available upon demand. However, compressed hydrogen (at 700 bar) has only 15% of the energy density of gasoline so storing the equivalent amount of energy at a vehicle refueling station would require nearly seven times the space [4].

Material-based storage or solid-state storage uses different materials to store hydrogen either on the surface of solids (physisorption) or within solids (chemisorption) depending on the nature of the materials. In physisorption, molecular hydrogen (H_2) is adsorbed on the surface by van der Waals interactions. While in chemisorption atomic hydrogen (H) is absorbed to form hydrides [5]. The H_2 reacts with the surface of the solid

and dissociates into hydrogen atoms (Figure 1a). The hydrogen is then absorbed into random locations of the material (Figure 1b). Finally, the hydrogen forms metallic, covalent or ionic bonds with the metal atoms to yield a hydride compound where the hydrogen occupies a specific position in the structure (Figure 1c) [6].

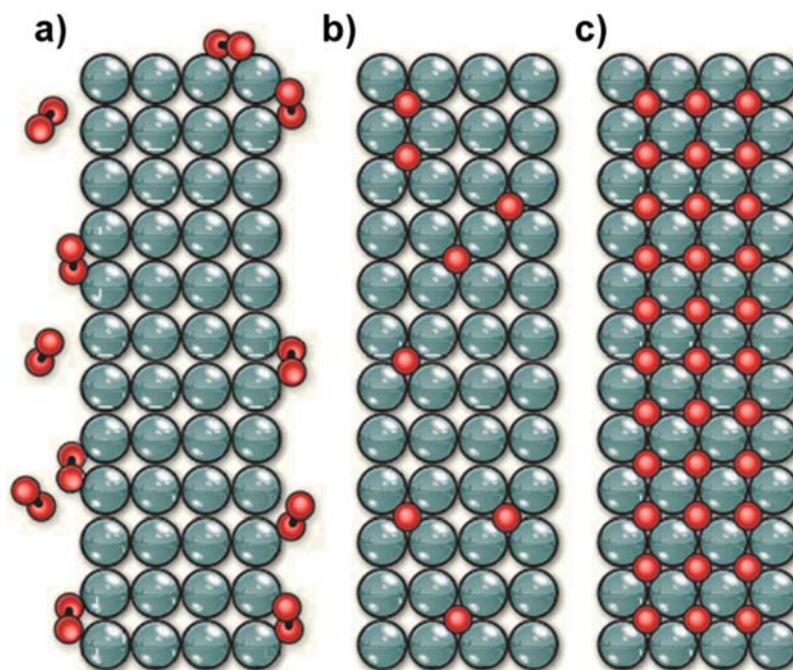


Figure 1. Schematic representation of chemisorption in hydride formation [6].

In this chapter, the focus is set on metal hydrides, their thermodynamics and types. Special emphasis will be set on the hydride forming intermetallic TiFe. The research topic of the thesis is specifically on TiFe-based alloys. Therefore, relevant studies on the subject will be included in order to provide a clear overall idea of the current state of the art on TiFe.

1.2 Metal Hydrides

Metal hydrides are composed of metal atoms that constitute a host lattice and hydrogen atoms [7], where the hydrogen atoms are located within the lattice. The localization of the hydrogen atom allows for two groups of hydrides to be classified,

interstitial and non-interstitial hydrides. Interstitial hydrides form metallic bonds by occupying the interstitial spaces of tetrahedral and/or octahedral sites in the sublattice with hydrogen atoms (LaNi₅H₆, TiCr₂H₄, TiFeH₂, Ti-V-Cr-H₂), non-interstitial hydrides form covalent and/or ionic bonds with neighbor elements (NaAlH₄, Mg(NH₂)₂, LiBH₄, α -MgH₂) [8].

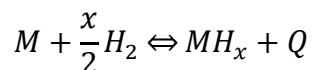
Both non-interstitial (NIH) and interstitial (IH) hydrides have their advantages and disadvantages. For example, NIH possess much higher hydrogen capacity than IH, above 5 wt.% and some reach close to 20 wt.%. However, IH show better reactivity toward hydrogen (lower reaction temperature, faster reaction kinetics and better cycling behavior). Table 1 illustrates the differences between interstitial and non-interstitial hydrides. All the alloys studied in this project are IH. The thermodynamics of IH formation will be described in the following section.

Table 1. Characteristic of interstitial and non-interstitial hydrides.

Type	Metal Elements	Characteristics
Interstitial	Mainly transition metals	→ Weaker bond allowing a lower desorption temperature. → Absorption and desorption depend on dissociation and recombination on the surface and the diffusion in the bulk of hydrogen atoms.
Non-interstitial	Light elements	→ Higher hydrogen capacity per mass. → Desorption depends on the decomposition of the non-interstitial hydrides. → Absorption occurs via recombination of decomposed products, requiring the diffusion of not only hydrogen atoms, but also the other constituent elements.

1.2.1 Thermodynamics

The hydrogenation reaction between the hydride-forming metal (M) and hydrogen is exothermic and can be described by the following reaction, where Q is the heat of reaction.



However, this reaction does not give a lot of insight into the thermodynamic. The thermodynamics of metal hydride formation are best described by the pressure-composition isotherm (PCI) and the resulting Van't Hoff plot. The PCI curve has three regions as seen in Figure 2a. In region I, the concentration of hydrogen, C_H , increases as hydrogen pressure increases up to the plateau pressure. The hydrogen concentration in region I is very small and hydrogen atoms dissolve into sublattice of metal/alloy to form solid solution phase (α -phase). In region II, hydrogen concentration increases at constant pressure (plateau region), where the saturated α -phase converts to β -phase (hydride phase) with the concentration increment. While the two phases coexist, the isotherms show a flat plateau, the length of which determines how much hydrogen can be stored reversibly with small pressure variations [8-10]. At higher hydrogen pressure, further plateaus and further hydride phases may be formed, however in Figure 2a only one plateau is shown.

The plateau behavior is explained by the degree of freedom of the system according to the Gibbs phase rule. The Gibbs phase rule (Equation 1) gives the relationship between the number of phases P and components C in a given alloy under equilibrium conditions at constant pressure, where n is the number of thermodynamic degrees of freedom in the system [11]. The degrees of freedom, designates the number of intensive independent properties that must be specified to fix the state of a system for each phase.

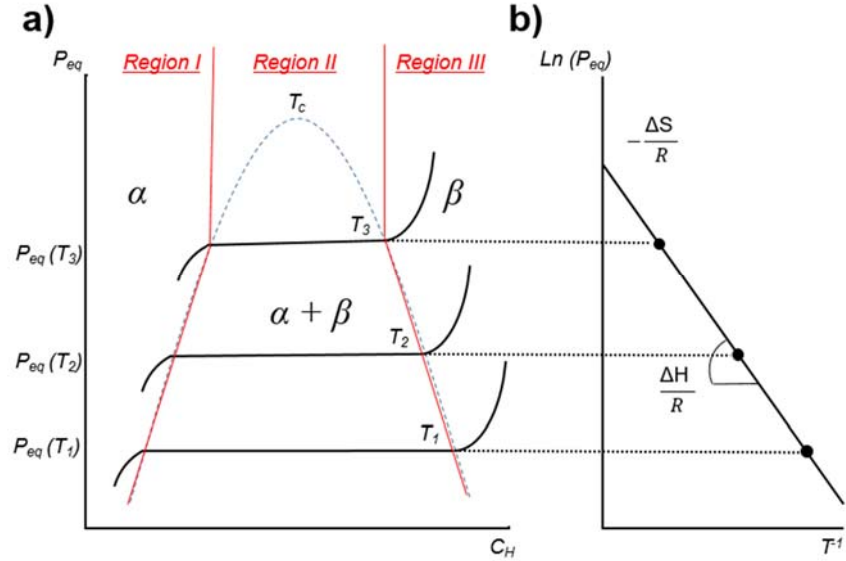


Figure 2. Schematic representation of Pressure-Composition-Isotherm (PCI) curve and the Van't Hoff Plot obtained from the PCI.

$$P + n = C + 2 \quad (1)$$

In region II the system now has three phases (hydrogen gas, α and β) and two components (metal and hydrogen). According to the Gibbs phase rule $n = 1$ which means that only one intensive property must be specified to determine the state of the system in each phase [12]. Therefore, in the two-phase region the concentration increases while the hydrogen pressure is constant. Once the pure β phase is reached (complete disappearance of the α phase) the system has two degrees of freedom. This marks the beginning of region III where hydrogen enters into solid solution in the β phase and the hydrogen pressure again rises with concentration.

The plateau or equilibrium pressure (P_{eq}) depends strongly on temperature (T) and is related to the changes of enthalpy (ΔH) and entropy (ΔS). Since the entropy change corresponds mostly to the change from molecular hydrogen gas to dissolved hydrogen, it can be considered a constant. The Gibbs free energy (ΔG) in the plateau region is a function of temperature, as P_{eq} depends on T [8], see Equation 2 and Figure 2.

$$\Delta G = RT \ln(P_{eq}) \quad (2)$$

From Equation 2, the Van't Hoff equation can be obtained (see Equation 3). The equilibrium pressure at $\alpha \rightarrow \beta$ phase transformation is given by the Van't Hoff law and is seen plotted in the graph in Figure 2b. In the graph, the ΔH and ΔS are the slope and intercept of the straight-line plotting $\ln(P_{eq})$ versus T^{-1} . The temperature dependent plateau pressure is the equilibrium dissociation pressure of the hydride (β -phase), thus being a measure of the stability of the hydride. In other words, thermodynamic stability of the hydride can be reduced by increasing the plateau pressure at a given temperature. Moreover, the width of the plateau region determines the maximum amount of reversibly absorbed and desorbed hydrogen.

$$\ln(P_{eq}) = \frac{\Delta H}{RT} - \frac{\Delta S}{R} \quad (3)$$

1.2.2 Types of interstitial hydrides

Intermetallic hydrides represent the hydrides of alloys composed of transition metals. Hydrogen occupies the tetrahedral and/or the octahedral sites of intermetallic hydrides. Figure 3 shows a schematic representation for the fcc, hcp and bcc structures.

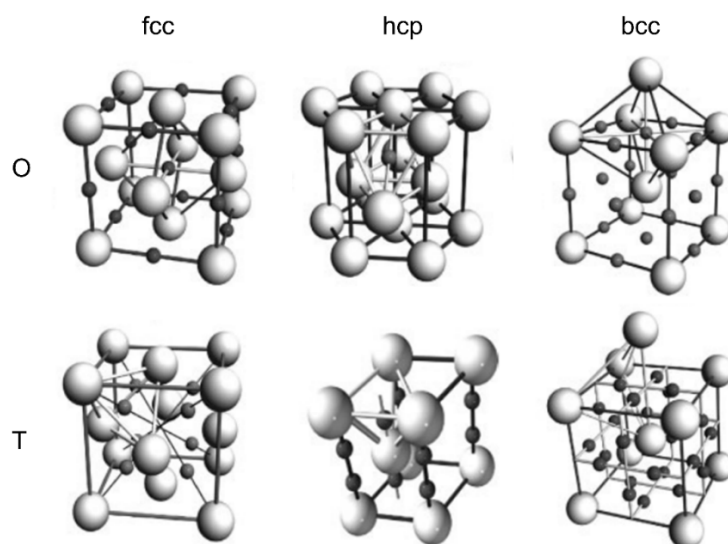


Figure 3. Interstitial octahedral (O) and tetrahedral (T) sites in face centered cubic (fcc), hexagonal close packed (hcp) and body-centered cubic (BCC) lattices [10].

In most cases, intermetallic compounds (A_xB_y) consist of a metal that easily forms stable hydrides (A) and another element which does not form stable hydrides (B). The intermetallics thus formed could then be grouped according to their stoichiometry such as: AB_5 ($LaNi_5$, $CaNi_5$), AB_2 ($ZrMn_2$, ZrV_2), AB ($TiFe$) and A_2B (Mg_2Ni). Table 2 shows the most studied hydride forming compounds and classifies the type each one belongs to, as well as the wt%, vol% and entropy.

Table 2. List the most studied hydride forming compounds.

Type	Hydride	$C_m/wt.\%$	$C_v/kg\cdot m^{-3}$	$\Delta H/kJ\cdot mol^{-1}$	Ref.
AB_5	$LaNi_5H_6$	1.4	92	-31.2	[13]
AB_2	$TiCr_2H_4$	2.57	108	-23	[14]
	$TiMn_{1.5}H_{2.5}$	1.86	119	-28.5	
BCC	$V_{22}Ti_{35}Cr_{43}$	2.5	156	-39	[15]
AB	$TiFeH_2$	1.89	96	-28.1	[16]

1.3 TiFe

The alloy TiFe is a well-known metal hydride that has a hydrogen absorption capacity of 1.86 wt.% at low pressure at room temperature [17],[18]. First hydrogenation or so-called “activation” is usually slow at room temperature. The activation mechanisms have been shown to be dependent on the surface condition [19, 20]. TiFe is highly sensitive to air and forms a passivation layer that inhibits the activation. Generally, some form of heat treatment is needed to speed up the activation kinetics of pure TiFe. This activation heat treatment requires cycling between high temperature and room temperature under high hydrogen pressure, a process that is time consuming and would ultimately increase the hydride’s cost and the cost of any tank that would hold the hydride.

The activation of TiFe has been improved by different approaches. For example the use of mechanical processing techniques such as ball milling, cold rolling, high-pressure torsion [2, 21-24] and/or the addition of transition metals [25-30] have both shown to improve the kinetics.

Previous studies have shown how the addition of Zr greatly improves the TiFe activation kinetics by forming secondary phases [31-35]. The addition of 4 wt.% represents the minimum threshold in order to achieve activation without any pretreatment [31]. Further increase of Zr wt.% enhances the abundance of the secondary phases which improves the kinetics but decreases the reversible capacity [36]. Extensive work has been done on the phase equilibria diagram of the Ti-Fe-Zr system [37-42]. Zeng et al. experimentally investigated the phase relations of isothermal sections of the Ti-Fe-Zr ternary system at 875 and 1173 K. Four stable ternary phases were identified as τ_1 , τ_2 , τ_3 , τ_4 and eight three-phase equilibria regions were detected. The τ_1 and τ_3 phases presented a C14 structure and the τ_2 , τ_4 phase presented a Fd3-m cubic structure [38]. The ternary phases are of interest for metal hydride research since they are likely to be formed as secondary phases.

Faisal et al. investigated first cycle hydrogenation properties of Ti-Fe-Zr ternary alloys but their compositions were highly Ti-understoichiometric (25 at.% Ti, 50 at.% Fe, 25 at.% Zr) and (38.1 at.% Ti, 33.3 at.% Fe, 28.6 at.% Zr) [37]. It is therefore difficult to compare their finding with the present Ti- overstoichiometric system. Nevertheless, their XPS studies indicates the presence of an Fe⁰ metallic state directly below the alloy surface, which may catalyze hydrogen dissociation at room temperature.

TiFe alloy with overstoichiometric-Ti has been previously studied with the goal of obtaining the metastable phase Ti₂Fe [17, 43]. Reilly et al. were the first to try to obtain Ti₂Fe to study the hydrogenation properties. However after synthesizing and annealing at 1000K the stoichiometry Ti₂Fe (63% Ti – 37% Fe) the attempt was unsuccessful and the phases formed were TiFe and Ti [17]. Park et al. synthesized and annealed at 1470 K the composition Ti_{1.2}Fe (60% Ti – 40% Fe). They obtained three phases TiFe (92%), Ti₂Fe

(3%) and $\text{Ti}_4\text{Fe}_{(\text{BCC})}$ (5%). The $\text{Ti}_{1.2}\text{Fe}$ alloy could be activated at low pressure and room temperature reaching 2.1wt.% H in 6 hours. The composition of each phase was measured to study the surface of each phase by XPS. However only the TiFe and $\text{Ti}_4\text{Fe}_{(\text{BCC})}$ alloys were synthesized as the Ti_2Fe composition was not possible to synthesize as a single-phase alloy. From this work it was concluded that the improvement of the kinetics is due to the formation of the Ti_2Fe and $\text{Ti}_4\text{Fe}_{(\text{BCC})}$ phases, or the formation of a Ti-rich oxide layer measured on the $\text{Ti}_4\text{Fe}_{(\text{BCC})}$ alloy [44]. The possibility of using Ti itself as the alloying element instead of other more expensive transition metals [25, 31] or rare earth elements to improve the activation kinetics of TiFe is of great interest because this would decrease the cost of the alloy and simplify production.

Besides activation, the production cost of metal hydride forming alloys in an industrial scale is also of importance for commercialization. The typical process to obtain metal hydride alloys is by fusion (arc-melting, induction melting, electron beam). Other methods such as electrochemical reduction, mechanical alloying, combustion synthesis, etc. are also used [18, 45]. The development of a one-step synthesis process that results in an alloy with an ideal microstructure is a task that has not been achieved. Most of the prior mentioned synthesis techniques require processing or heat treatment to achieve good hydrogenation properties. Gas atomization is a synthesis process that can directly produce metallic powders at an industrial scale. This is one of the reasons why it would be beneficial to study the effect of this synthesis method on the hydrogen storage of TiFe-based alloys to determine if it is a viable option. The second reason concerns the fine microstructure that this synthesis method produce. The microstructure of an alloy will greatly affect its hydrogenation properties. Patel et al. studied the effect of the cooling rate on the microstructure of $\text{TiFe} + 4\text{wt}\% \text{Zr}$ by casting in a step mold with different thicknesses. Higher cooling rates resulted in finer distribution of the secondary phase that proved to be beneficial to the activation kinetics [46].

There have been no previous investigations on the hydrogenation behaviour of atomized TiFe-based alloys. There is some work done on metal hydride powders produced by gas atomization for hydrogen storage and for nickel-metal hydride batteries.

Some focus on electrochemical cycling and the discharge capacity: AB₅-type alloys (LaNi_{4.75}Sn_{0.25}, MmNi_{3.6}Co_{0.56}Mn_{0.56}Al_{0.28}, Zr-based) [47-50], while others did report the gas-phase hydrogenation (MmNi_{3.6}Co_{0.56}Mn_{0.56}Al_{0.28} and Zr-based AB₂) [48, 51]. Kim et al. [51], showed that, for the AB₂ alloy Zr_{0.55}Ti_{0.45}V_{0.54}Mn_{0.24}Ni_{0.88}Co_{0.16}Cr_{0.16} produced by gas atomization, the particles smaller than 50 μm present a highly sloped plateau and a larger hysteresis loop than particles larger than 50 μm as well as a decrease of the storage capacity. This was explained by a partially amorphous phase which inhibited the hydride–dehydride reaction between the gas–solid. Chung et al. [48] found that, particles smaller than 10 μm showed slower kinetics and lower capacity than larger particles of AB₅ type alloy. However, no amorphous phase was found.

1.4 Research goals

The goal of the PhD project was to investigate the activation kinetics of TiFe-based alloys for hydrogen. The objectives can be divided as follows:

- Compare different synthesis and processing techniques to obtain TiFe-based alloys for hydrogen storage.
- Examine the effect of new alloying compositions of TiFe-based alloy for hydrogen storage. (Overstoichiometric Ti: Ti_xFe_{2-x} + 4 wt% Zr (x = 1.1, 1.15 and 1.2) and Ti_{1.2}Fe_{0.8}).
- Investigate the effect air-exposed on activation kinetics.

1.5 Thesis structure

The thesis has been divided into six chapters. Chapter I is the introduction to hydrogen storage in metal hydrides, focusing on the intermetallic TiFe. Chapter II presents the description of the experimental details and a brief description of the theory behind each technique. Chapter III covers the study of the first hydrogenation of mechanically processed alloy (TiFe+ 2 wt.% Mn + 4 wt.% Zr) synthesized by gas atomization.

Chapter IV shows the results of the addition of overstoichiometric-Ti to the alloy $\text{Ti}_x\text{Fe}_{2-x} + 4 \text{ wt.}\% \text{ Zr}$ ($x = 1.1, 1.15$ and 1.2). Chapter V shows investigation of the activation kinetics and regeneration ability of TiFe doped with Ti. The results corroborate how Ti used as a doping element can be as effective as adding other more expensive transition metals. Finally, in Chapter VI the conclusion and future work are presented.

CHAPTER II

EXPERIMENTAL DETAILS

2.1 Synthesis methods

2.1.1 Arc-melting

The arc-melting equipment used was a lab scale synthesis method available at the Hydrogen Research Institute. Before scaling up any composition it is of great importance to run initial hydrogenation trials on smaller sample sizes before investing into costly production techniques as gas-atomization or induction melting. For arc melting, the composition is calculated and weight to a 3 grams sample size. A standard Tungsten Inert Gas (TIG) welding unit is used as a power source. Heating is done via an electric arc between the tungsten electrode and the metals placed in the copper crucible. Figure 4 shows the arc-melting set up. To avoid oxidation, the chamber is evacuated and then filled back with argon gas. To ensure the homogeneity of the sample, the pellets are turned over and remelted three times.



Figure 4. Arc-melting equipment.

2.1.2 Gas-atomization

Gas atomization is a synthesis technique that is used in the powder metallurgy field.

It is also known as two phase or two fluid atomization [52, 53]. Figure 5 shows a schematic representation of gas atomization processing. The first phase will always refer to the molten metal while the second phase in this case will be a gas, such as, air, an oxygen mixture, nitrogen, argon, or helium [53-55]. Inert gas is generally used. This is usually desired because reactions between the phases are avoided. As seen in Figure 5, the molten metal is forced through an orifice at moderate pressure and is disintegrated into small droplets or splats when the metal stream is impacted by high energy jets of a particular fluid medium. The high solidification rates ($\sim 10^5$ K/s) classify the technique as a rapid solidification technique.

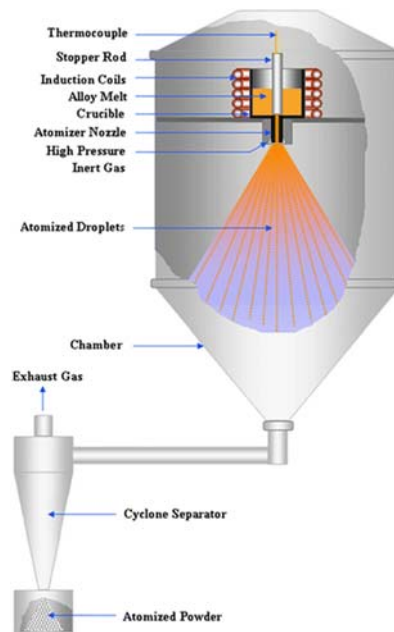


Figure 5. Diagram of atomization structure and processing basic design [56].

The gas atomization synthesis performed for the project was of composition TiFe + 2 wt.% Mn + 4 wt.% Zr. It was carried out by the industrial collaborator GKN Hoeganaes Innovation Center & Advanced Materials, using industrial grade Fe (ASTM 1005), Ti (ASTM B265 grade 1), Zr 702 (99.2%) and electrolytic manganese Mn (99.7%).

The atomization was done under pure argon with a VIGA-type furnace with a free fall atomization ring configuration. The resulting powder alloy was packed in air and shipped.

2.1.3 Induction melting

Induction melting is done in an electrical furnace; the operation is based on heating through electromagnetic induction. This technology mainly consists of an inductor and a crucible. The crucible is surrounded by a copper tube that forms a coil. An alternative current passes through the primary inductive circuit (coil), leading to the generation of an alternating magnetic field. Under the influence of a magnetic field in a body placed inside the inductor, an electric field appears which induces eddy currents (also called Foucault current). These eddy currents will generate heat by Joule effect. This will ultimately melt the material inside the crucible. The induction melting furnace model was a CONSARC furnace (see Figure 6), this model operates between 0.06 - 0.1 Torr with a water-cooled copper crucible. During the heating process, the material in contact with the crucible might not melt or will re-solidify after some time. The sample was melted under vacuum and left to solidify inside the crucible. The sample did not present a slag layer and only a thin oxidized superficial layer which was later removed by sandblasting.



Figure 6. CONSARC furnace.

2.2 Processing methods

2.2.1 Cold Rolling

Cold rolling (CR) is commonly used in industrial applications as a precision forming technique that applies the principle of plastic forming to obtain different shaft parts. Currently cold rolling has also been reported to greatly improve the hydrogenation kinetics of hydride forming alloys (HFA) [2, 21, 35, 57]. The cold rolling of HFA is performed on a previously crushed sample that is placed between two stainless steel plates in order to better constrict the sample. The plates are set between two rollers as shown in Figure 7. The rollers generate mechanical stress by applying a reduction to the powder and plates inducing deformation on the powder. The main different with cold rolling on HFA and the typical industrial use of the technique is the nature of the HFA samples which are typically brittle, and although plastic deformation may be occurring the most notable effect is the fissuring of particles which exposes fresh surface area.

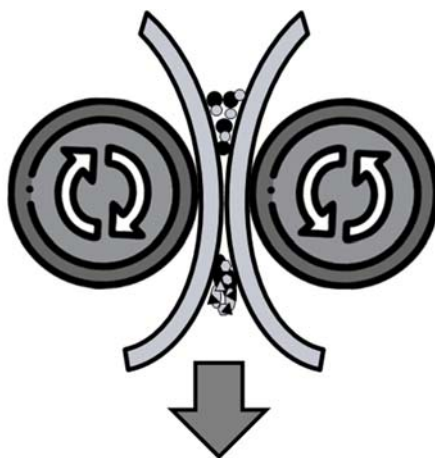


Figure 7. Schematic representation of cold rolling process.

The cold Rolling was performed under air using a modified version of Durston DRM 130 model where the powder samples could be cold rolled vertically. Samples were cold rolled for 1 or 5 passes (CR1, CR5).

2.2.2 Ball milling

Ball milling is a powder processing technique, where powder is introduced into a crucible that contains balls or cylinders that will generate collisions with the powder. The crucible rotates in one or more axis and can do so at different speeds. The design of the ball mill determines the classification of the equipment. Ball mills are classified as planetary, tumbler, attrition, vibration, and high energy ball milling [22, 24, 58, 59]. For this project a high energy milling machine SPEX 8000M (1725 RPM) apparatus was used. Figure 8 shows a schematic representation of the SPEX mixing dynamics. The ball to sample mass ratio was 10:1. The powder was prepared, processed, and handled under argon.

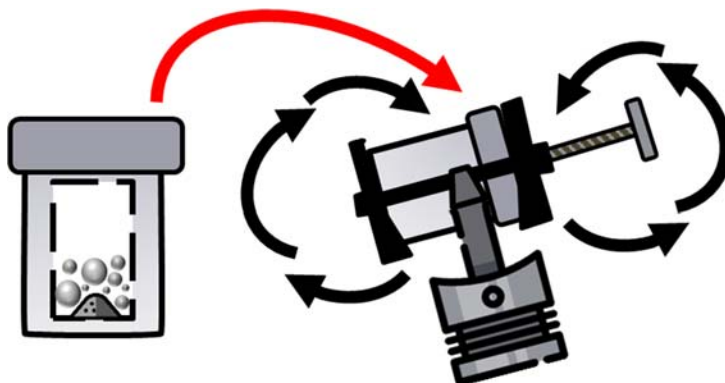


Figure 8. Schematic representation of cold rolling process.

2.3 Characterization techniques

2.3.1 Scanning electron microscopy (SEM) and Energy dispersive X-Ray (EDS)

The elements of a scanning electron microscope are detailed in Figure 9. The electron gun produces a beam of electrons that is attracted through the anode and condensed by the condenser lens and then focused as a very fine point on the specimen by the objective lens. A set of small coils of wire, called the scan coils, are located within the objective lens. The coils are energized by a varying voltage produced by the scan generator and create a magnetic field that deflects the beam of electrons back and forth in a

controlled pattern called a raster. The raster is very similar to a raster used in a television receiver.

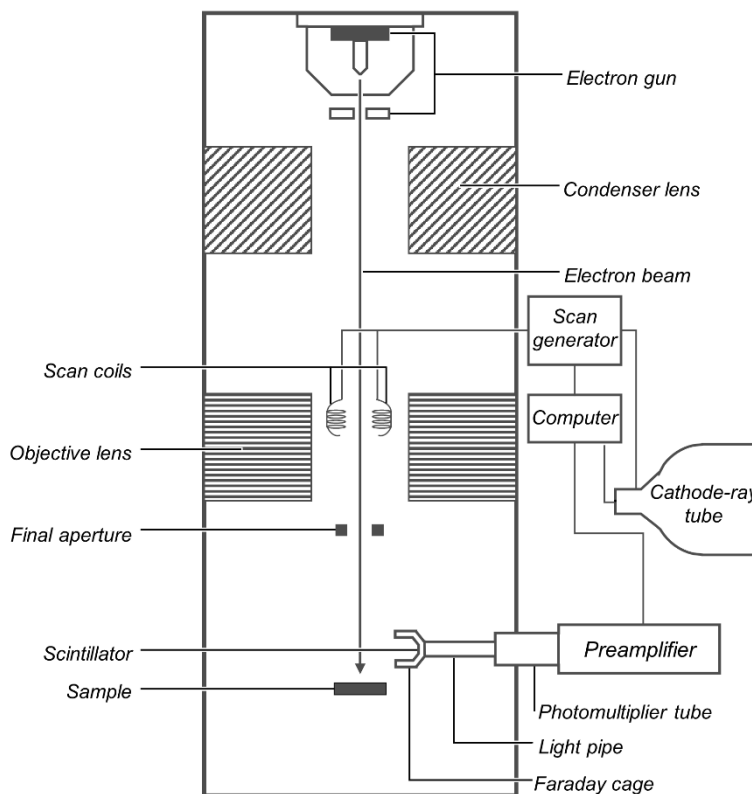


Figure 9. Schematic representation of scanning electron microscope (SEM).

The varying voltage from the scan generator is also applied to a set of deflection coils around the neck of a cathode-ray tube (CRT). The magnetic field from this coil causes the deflection of a spot of light back and forth on the surface of the CRT. The pattern of deflection of the beam of electrons on the sample is exactly the same as the pattern of deflection of the spot of light on the CRT. When the incident beam electron strikes the surface of a sample, it undergoes a series of complex interactions with the electrons of the atoms of the sample. The interaction produces a variety of secondary products, such as electron of different energy, X-rays, heat, and light. Many of these secondary products are used to produce the images of the sample and to collect additional data from the sample [60, 61]. Figure 10 illustrates some of the interactions that occur due to the incident electron interaction with the surface. The analysis performed in the project

are: Secondary electrons (SE), backscattered electrons (BSE) and characteristic X-ray (EDS).

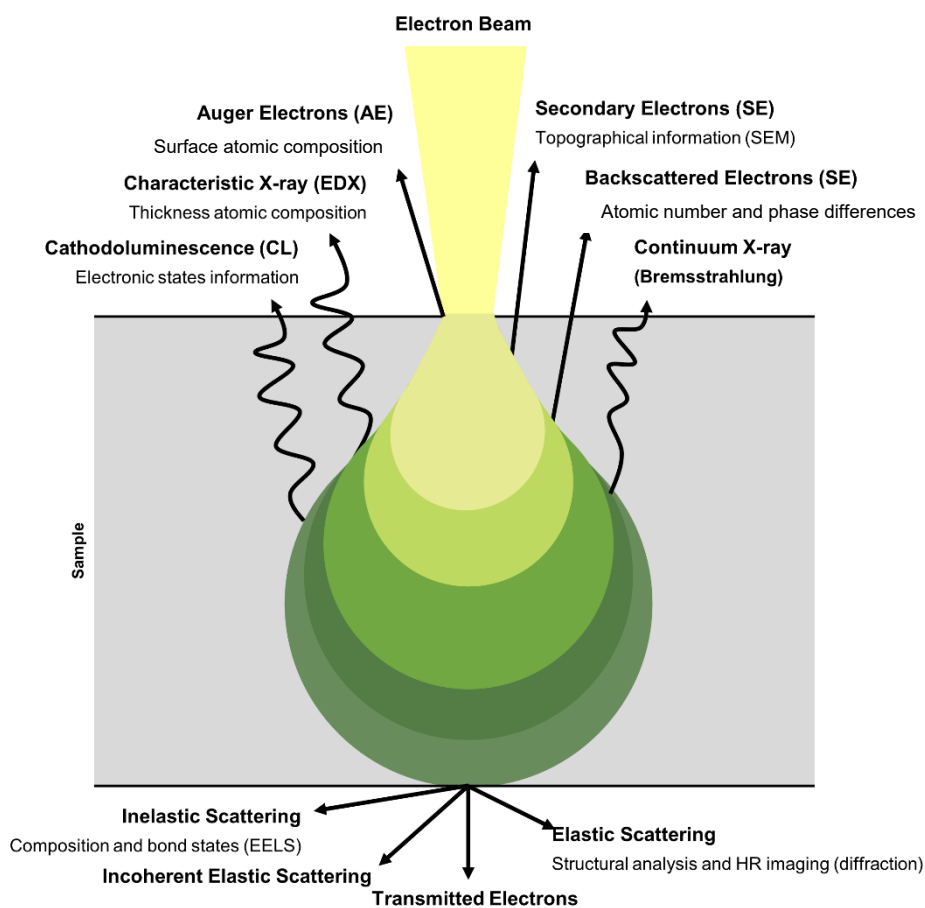


Figure 10. Schematic representation of interactions that occur due to the incident electron beam with the surface.

2.3.2 Sieverts-type apparatus

Although testing a material in a prototype storage unit is probably the most effective method for determining how well it performs as a hydrogen store, this is not practical when developing, or searching for, new materials. The Sieverts-type apparatus is a gas sorption measurement device. Gas sorption measurements can be broadly separated into categories: gravimetric and volumetric. The Sieverts-type apparatus is a type of volumetric techniques where the amount of hydrogen absorbed or desorbed by the sample is determined by measuring the change in pressure in a fixed, known volume: absorption

or adsorption results in a decrease in the observed pressure, whereas desorption results in an increase [62]. The number of moles sorbed is given by Equation 3. Where $Z_{i,T}$ and $Z_{f,T}$ are the compressibility coefficients under P_i (initial pressure) and T and P_f (final pressure) and T . P is the pressure of the gas, V the volume of the gas, n is the amount of substance of gas (moles) absorbed, R is the gas constant and T the absolute temperature of the gas. The diagram in Figure 11 further describes Equation 3.

$$\Delta n = \frac{P_i V_1}{Z_{i,T} R T} - \frac{P_f (V_1 + V_2)}{Z_{f,T} R T} \quad (3)$$

A schematic diagram of a basic manometric system is shown in Figure 11 [63]. The valves B and C are first opened to evacuate V_1 and V_2 . After sufficient time, valves B and C are then closed. Valve A is opened, allowing V_1 to fill with hydrogen to an initial pressure P_i . Valve C is then opened thus filling V_2 . Any drop in pressure beyond that which is expected from the volume difference between V_1 and $(V_1 + V_2)$ is then assumed to have resulted from the absorption of hydrogen.

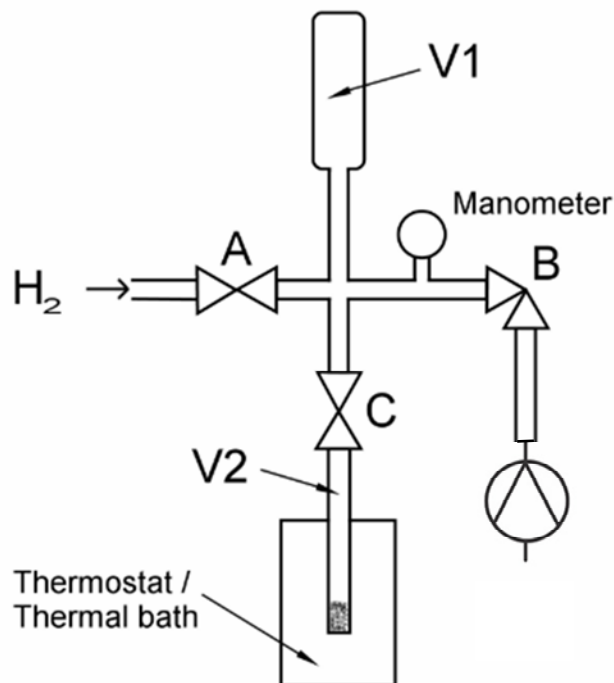


Figure 11. A schematic diagram of volumetric sorption apparatus [63].

To extend this measurement to a full isotherm, the subsequent step would then use the values of Δn and P_f as a starting point. The repetition of the above procedure will result in the measurement of a complete absorption isotherm [63].

2.3.3 X-ray diffraction

X-ray diffraction is based on the constructive interference of monochromatic X-rays and a crystalline sample. These X-rays are generated by a copper target, filtered to produce monochromatic radiation, collimated, and directed toward the sample. The interaction of the incident rays with the sample produces constructive interference (and a diffracted ray) when conditions satisfy Bragg's Law (see Equation 4) [64].

$$n\lambda = 2d \sin \theta \quad (4)$$

This law relates the wavelength (λ) of electromagnetic radiation to the diffraction angle (θ) and the lattice spacing (d) in a crystalline sample. Figure 12 shows a schematic

representation of the X-ray interaction with the atoms. These diffracted X-rays are then detected, processed and counted. By scanning the sample through a range of 2θ angles, all possible diffraction directions of the lattice should be obtained due to the random orientation of the powdered material [64, 65]. Conversion of the diffraction peaks to d-spacings allows identification of the alloy because each phase has a set of unique d-spacings. Typically, this is achieved by comparison of d-spacings with standard reference patterns.

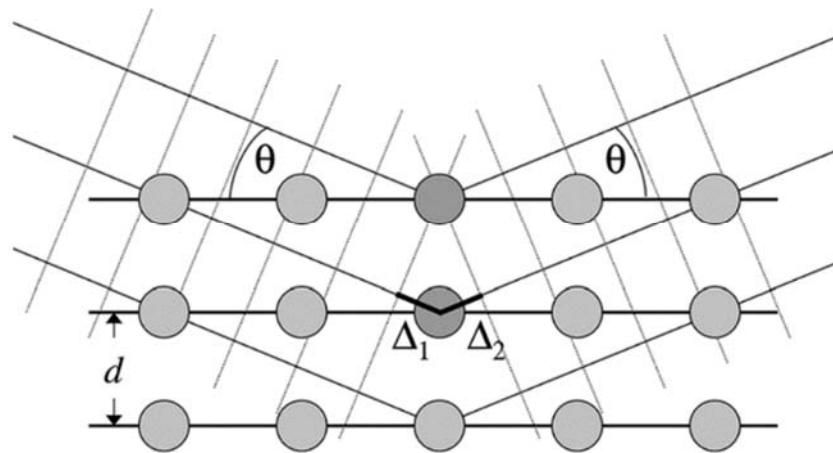


Figure 12. Visualization of the Bragg equation. Maximum scattered intensity is only observed when the phase shifts add to a multiple of the incident wavelength λ [65].

CHAPTER III

FIRST HYDROGENATION OF MECHANICALLY PROCESSED TIFE-BASED ALLOY SYNTHESIZED BY GAS ATOMIZATION

The content of Chapter III has been published in the *International Journal of Hydrogen Energy*. Volume 46, Issue 10, 8 February 2021, Pages 7381-7389. The article can be found in the following link: <https://doi.org/10.1016/j.ijhydene.2020.11.237>

3.1 Authors contributions

The authors of the article are Ms. Elena Ulate-Kolitsky, Doctor Bernard Tougas, Mme Bettina Neumann, Dr. Chris Schade and Doctor Jacques Huot.

Ms. Ulate-Kolitsky was responsible for the entirety of the experimental work presented in the article. The analysis of the results was done by Ms. Ulate-Kolitsky who was also responsible for the initial manuscript and finalizing any changes after discussion with the other authors. Dr. Tougas (Co-advisor) and Dr. Huot (Advisor) assisted with insightful discussion, comments, and suggestions on the article. Several versions of the manuscript were written until everyone was satisfied with the article. Dr. Huot played an important role finalizing the Rietveld refinement. Mme. Neumann and Mr. Schade both work for the industrial partner GKN. They were both involved in the synthesis of the alloy that was studied as well as the final revision and approval of the article.

3.2 Summary of the article

The overall project focuses on TiFe-based alloys and different approaches to improve its first-hydrogenation kinetics. Therefore, a look into an alternative synthesis method was possible thanks to the help of the industrial partner GKN. The alloy TiFe +

2 wt.% Mn + 4 wt.% Zr synthesized by induction melting has been previously studied and shown to possess good first hydrogenation (activation) kinetics without the need for an activation heat treatment [66]. This article focuses on the effect of gas-atomization on TiFe + 2 wt.% Mn + 4 wt.% Zr microstructure and its activation kinetics. The microstructure obtained by gas-atomization is different than those obtained by "standard" commercial methods. Atomization does not yield an ingot but directly produces alloyed-powder. The powder was stored in air after synthesis.

The as-received powder did not activate under the experimental conditions (20 bar, room temperature) after a period of 24 hours. Mechanical processing was performed in order to achieve activation, cold rolling (1 and 5 passes) and Ball milling (5, 10 and 30 minutes). It is thought that being exposed to air for over 2 months generates a passivation layer which was broken up during the mechanical processing. In the case of the cold rolled 5 passes samples the exposure of fresh surface area resulted in fast activation kinetics that reached saturation in about 2 hours.

To see the actual effect of the gas-atomized microstructure the results were compared to the work reported by Manna et al. who studied the effect of air exposed TiFe + 2 wt.% Mn + 4 wt.% Zr synthesized by induction melting. After air exposure their samples required cold rolling (5 passes) to achieve activation. Based on the results from the comparison with previous work it was concluded that gas-atomization is a good candidate to produce TiFe-based alloys that present good kinetics and capacity after air exposure.

3.3 Results and discussion

3.3.1 Morphology

Figure 13a and 13b show the microstructure of the as-atomized TiFe + 2 wt.% Mn + 4 wt.% Zr alloy. The powder presents a dendritic structure where the microstructure consists of a matrix (grey phase), a darker grey secondary phase and a bright phase.

The phase fractions were calculated by image processing, the matrix accounts for 76% of the alloy, with the secondary and bright phases are respectively 20% and 4% of the total surface. Figure 13c and 13d show the microstructure of the TiFe + 2 wt.% Mn + 4 wt.% Zr alloy synthesized by induction melting previously reported by Patel et al. Their work serves as a comparison with the atomized powder. A clear difference is notable, the atomized powder's microstructure is much finer. The induction melted alloy presents a eutectic microstructure within the interphase region. The eutectic reaction is between the matrix (TiFe) and the bright phase (Zr-rich 20 at.%). The explanation for the different microstructure is the nature of the synthesis process and the solidification rate of each technique. The alloy that was gas-atomized undergoes rapid solidification, meaning that the melt becomes solid at an extremely high cooling rate between $\sim 10^5$ K/s. Therefore, the eutectic reaction does not have time to occur. On the other hand, the cooling rate for the cast obtained by induction melting would have presented a standard cooling rate.

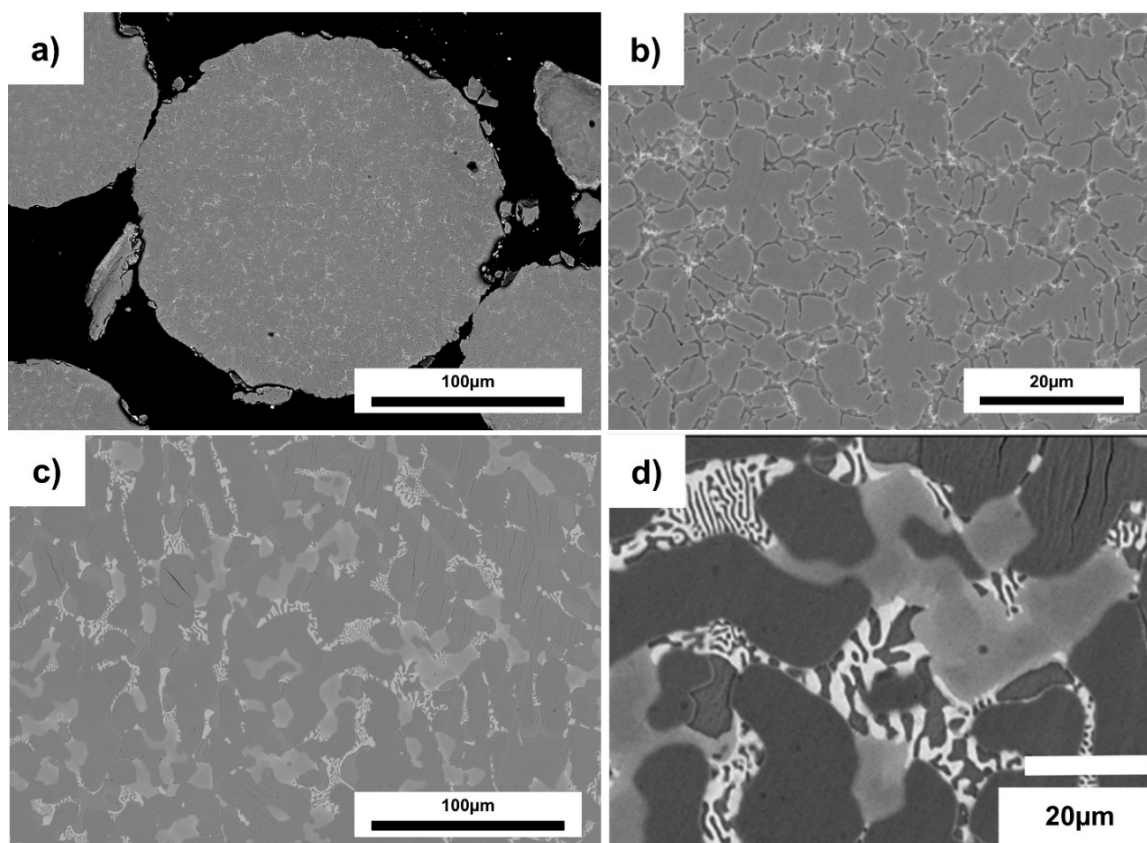


Figure 13. Backscattered electrons image of an atomized TiFe + 2 wt.% Mn + 4 wt.% Zr particle cross section. a) low - b) high magnification. Backscattered electron image induction melted TiFe + 2 wt.% Mn + 4 wt.% Zr c) low - d) high magnification.

Figure 14a shows the as-received atomized powder. The particles are mainly spherical, some present small satellites, where two spheres are joined. The particle size distribution, D_{50} , was determined to be 105 μm . The as-atomized powder was subjected to 20 bars of hydrogen at room temperature for a period of at least 24 hours. No hydrogen uptake was registered.

The application of mechanical processing techniques was done to improve the activation kinetics of the atomized (as-received) powder. The following techniques were studied: cold rolling (1 and 5 passes) in air and ball milling (5, 10 and 30 minutes) under argon. The conditions studied for cold rolling and ball milling are designated, CR1, CR5, BM5, BM10 and BM30. The micrographs of the processed powder can be seen in Figure 14b, 14c, 14d, 14e and 14f respectively. The CR1 image shows that most of the big spheres were cracked while there is some consolidation of the smaller particles

forming a porous plate sample. For CR5 the cracking of the big sphere is less apparent, and most particles are compressed together in the same way to CR1 formed a porous plate structure. The ball milled samples were broken up into fine irregular powder particles. As the time of BM increases a decrease of particle size is noted as well as the formation of larger agglomerations of these small particles.

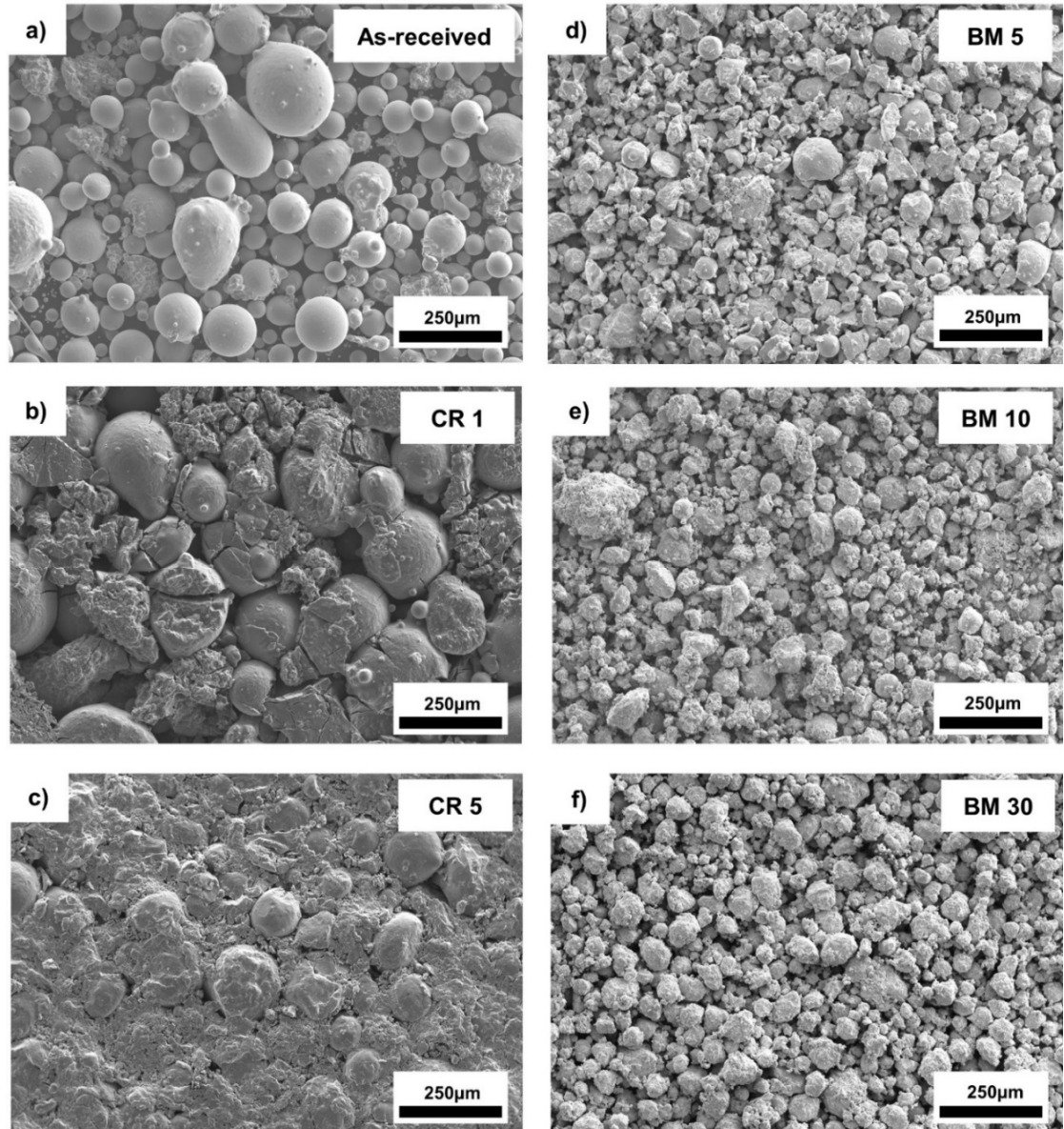


Figure 14. Morphology of atomized powder by processing: a) as atomized, b) cold rolled 1 pass (CR1), c) cold rolled 5 passes (CR5), d) ball milled 5 min, e) ball milled 10 min and f) ball milled 30 min.

3.3.2 Chemical analysis

Figure 15 shows the regions where EDS point analysis was performed. The chemical composition of the bulk and each specific region was measured by EDS, and the results are shown in Table 3.

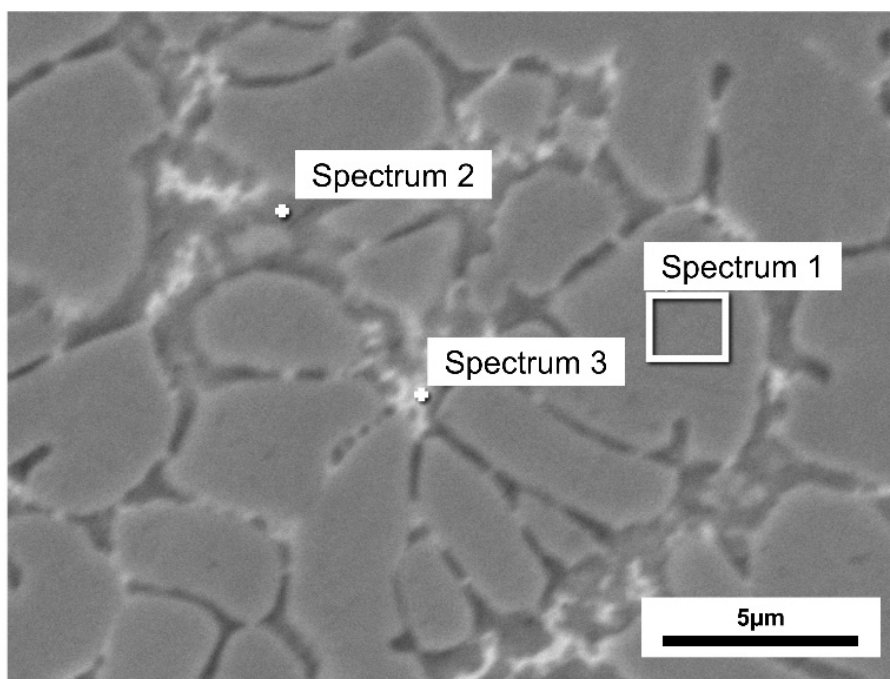


Figure 15. Backscattered electrons image of atomized particle cross section. Spectrum 1: matrix; spectrum 2: dark grey phase; spectrum 3: bright phase.

Table 3. Chemical composition, in at.%, of the gas atomized EDS analysis (uncertainty is ± 1 for all values).

	Nominal composition	Bulk composition	Spectrum 1	Spectrum 2	Spectrum 3
Ti	47.9	55.6	51.0	71.2	58.4
Fe	47.9	39.8	46.9	21.5	23.2
Mn	1.9	2.2	1.7	2.2	2.4
Zr	2.3	2.4	0.4	5.1	16.0

The bulk measurement shows that the alloy is titanium-rich, and the composition could be written as $\text{Ti}_{1.11}\text{Fe}_{0.80}\text{Mn}_{0.04}\text{Zr}_{0.05}$. This is different from the nominal composition ($\text{Ti}_{0.96}\text{Fe}_{0.96}\text{Mn}_{0.04}\text{Zr}_{0.05}$) however, the Mn and Zr abundances do match the nominal composition. The bulk composition is close to the composition reported in the work reported by Patel et al. on $\text{TiFe} + 2 \text{ wt.}\% \text{ Mn} + 4 \text{ wt.}\%$ that has been used as comparison.

The matrix (Spectrum 1) is essentially TiFe alloy with a slight amount of Mn and very small proportion of Zr. The secondary phase (Spectrum 2) is Ti-rich and has higher content of Mn and Zr than the matrix. In fact, assuming that Mn and Zr are on the same site as Fe, this phase has a stoichiometry close to $\text{Ti}_2(\text{Fe},\text{Mn},\text{Zr})$. The bright regions (Spectrum 3) are Zr rich.

3.3.3 First hydrogenation

Figure 16a shows the activation curves of all the conditions. The as-received sample did not activate even after more than 24 hours. The fastest activation and highest capacity were achieved by the CR5 sample. Both the CR 1 and CR5 present high kinetics, reaching saturation in 3 and 2 hours respectively and no loss of capacity. All ball milled samples presented very slow kinetics. BM5 and BM10 reached a capacity of $\sim 1.8 \text{ wt.}\%$ but were still slowly absorbing when the experiment was stopped after 60 hours (see Figure 16b). BM30 suffered a severe decrease of kinetics reaching only $\sim 0.85 \text{ wt.}\%$ after 60 hours of hydrogen exposure. Ball milling's highly energetic character has been shown to become detrimental after a certain time reducing the amount of hydrogen being able to be absorbed. Although grain boundaries have been shown to enhance hydrogenation kinetics [24], when the surface area of the grain boundaries exceeds that of the grains capacity can be affected as seen in the BM30 sample.

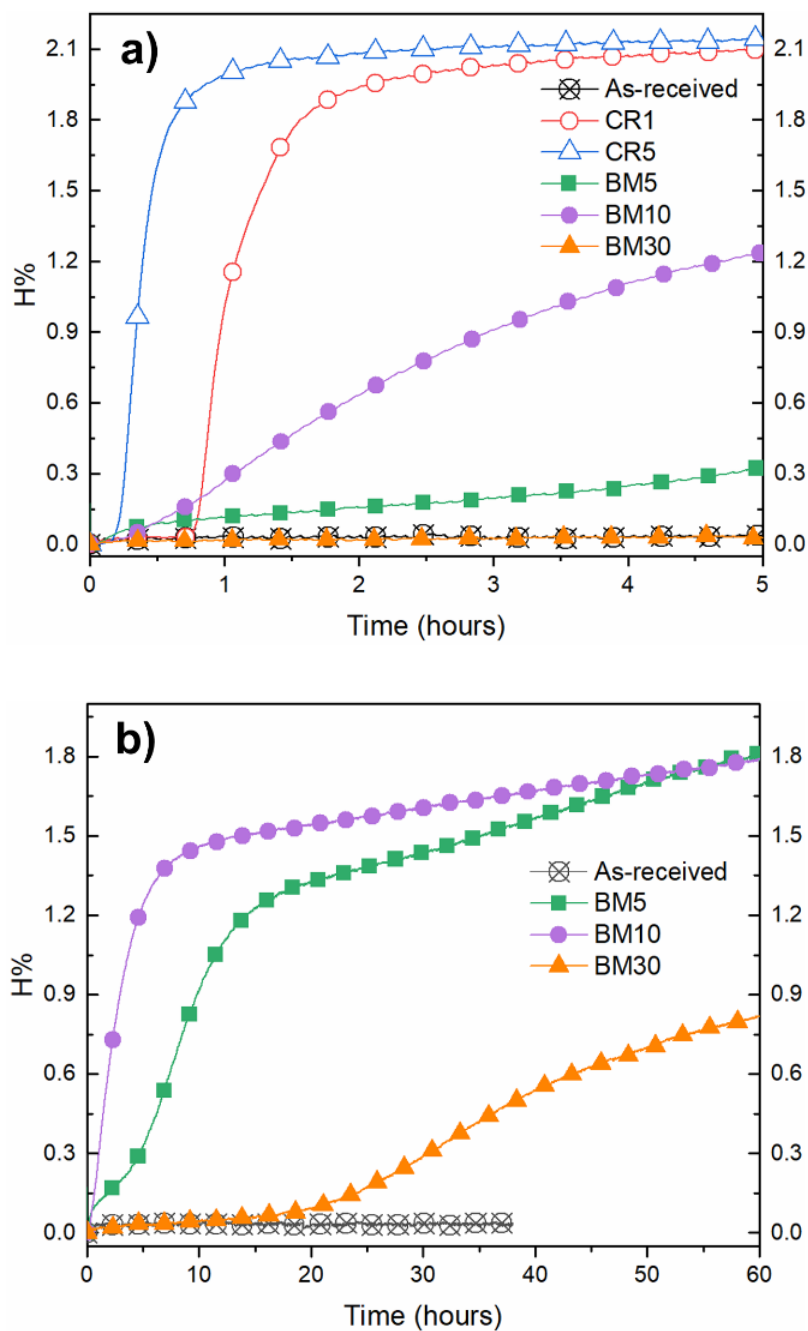


Figure 16. a) Activation under 20 bars of hydrogen pressure and at RT for all samples, b) long-term activation for BM5, BM10 and BM30.

3.3.4 Structural characterization

Figure 17a shows the XRD patterns all the powder for the conditions: As-received, CR1, CR5, BM5, BM10 and BM30. and desorption. In the patterns in Figure 17a the following phases were identified: TiFe, Ti₂Fe and a BCC phase. By correlating the phases identified by SEM and EDS, it can be assumed that the matrix and dark grey phase are respectively TiFe and Ti₂Fe. The presence of the BCC phase is more problematic and is discussed below with the Rietveld refinement results.

Figure 17b shows a side to side comparison between CR5 and CR5 after hydrogenation. In the pattern shown in Figure 17b for CR5 after dehydrogenation the TiFe phase was present and a new phase peak appeared at lower angles. There was no clear evidence of the Ti₂Fe phase.

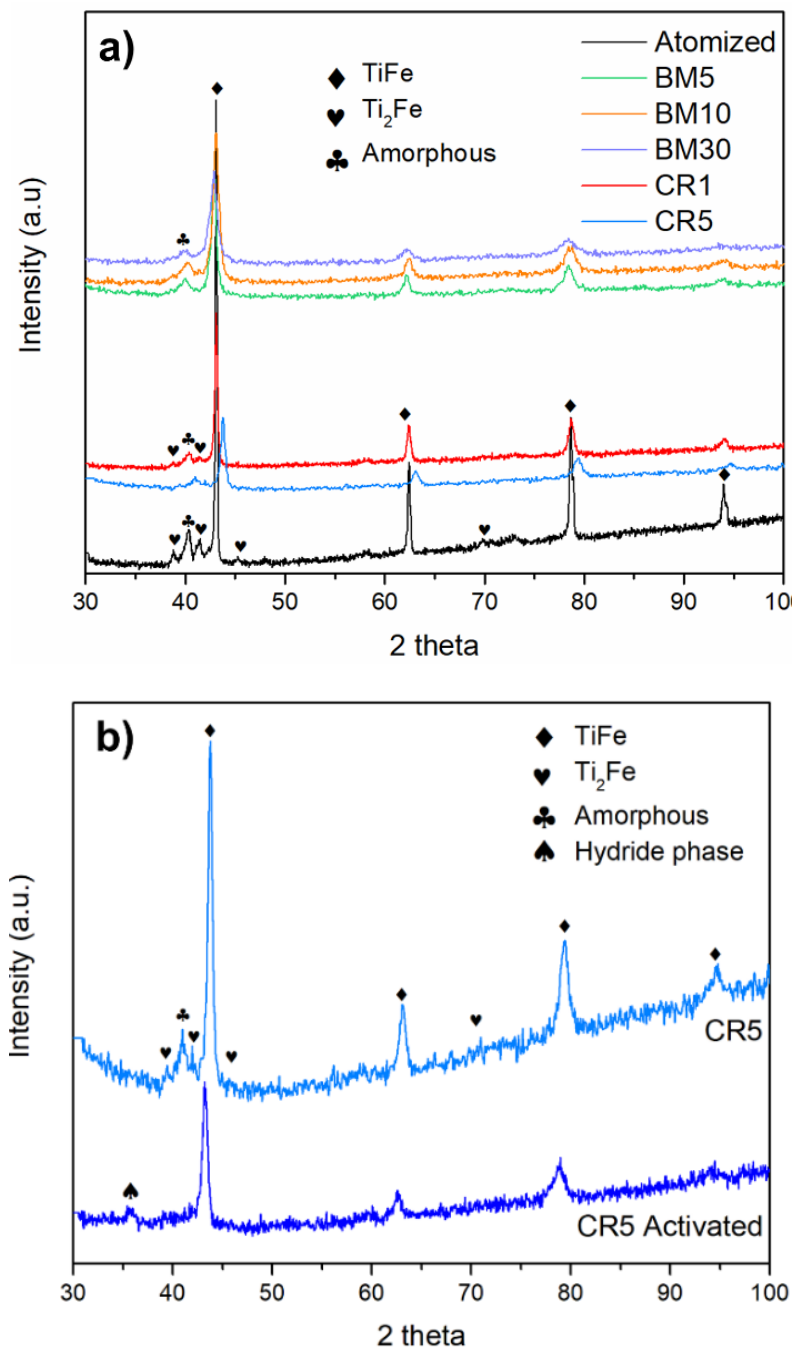


Figure 17. X-ray diffraction patterns of a) As-atomized powder, BM5, BM10, BM30, CR1 and CR5; b) CR5 before and after activation.

Table 4 presents the Rietveld refinement performed on the patterns of Figure 17a, as the cold rolled samples presented the best hydrogenation kinetic, the pattern for CR5-after activation and the patterns of the CR1-after activation (not shown in Figure 17b) were also refined. Starting with the as-atomized sample, three phases were identified:

TiFe, Ti₂Fe and a body-centered cubic (BCC) phase. They correspond respectively to the matrix, dark grey and bright phases seen in Figure 15. The Bragg's peaks of the BCC phase are very broad and almost buried in the background at high angles. This made the phase quantification difficult. However, by keeping the BCC phase abundance to a value of 4 wt.% as determined from the SEM observations, the abundance of the TiFe and Ti₂Fe were refined to be respectively 77% and 19% which agrees with what was determined from Figure 13b. The lattice parameter of Ti₂Fe phase was determined to be 11.4227 (2) Å and crystallite size of 6.6 (5) nm. As the BCC phase is of such low abundance, the crystallite size and microstrain could not be refined.

Table 4. Rietveld refinement of TiFe-phase and amorphous peak for conditions (the uncertainty on the last significant digit is given by the number in parenthesis).

	Crystallite size (nm)	Strain (μm)	Lattice parameter a (Å)
As-atomized	77 (3)	0.0417 (1)	2.9878 (1)
CR1	30 (1)	0.077 (4)	2.9882 (3)
CR5	19 (2)	0.14 (1)	2.9881 (9)
BM5	14.2 (6)	0.14 (1)	2.9896 (8)
BM10	12.6 (5)	0.20 (1)	2.9917 (9)
BM30	9. (6)	0.26 (2)	2.9892 (2)
CR1 after activation	25 (2)	0.158 (7)	2.9913(6)
CR5 after activation	18 (2)	0.22 (2)	2.988 (1)

The cold rolling and ball milling process decreased the crystallite size (CS) and increased the microstrain of the TiFe phase. As BM is an energetic process the reduction of CS was more important than for CR. CR5 showed the same strain effect as BM for only 5 minutes. Higher microstrain is also produced by BM. For all patterns, the BCC phase is

reduced to one identifiable Bragg peaks at 40 degrees. In fact, a better fit of the pattern is possible by using an amorphous phase instead. However, as we do not have other proofs of transformation of BCC to amorphous phase upon a few cold rolling passes or short ball milling times, the BCC was used for the refinements even if just one peak was visible. The Ti_2Fe phase is also affected and the peaks are too broad and the intensity too small for the refinement to accurately determine the CS and strain values.

The patterns of CR1 and CR5 after activation and desorption, showed an increase in microstrain in the TiFe phase. This increase comes from the expansion stress the lattice undergoes when hydrogen is introduced and later removed. After desorption a new Bragg peak appears at 35 degrees pointing to the formation of a stable hydride phase from one of the secondary phases. Since the secondary phases cannot be reliably discerned from the background, their hydrogen uptake cannot be estimated.

The Ti_2Fe metastable phase, has not been formally studied regarding its hydrogenation.

3.3.5 Comparison with other works

In order to discuss the influence of gas-atomization as a synthesis technique a comparison is made with the work done by Patel et al. were the same alloy composition, TiFe + 2 wt% Mn 4 wt% Zr, was obtained by induction melting under vacuum [67]. A conclusion of that work was that the Zr-rich secondary phase is responsible for the fast-first hydrogenation. In our atomized powder study, the sample required mechanical processing in order to have activation despite a much finer microstructure. However, as the atomized powder was exposed to the air for more than two months while the sample synthesized by induction melting was always protected against air exposure means that a definitive conclusion about the microstructure scale could not be reached at this moment. Future work will be performed to evaluate fresh powder without air exposition.

An interesting comparison could be made with Manna et al. work for the same system, TiFe+ 2 wt% Mn 4 wt% Zr [68]. Their samples were produced by induction melting, hand crushed and left in air for 7 and 30 days in order to see the effect of air exposure and the regeneration ability of CR and BM. The 7- and 30-day samples did not activate after air exposure but were able to activate after CR5 in air. As presented above, cold rolling was also beneficial to regenerate the atomized alloy exposed to the air for more than two months. However, as seen in Table 5 cold rolling was much more efficient on the atomized powder than on the induction melt one. The kinetic was faster and the capacity higher. The induction melted sample presented a loss of kinetics and capacity. This may be an indication that the effectiveness of cold rolling highly depends on the microstructure of the alloy.

Table 5. Effect of cold rolling on TiFe + 2 wt.% Mn + 4 wt.% Zr alloys.

	Synthesis process	Activation	Ref.
TiFe + 2 wt.% Mn 4 wt.% Zr (Fresh sample)	Induction melting	2wt.% 12 hours	[67]
TiFe + 2 wt.% Mn + 4 wt.% Zr (7 days in Air_CR5)	Induction melting	> 24 hours	[68]
(30 days in Air_CR5)		1.3wt.% 1.2wt.%	
TiFe + 2 wt.% Mn 4wt.% Zr (+60 days in Air_CR5)	Gas atomization	2.1wt.% 2 hours	This work

3.4 Conclusions

- Gas atomization resulted in TiFe matrix with finely distributed secondary phases. No eutectic microstructure was observed by SEM, as previously reported for the TiFe + 2wt%Zr + 4wt%Mn system produced by induction melting.

- The air exposed atomized powder did not absorb hydrogen and had to be regenerated by cold rolling or ball milling. Cold rolling was shown to be more efficient than ball milling for regeneration. The cold rolled samples absorbed hydrogen quickly and achieved full hydrogen capacity.
- From comparison with induction melted alloys, it seems that the effectiveness of cold rolling depends on the microstructure of the alloy.

CHAPTER IV

HYDROGENATION OF Ti_xFe_{2-x}-BASED ALLOYS WITH OVERSTOICHIOMETRIC Ti RATIO (X = 1.1, 1.15 AND 1.2)

The content of Chapter IV has been published in the *International Journal of Hydrogen Energy*. Volume 46, Issue 77, 8 November 2021, Pages 38363-38369. The article can be found in the following link: <https://doi.org/10.1016/j.ijhydene.2021.09.077>

4.1 Authors contributions

The authors of the article are Ms. Elena Ulate-Kolitsky, Doctor Bernard Tougas, and Doctor Jacques Huot.

Ms. Ulate-Kolitsky was responsible for the entirety of the experimental work presented in the article. The analysis of the results was done by Ms. Ulate-Kolitsky who was also responsible for the initial manuscript and finalizing any changes after discussion with the other authors. Dr. Tougas (Co-advisor) and Dr. Huot (Advisor) assisted with insightful discussion, comments, and suggestions on the article. Several versions of the manuscript were written until everyone was satisfied with the article. Dr. Huot played an important role finalizing the Rietveld refinement and guiding the research performed for the project.

4.2 Summary of the article

The hydrogenation behavior of Ti_xFe_{2-x}+ 4 wt.% Zr alloys, for x = 1.1, 1.15 and 1.2 has been investigated. The compositions were synthesized by arc melting. All compositions presented a multiphase microstructure with a TiFe-matrix along with secondary Ti₂Fe-like and Ti-rich BCC phases. The phase fraction varied with “x”.

Ti₂Fe is a metastable phase that was identified, it is thought that the alloying elements stabilize the structure and form a Ti₂Fe-like phase. The effect of the secondary phases on the activation kinetics and reversible capacity was studied. The hydrogenation of the secondary phases, specifically the Ti₂Fe-like phase has not been previously reported due to its difficulty to be synthesized in a large enough phase fraction.

The increase of titanium abundance decreases the plateau pressure of the alloy, but this comes with a loss of hydrogen capacity. The hydrogen absorbed by the TiFe phase for each composition matched the contribution expected for the corresponding phase abundance. The secondary phases formed stable hydrides Ti₂FeH_x and FCC, these were formed during activation and did not desorb under the experimental conditions. The stoichiometry of the stable hydrides was calculated based on the Rietveld refinement results.

Based on the results the first hydrogenation kinetics are fast due to the presence of the secondary phases which act as gateways for hydrogen. However, the reversible capacity is fully attributed to the TiFe phase.

4.3 Results and discussion

4.3.1 Morphology

Figure 18 shows the morphology of all studied compositions. They all show a light grey matrix and secondaries grey and bright regions. Increasing Ti from $x = 1.1$ to 1.15 does not drastically change the microstructure. The $x = 1.2$ composition shows a notable decrease of the total area of the secondary bright region. The surface area percentage of the different regions was measured by image analysis. For $x = 1.1$ and 1.15 compositions, the matrix covered about 69% of the area and the secondary regions 31%. In the $x = 1.2$ composition, the secondary bright region covered around 10%. Because of the similar contrast of the matrix and secondary grey region we were unable to quantify by image analysis the relative proportion of these two phases in $x = 1.2$.

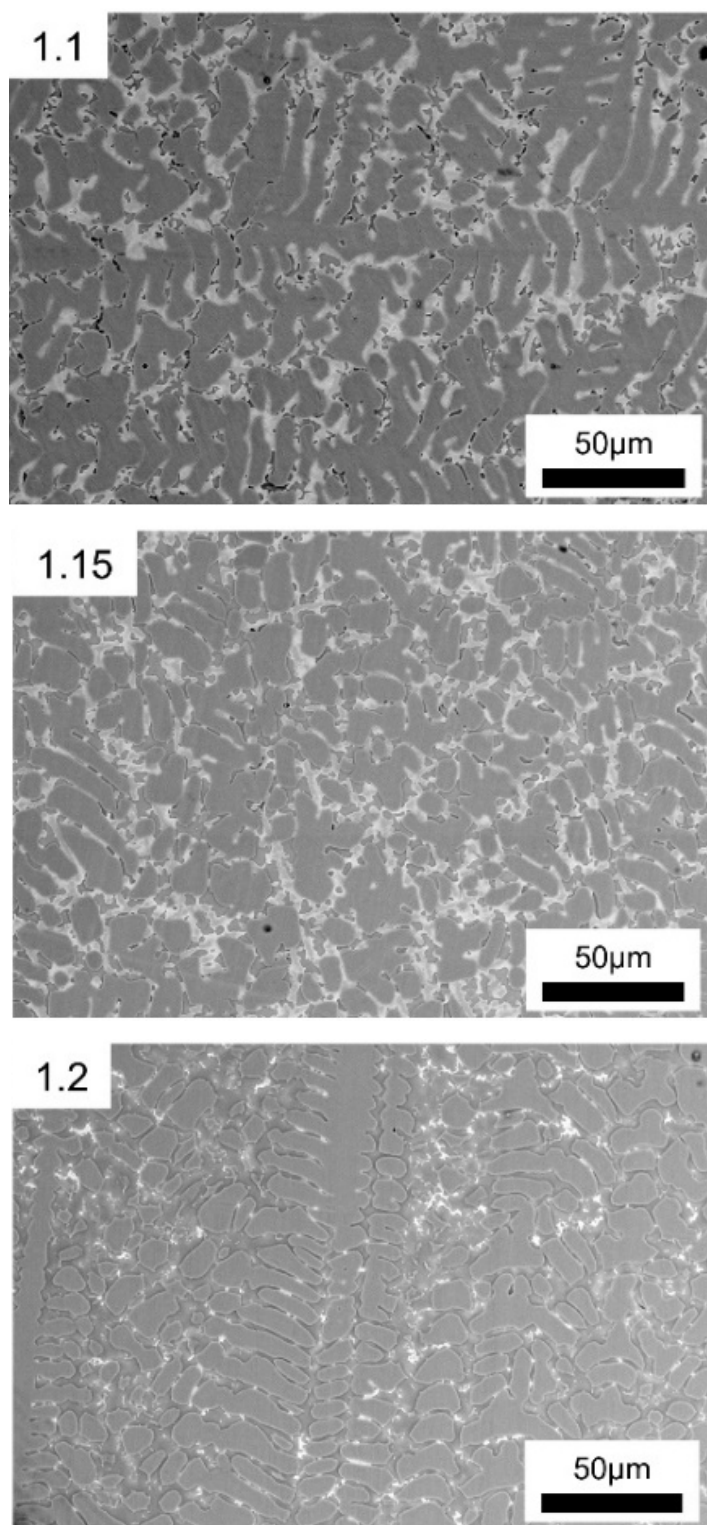


Figure 18. Backscattered electron micrograph of overstoichiometric-Ti, $\text{Ti}_x\text{Fe}_{2-x}$ + 4 wt.% Zr ($x = 1.1, 1.15$ and 1.2).

Figure 19 shows a secondary electron image of the $x = 1.1$ composition. It is noted that the grey region is topographically lower than the matrix. This means that the grey and the bright region is softer than the matrix.

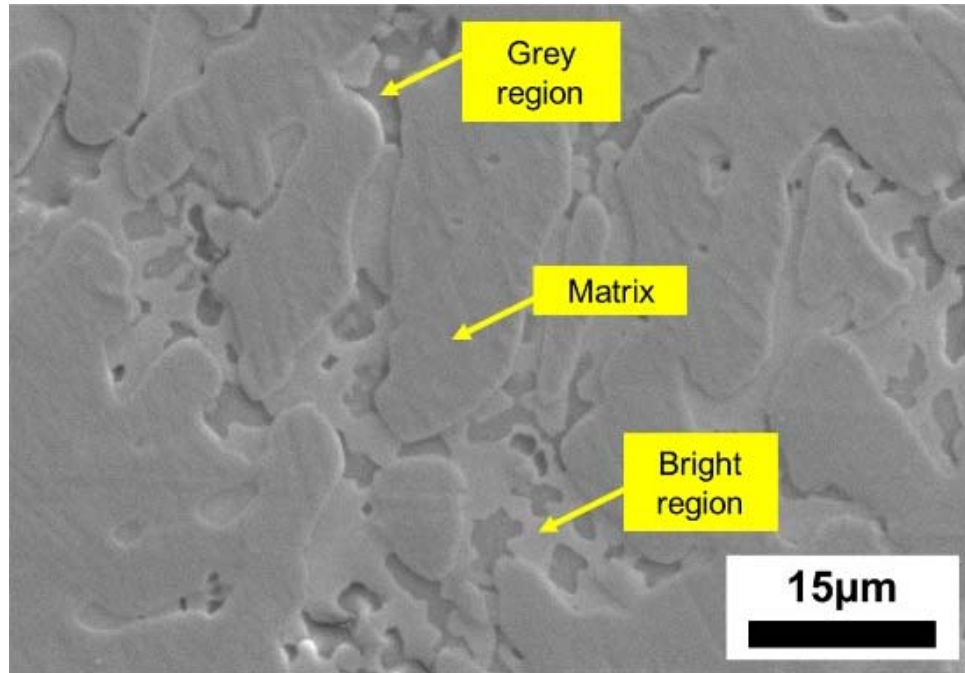


Figure 19. Secondary electron micrograph of $\text{Ti}_{1.1}\text{Fe}_{0.9} + 4 \text{ wt.}\% \text{ Zr}$.

4.3.2 Chemical analysis

Figure 20 shows the microstructure at higher magnification, the annotations on the image correspond to where the EDS point analysis were taken. The chemical composition of the matrix (1), secondary grey region (2) and secondary bright region (3) were measured by EDS point analysis.

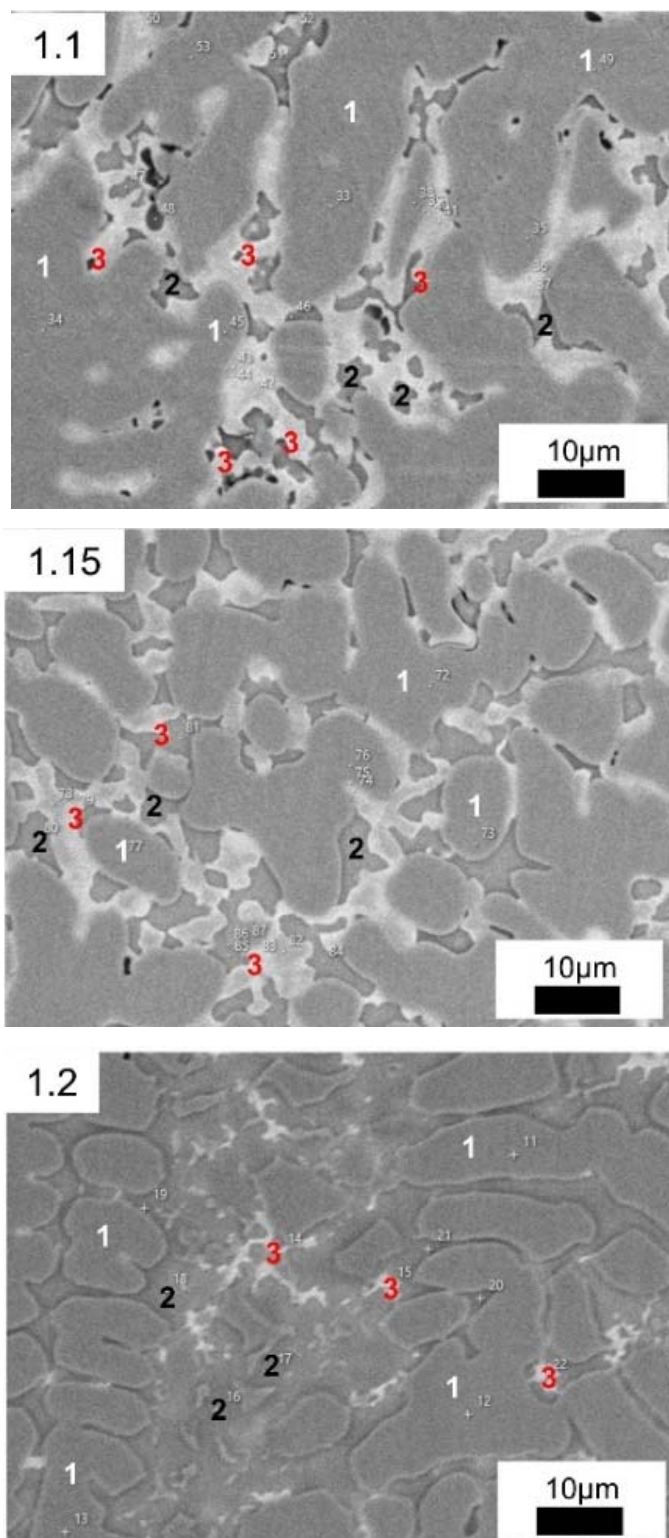


Figure 20. Backscattered electrons image of overstoichiometric-Ti, $Ti_xFe_{2-x} + 4$ wt.% Zr ($x = 1.1, 1.15$ and 1.2). Spectrum 1: matrix; spectrum 2: grey region; spectrum 3: bright region.

Table 6 presents the EDS chemical analysis for each region. The matrix for the three compositions has the TiFe stoichiometry with only a small substitution of Ti by Zr in the $x = 1.1$ alloy. The secondary grey region composition is essentially the same for the three alloys.

Table 6. EDS analysis of overstoichiometric-Ti, $\text{Ti}_x\text{Fe}_{2-x} + 4\text{wt.}\% \text{ Zr}$ ($x = 1.1, 1.15$ and 1.2).

X	Spectrum	Region	Average at.%		
			Fe	Ti	Zr
1.1	1	Matrix	51	48	1
	2	Grey region	23	73	4
	3	Bright region I	32	60	8
1.15	1	Matrix	48	52	0
	2	Grey region	25	71	4
	3	Bright region I	33	60	7
1.2	1	Matrix	48	52	0
	2	Grey region	21	75	4
	3	Bright region II	24	61	15

4.3.3 Hydrogenation kinetics and PCI

Figure 21 shows the activation curves for the as-cast alloys. All samples absorbed hydrogen relatively quickly, reaching full capacity after about 2 hours. The activation capacity reached by all samples is higher than the 1.86 wt.% H capacity of pure TiFe. This means that the secondary phases are also absorbing hydrogen.

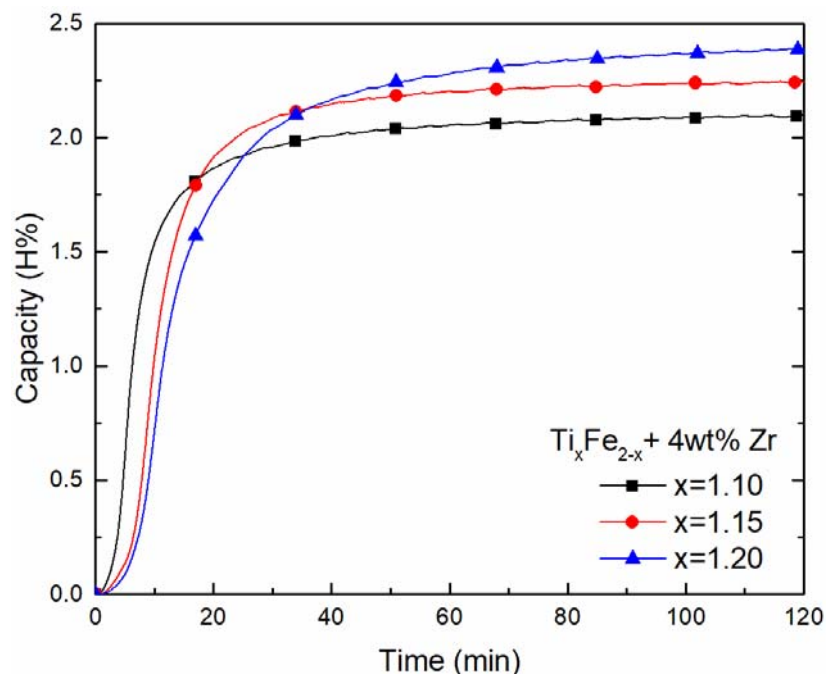


Figure 21. Activation of overstoichiometric-Ti, $\text{Ti}_x\text{Fe}_{2-x} + 4 \text{ wt.}\% \text{ Zr}$ ($x = 1.1, 1.15$ and 1.2).

Figure 22 presents the pressure composition isotherm (PCI) curves after activation and desorption. The absorption 1st plateau ($\sim 200 \text{ kPa}$) for all samples is at a lower pressure than the ones reported for pure-TiFe where the absorption plateau is $\sim 500 \text{ kPa}$. However, this drop in plateau pressure has been previously reported for $\text{TiFe} + X \text{ wt.}\% \text{ Zr}$ [69]. Regarding the effect of increasing x , it slightly stabilizes the hydride as indicated by a lower pressure of the plateau. The plateau pressure decreasing with the increase of x value is possibly due to the slight change of composition of TiFe phase.

The small 'loop, seen at high pressure for the three isotherms is due to experimental artefact. At high pressure, there is a systematic shift of the pressure due to the hysteresis of the strain gauge. This loop has also the effect of shifting the capacity toward lower value. As the effect is accumulative, this is the reason for the small negative value of the capacity at the end of desorption.

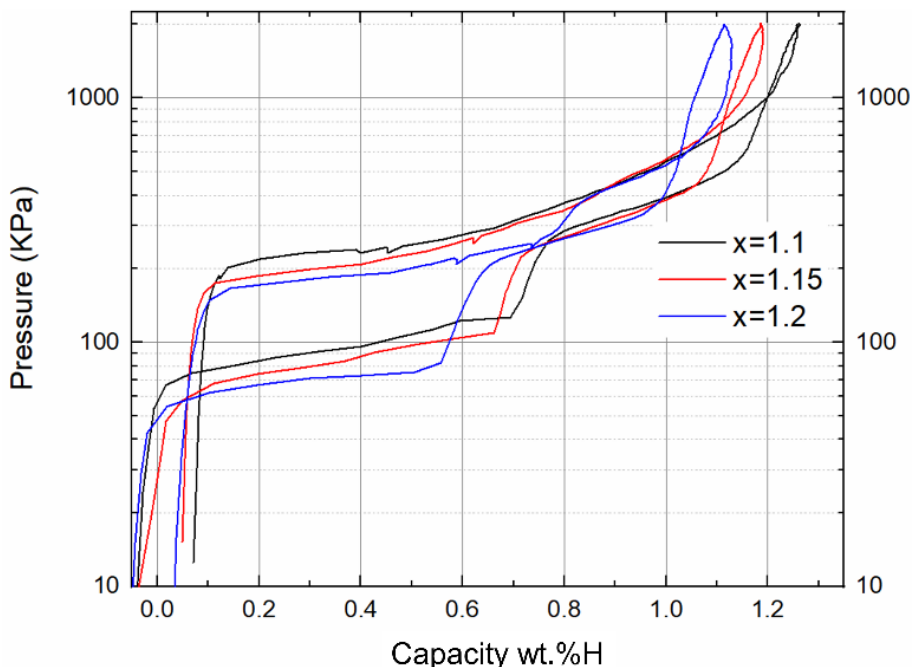


Figure 22. Pressure Composition Isotherm (23 °C) of overstoichiometric-Ti, $\text{Ti}_x\text{Fe}_{2-x}$ + 4 wt.% Zr ($x = 1.1, 1.15$ and 1.2).

4.3.4 Structural characterization

Figure 23 shows the XRD pattern of all compositions. The main phase identified is TiFe which confirms the EDS measurements of the matrix. The other peaks were indexed as a Ti_2Fe phase and a BCC phase. This three-phase microstructure matches the phase equilibria reported previously reported by Zeng et al. for the 60.6 at.% Ti, 34.6 at.% Fe and 4.8 at.% Zr alloy. This alloy reportedly presented three stable phases TiFe, a cubic phase called τ_4 of composition (33.3 at.% Fe, 50.4 – 60.9 at% Ti) and a β (Ti,Zr) phase (Structure type W) [38]. As indicated in Table 6, the secondary bright region for compositions $x = 1.1$ and 1.15 has a Fe abundance close to 33 at.%. This matches perfectly the τ_4 line composition discussed by Zeng et al. [38]. Thus, the secondary region may be associated with the Ti_2Fe -like phase where Zr substitutes Ti and can be written as $(\text{Ti}, \text{Zr})_2\text{Fe}$. For the $x = 1.2$, as seen in Figure 18, the secondary bright region has a much smaller area and a different chemical composition. This is reflected in the diffraction pattern where the relative intensities of the Ti_2Fe peaks are reduced. In the case of $x = 1.2$ the stoichiometry associated with the bright region II phase in Table 6 does not match the

line compound, τ_4 , identified by Zeng et al. Nonetheless in the $x = 1.2$ pattern the phase Ti_2Fe was indexed although, we could not be affirmative about the presence of this phase because of the weak peak intensities.

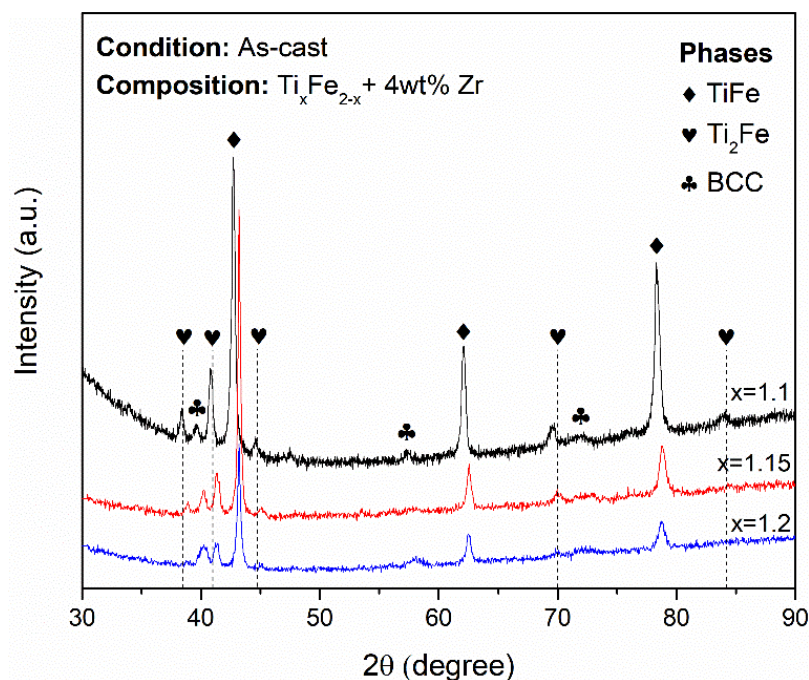


Figure 23. X-ray diffraction patterns of overstoichiometric-Ti, $Ti_xFe_{2-x} + 4$ wt.% Zr for $x = 1.1, 1.15$ and 1.2 .

The BCC structure is associated to the secondary grey region reported in Table 6. The averaged composition of the BCC phase 23 at.% Fe, 73 at.% Ti and 4 at.% Zr is close to that of the $\beta(Ti,Zr)_{BCC}$ phase in Zeng et al.'s work 17,5 at.% Fe, 79.3 at% Ti and 3.2 at.% Zr.

Table 7 shows the Rietveld refinement results of the XRD patterns shown in Figure 23. For the compositions $x = 1.1$ and 1.15 , the phase abundance estimated from EDS agrees with the phase fractions calculated from Rietveld refinement. For the $x = 1.2$ compositions, the situation is not as straightforward. The backscattered images show only 10% of the secondary bright region as measured by image analysis. This does not match quantitatively the 18.8 wt.%. However, as mentioned above, because of the weak Bragg's peaks we could not be affirmative that this phase has a Ti_2Fe structure. As seen in Table 7,

the change of composition leads to an increase of the lattice parameter with x . A bigger lattice parameter means a bigger interstice for hydrogen and thus a lower plateau pressure as shown in Figure 22.

Table 7. Rietveld refinement of overstoichiometric-Ti, $\text{Ti}_x\text{Fe}_{2-x} + 4 \text{ wt.}\% \text{ Zr}$ where, $x = 1.1, 1.15$ and 1.2 (the uncertainty on the last significant digit is given by the number in parentheses).

	Phase	Phase Fraction wt. %	Lattice parameters “a” (Å)	Unit cell volume (Å³)
$x = 1.1$	TiFe	68	2.9844 (1)	26.582 (4)
	Ti ₂ Fe	28	11.451 (1)	1501.4 (4)
	BCC	4	3.205 (1)	32.91 (3)
$x = 1.15$	TiFe	65	2.9867 (2)	26.642 (6)
	Ti ₂ Fe	25	11.456 (2)	1503.4 (7)
	BCC	10	3.2021 (9)	32.83 (3)
$x = 1.2$	TiFe	57	2.9895 (4)	26.71 (1)
	Ti ₂ Fe	19	11.469 (3)	1509 (1)
	BCC	24	3.203 (1)	32.85 (3)

Using the phase abundance of the TiFe phase determined by Rietveld refinement, the hydrogen absorption contribution of this phase for $x = 1.1, 1.15$ and 1.2 would respectively be 1.26 wt.% H, 1.21 wt.% H and 1.06 wt.% H. Thus, the missing capacity should be coming from the secondary phases. All compositions ($x = 1.1, 1.15, 1.2$) were cycled 10 times to corroborate that the reversible capacity was stable (1.21 wt.% H, 1.2 wt.% H and 1.1 wt.% H respectively). The reversible capacity closely matches the contribution calculated for the TiFe phase according to the Rietveld refinement.

Figure 24 shows the XRD patterns of the samples after cycling (10 cycles). The phases identified are TiFe, a Ti_2Fe -like phase and an FCC phase.

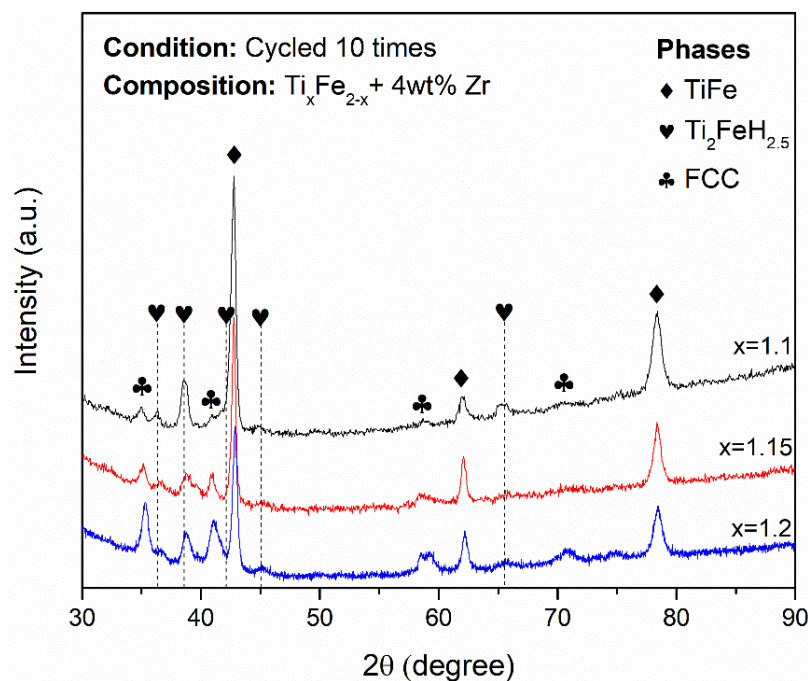


Figure 24. X-ray diffraction patterns of the cycled overstoichiometric-Ti, $\text{Ti}_x\text{Fe}_{2-x} + 4 \text{ wt.}\% \text{Zr}$ ($x = 1.1, 1.15$ and 1.2).

Table 8 shows the crystal structure parameters for each phase identified in Figure 24. Considering that the structure type of the Ti_2Fe phase is Ti_2Ni , we can expect that the Ti_2Fe -like hydride presents the same structure as Ti_2Ni hydride ($\text{Ti}_2\text{NiH}_{2.5}$, Fd-3m, Pearson's symbol cF96) [70]. The volume expansion by a Ti_2Fe -like phase due to hydrogen uptake has been previously reported for two alloys that presented a $(\text{Ti,Zr})_2\text{Fe}$ minor phase. The volume change was reported as 16.4% and 24.4% [37].

The stoichiometry of the hydrided Ti_2Fe -like phase for the $x = 1.1, 1.15$ and 1.2 compositions were determined by the unit cell volume increase due to the hydrogen uptake. In the case of $x = 1.1$ the volume increase is 266 \AA^3 (~16%). Considering 32 formula units per unit cell, this gives a volume per formula unit of 8.3 \AA^3 . Assuming that a single hydrogen atom usually occupies a volume between 2 and 3 \AA^3 , this gives a range of stoichiometry between Ti_2FeH_4 (2.6 wt.% H) and $\text{Ti}_2\text{FeH}_{2.8}$ (1.8 wt.% H).

Similar range has been found for the other two compositions. Using the phase abundance from Table 7, the contribution of the Ti_2Fe -like phase for sample $x = 1.1$ would then be 0.72 - 0.5 wt.% H. Similarly, the capacity coming from Ti_2Fe -like phase for $x = 1.15$ is between 0.57 and 0.39 wt.% H and for $x = 1.2$ it is between 0.5 and 0.34 wt.% H.

It is well known that the dihydride of a BCC phase is FCC. Thus, the origin of the FCC could be directly related to the presence of a BCC phase in the as-cast alloy. Considering the phase fraction of BCC given in Table 7, the full capacity of the BCC phase for samples, $x = 1.1$, 1.15 and 1.2 are respectively 3 wt.% H, 5.6 wt.% H and 3.8 wt.% H. As the H/M of the FCC phase is 2, the 'theoretical' capacity of the FCC should be 3.7 wt.% H which agrees relatively well with the estimation from X-ray diffraction patterns.

Table 8. Crystal structure parameters of cycled overstoichiometric-Ti, $Ti_xFe_{2-x} + 4$ wt.% Zr where, $x = 1.1, 1.15$ and 1.2 (the uncertainty on the last significant digit is given by the number in parenthesis).

	Phase	Lattice parameters (Å)	Unit cell volume (Å ³)
x = 1.1	TiFe	2.9877 (3)	26.670 (7)
	Ti ₂ FeH _x	12.092 (2)	1768 (1)
	FCC	4.421 (2)	86.4 (1)
x = 1.15	TiFe	2.9868 (4)	26.65 (1)
	Ti ₂ FeH _x	12.010 (7)	1732 (3)
	FCC	4.418 (2)	86.2 (1)
x = 1.2	TiFe	2.9910 (4)	26.75 (1)
	Ti ₂ FeH _x	12.094 (4)	1769 (2)
	FCC	4.4157 (9)	86.10 (5)

4.3.5 Comparison with previous works

Table 9 shows the activation results of previous studies with different $Ti_xFe-Zr_y-M_z$ compositions, and the respective secondary phases reported. From a purely kinetic point of view the samples with Ti overstoichiometry ($x = 1.1, 1.15$ and 1.2) all present the fastest activation. The work done on $TiFe + 2$ wt.% Mn + 4 wt.% Zr [67], presents the most similar phase fractions of TiFe and Ti₂Fe phases however the kinetics are slower. This points to a synergetic effect due to presence of a BCC phase alongside Ti₂Fe phase. Also, the capacity increase with Ti points to the BCC phase absorbing hydrogen during activation. However, the kinetics are not further improved by the increase of BCC phase. It is important to keep in mind how the uptake on hydrogen by the secondary phases may ultimately affect the reversible capacity because of the high stability of the secondary hydride phase.

Table 9. Summary of activation results of previous studies and current work.

Composition	Synthesis	Phases present	Capacity	Ref.
TiFe + 4 wt.% Zr	Arc-melting No heat treatment	TiFe	1.45 wt.% H	[36]
		Minor secondary phases not identified	7 h 2.5 MPa @25 °C	
TiFe + 4 wt.% Zr	Arc-melting Annealed 1173 K – 24 h	TiFe	0.1 wt.% H	[71]
		Minor secondary phases not identified	6 h (poor kinetics) 2 MPa @25 °C	
Ti _{1.2} Fe	Arc-melting Homogenization Annealing 1473 K – 10 h	TiFe (91.8 wt.%)	2.1 wt.% H	[44]
		Ti ₂ Fe (2.8 wt.%) Ti ₄ Fe _(BCC) (5.4 wt.%)	6 hours 4 MPa @25 °C	
TiFe + 2 wt.% Mn + 4 wt.% Zr	Induction melting No heat treatment	TiFe (70 wt.%)	2 wt.% H	[66]
		Ti ₂ Fe(28 wt.%) Ti (2 wt.%)	~10 h 2 MPa @25 °C	
TiFe _{0.85} Mn _{0.05}	Induction melting Annealed 1273 K – 168 h Water quenched	TiFe (94.8 wt.%)	1.73 wt.% H	[72]
		B-Ti (2.8 wt.%) Ti ₄ Fe ₂ O (2.4 wt.%)	Total time 7 h with 6 h incubation 2.5 MPa @25 °C	
Ti _{1.1} Fe _{0.9} + 4 wt.% Zr	Arc-melting No heat treatment	TiFe (68 wt.%)	2.1 wt.% H	Current work
		Ti ₂ Fe (28 wt.%) BCC (4 wt.%)	2 h 2 MPa @25 °C	
Ti _{1.15} Fe _{0.85} + 4 wt.% Zr	Arc-melting No heat treatment	TiFe (65 wt.%)	2.25 wt.% H	Current work
		Ti ₂ Fe (25 wt.%) BCC (10 wt.%)	2 h 2 MPa @25 °C	
Ti _{1.2} Fe _{0.8} + 4 wt.% Zr	No heat treatment	TiFe (57 wt%)	2.4 wt.%H	Current work
		Ti ₂ Fe (19 wt%) BCC (24 wt%)	2 h 2 MPa @25 °C	

4.4 Conclusions

Alloys of composition $\text{Ti}_x\text{Fe}_{2-x} + 4 \text{ wt.}\% \text{ Zr}$ alloys, with $x = 1.1, 1.15$ and 1.2 were investigated. We found that all alloys are composed of a main TiFe phase with zirconium-rich secondary phases. The secondary phases were identified as a Ti_2Fe -like phase and a Ti-rich BCC phase. The secondary phases match the τ_4 and $\beta(\text{Ti,Zr})$ phases described by Zeng et al. The first hydrogenation kinetics are fast due to the presence of these secondary phases which act as gateways for hydrogen. Both secondary phases form stable hydrides that do not desorb under the present experimental conditions (vacuum at room temperature). The hydride capacity of all phases was determined and match well with the reversible capacity measured experimentally. The reversible capacity is fully attributed to the TiFe phase. Pressure-composition isotherms taken at room temperature shown that increasing the relative amount of titanium makes the alloy more stable by increasing the Ti content in the TiFe phase.

CHAPTER V

FIRST HYDROGENATION KINETICS OF INDUCTION MELTED TIFE + 20 WT.% TI ($Ti_{1.2}Fe_{0.85}$)

The content of this chapter will be submitted to the *International Journal of Hydrogen Energy*.

5.1 Contribution des auteurs

The authors of the article are Ms. Elena Ulate-Kolitsky, Doctor Bernard Tougas, and Doctor Jacques Huot.

Ms. Ulate-Kolitsky was responsible for the entirety of the experimental work presented in the article. The analysis of the results was done by Ms. Ulate-Kolitsky who was also responsible for the initial manuscript and finalizing any changes after discussion with the other authors. Dr. Tougas (Co-advisor) and Dr. Huot (Advisor) assisted with insightful discussion, comments, and suggestions on the article. Dr. Bernard Tougas played a key role with the synthesis of the induction-melted ingot.

5.2 Summary of the article

The effect of titanium overstoichiometry was studied to determine if the activation kinetics can be improved without addition of Zr or Mn. The alloy of composition $Ti_{1.2}Fe_{0.8}$ was synthesized by induction-melting into a 9 kg ingot. The alloy presented the same three-phase system as the arc-melted, $Ti_xFe_{2-x} + 4$ wt.% Zr ($x = 1.1, 1.15, 1.2$) alloys and $Ti_{1.2}Fe$ alloy studied in previous works: a main TiFe phase, a secondary Ti_2Fe -like phase and a Ti-rich BCC phase. Unlike the arc melted alloys the induction melted $Ti_{1.2}Fe_{0.8}$ required cold rolling to achieve activation. However, it did so with good kinetics, reaching

saturation in ~ 6 h at room temperature and under 20 bars of hydrogen pressure. As the microstructure of induction-melted ingot is different than the structure of laboratory scale alloys synthesized by arc melting, a small 3-gram sample of $\text{Ti}_{1.2}\text{Fe}_{0.8}$ was synthesized by arc-melting. This sample could be activated without the need for cold rolling. This showed how the microstructure obtained by induction melting is not as advantageous as the finer microstructure obtained by arc-melting but is still able to activate under mild conditions after cold rolling. The microstructure is shown to be of special importance for the activation behaviors.

5.3 Results and discussion

5.3.1 Morphology

Figure 25 shows the microstructure of the induction melted $\text{Ti}_{1.2}\text{Fe}_{0.8}$ 9 kg ingot. Three regions are observed in the micrograph: a bright main region (a) and two grey regions. A grey region (b) that consists of rounded areas that are in contact with the bright region and a dispersed dark-grey region (c). The phase fractions were measured by image processing. The main bright region accounts for 58% of the micrographs area and the secondary grey and dark-grey regions for 12 and 30% respectively.

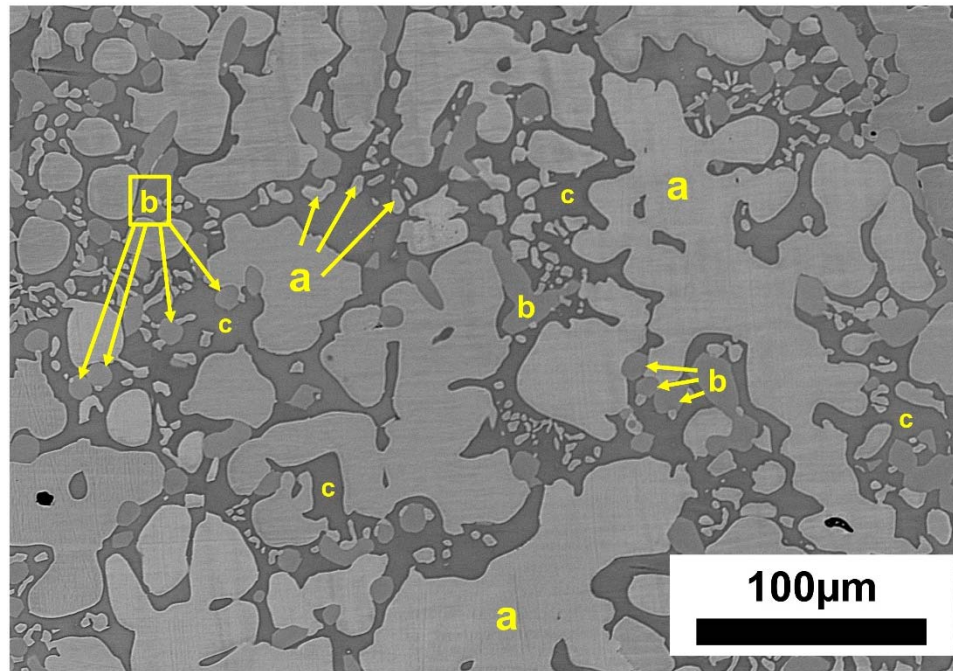


Figure 25. Backscattered electron micrograph of the induction melted Ti_{1.2}Fe_{0.8} alloy.

5.3.2 Chemical analysis

The difference in contrast between the regions reflects the difference in composition. Figure 26 shows a higher magnification image of the regions analyzed by EDS. The chemical composition of the overall alloy and each specific region was measured, and the results are shown in Table 10.

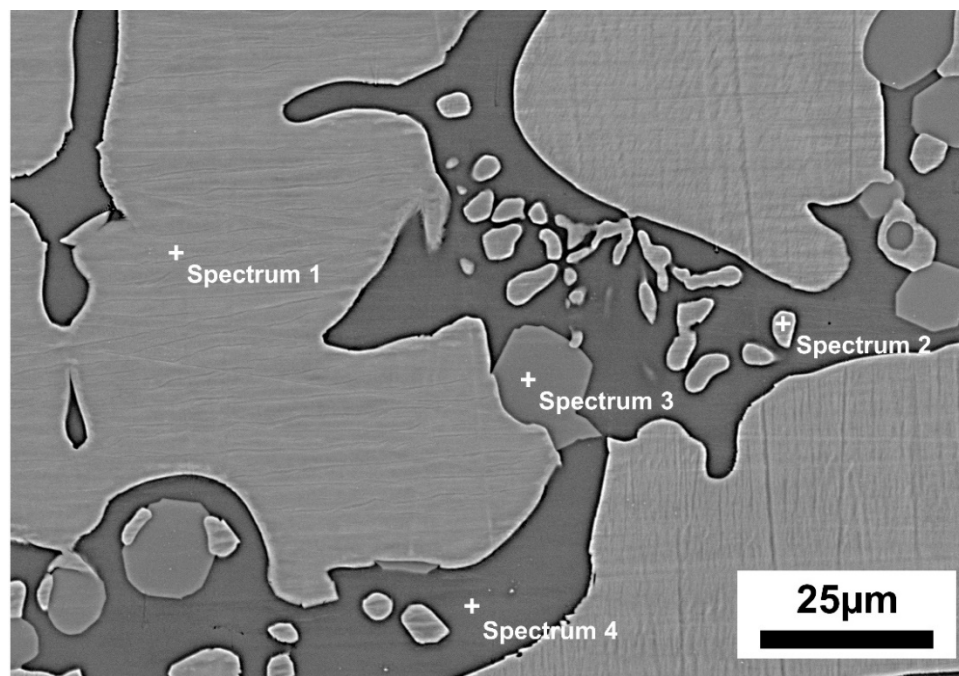


Figure 26. Backscattered electron micrograph of the induction melted Ti_{1.2}Fe_{0.8} alloy and EDS point spectra.

Table 10. EDS analysis of induction melted $\text{Ti}_{1.2}\text{Fe}_{0.8}$ alloy (uncertainty is ± 1 for all values).

	Region	Ti wt.%	Fe wt.%
Nominal composition	N/A	56	44
Overall composition	N/A	59	41
Spectrum 1 and 2	Bright	49	51
Spectrum 3	Grey	63	37
Spectrum 4	Dark-grey	79	21

The overall composition measurement shows how the real composition of the alloy is $\text{Ti}_{1.26}\text{Fe}_{0.74}$ instead of the nominal composition $\text{Ti}_{1.2}\text{Fe}_{0.8}$. This difference is not uncommon when working with industrial synthesis. Since the difference is small we will use the nominal composition in our discussion. The main phase (Spectrum 1 and 2) matches the composition for the intermetallic TiFe. The secondary grey phase (Spectrum 3) presents a composition close to Ti_2Fe and the secondary dark-grey phase (Spectrum 4) is Ti-rich.

5.3.3 Activation kinetics

Figure 27a and b show the activation curves of the $\text{Ti}_{1.2}\text{Fe}_{0.8}$ alloy at different times in the x-axis. The as-cast sample did not activate after over 20 hours under 2000 kPa of hydrogen pressure. The sample cold rolled 5 times in air (CR5) presented fast activation kinetics reaching ~ 2.6 wt.% H with an incubation period of ~ 40 minutes and saturation in ~ 6 hours.

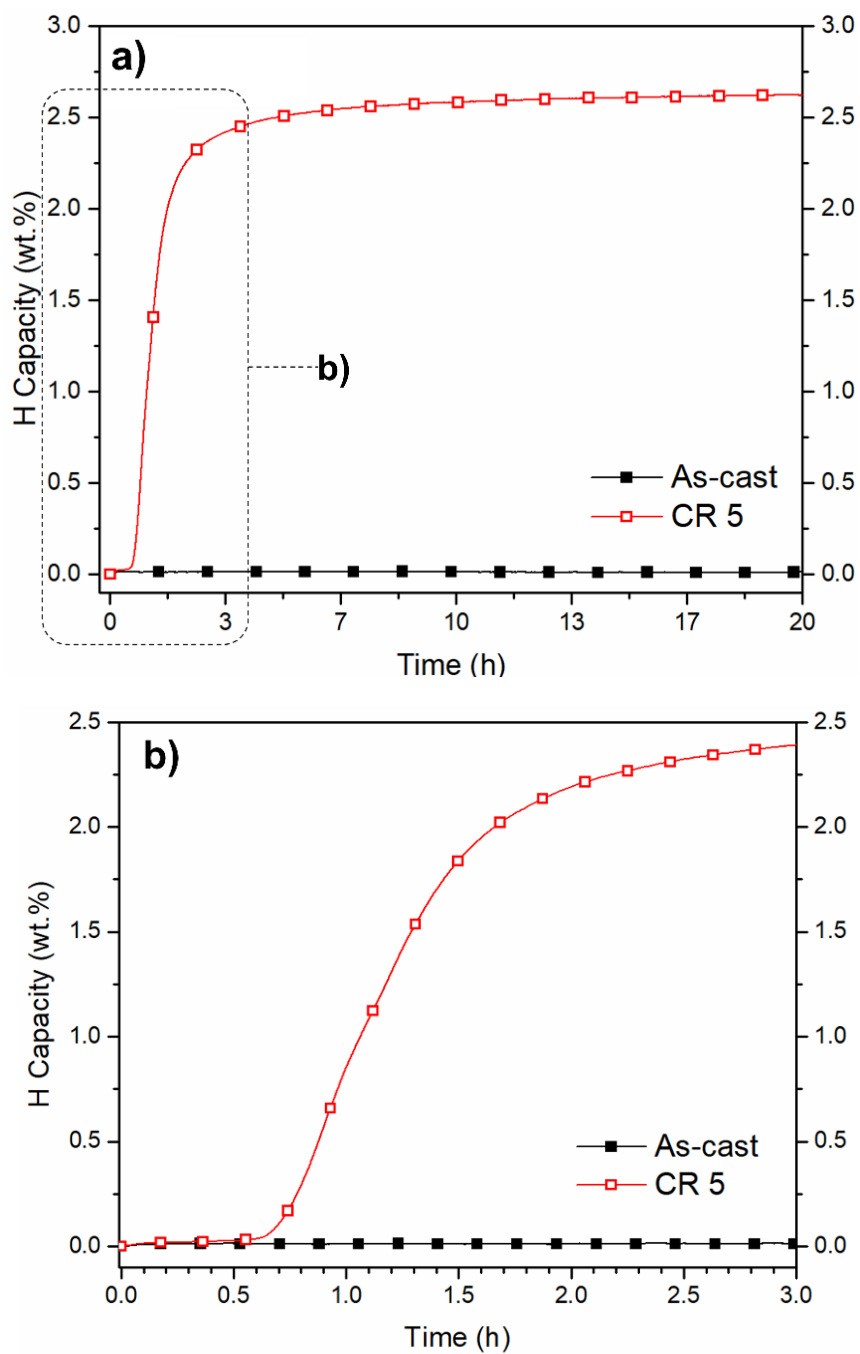


Figure 27. Activation curve of $Ti_{1.2}Fe_{0.8}$ with and without cold rolling a) 20 hours, b) 3 hours.

5.3.4 Structural characterization

Figure 28 shows the XRD patterns of the $\text{Ti}_{1.2}\text{Fe}_{0.8}$ alloy in the as-cast condition. The phases identified in the as-cast condition are TiFe, Ti_2Fe and BCC. By correlating the phases identified by EDS, it can be assumed that the main region, grey region, and dark-grey region respectively correspond to TiFe, Ti_2Fe and BCC phases. Table 11 presents the results from the Rietveld refinement performed on the as-cast condition. The abundance of each phase from image analysis were included for comparison. The phase abundance on the refinement results is higher than the one measured by image analysis however, it is important to keep in mind that Rietveld refinement reports the wt.%. If the phase fraction measured by image analysis is multiplied by the density of each phase ($\text{TiFe}\rho = 6.6 \text{ g/cm}^3$, $\text{Ti}_2\text{Fe}\rho = 5.7 \text{ g/cm}^3$, $\text{BCC}\rho (\text{Ti}_{80\%}\text{Fe}_{20\%}) = 5.2 \text{ g/cm}^3$) and each result is divided by the sum the phase fraction obtain is 63.3 wt.% TiFe, 11.2 wt.% Ti_2Fe and 25.5 wt.% BCC. This an almost exact match to the Rietveld refinement.

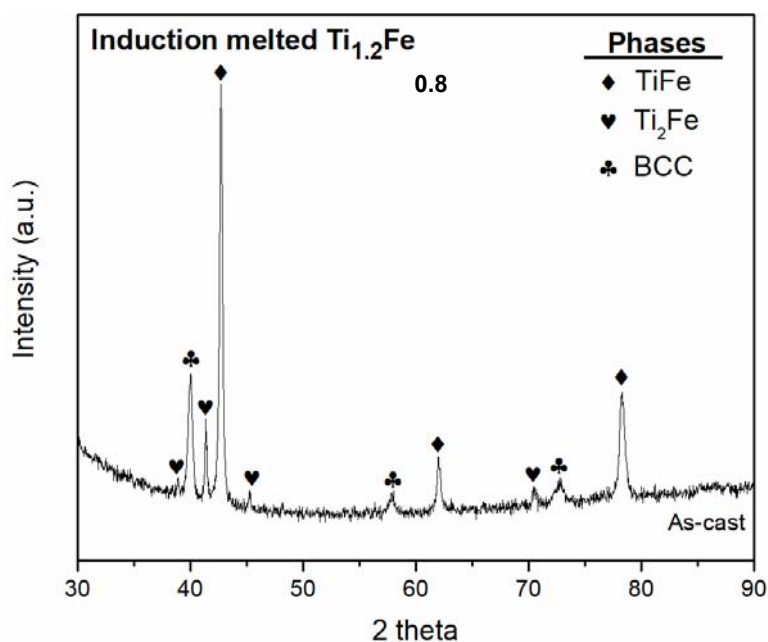


Figure 28. X-ray diffraction patterns of the induction melted $\text{Ti}_{1.2}\text{Fe}_{0.8}$.

Table 11. Rietveld refinement of the as-cast induction melted $Ti_{1.2}Fe_{0.8}$ (the uncertainty on the last significant digit is given by the number in parenthesis).

Phase	Phase Fraction Image analysis	Phase Fraction Rietveld Refinement	Lattice parameters “a” (Å)
TiFe	58	64	2.9904 (2)
Ti ₂ Fe	12	10	11.328 (1)
BCC	30	26	3.1850 (3)

Figure 29 shows the XRD patterns of the $Ti_{1.2}Fe_{0.8}$ alloy in the CR5 condition and the CR5 post-activation. The phases identified in the CR5 condition match those identified in the as-cast condition (TiFe, Ti₂Fe and BCC) with the difference that the peaks are slightly broader which is typical for samples that have undergone mechanical deformation. The phases identified in the CR5 post-activation patterns are TiFe, Ti₂FeH_x and FCC. The hydride phases Ti₂FeH_x and FCC are both stable hydrides formed during activation. It is well known that the dihydride of a BCC phase is FCC. Thus, the origin of the FCC could be directly related to the presence of a BCC phase in the as-cast alloy. The stable hydrides identified match those previously reported [73].

Table 12 shows the crystal structure parameters of the Ti₂Fe and Ti₂FeH_x refined for the CR5 and the CR5-post activation conditions respectively. The volume expansion of the Ti₂Fe phase on the CR5 post-activation condition was determined to be 21% this expansion is close to the one previously reported by Faisal et al. for their hydrated Ti₂Fe-like phase, 16.4% and 24.4% [37]. The stoichiometry of the Ti₂FeH_x was determined by the unit cell volume increase. The volume increase is 305 Å³, since there are 32 formula units per unit cell, this gives a volume per formula unit of 9.5 Å³. Assuming that a single hydrogen atom usually occupies a volume between 2 and 3 Å³, this gives a range of stoichiometry between Ti₂FeH_{4.75} (3.09 wt.% H) and Ti₂FeH_{3.2} (2.08 wt.% H).

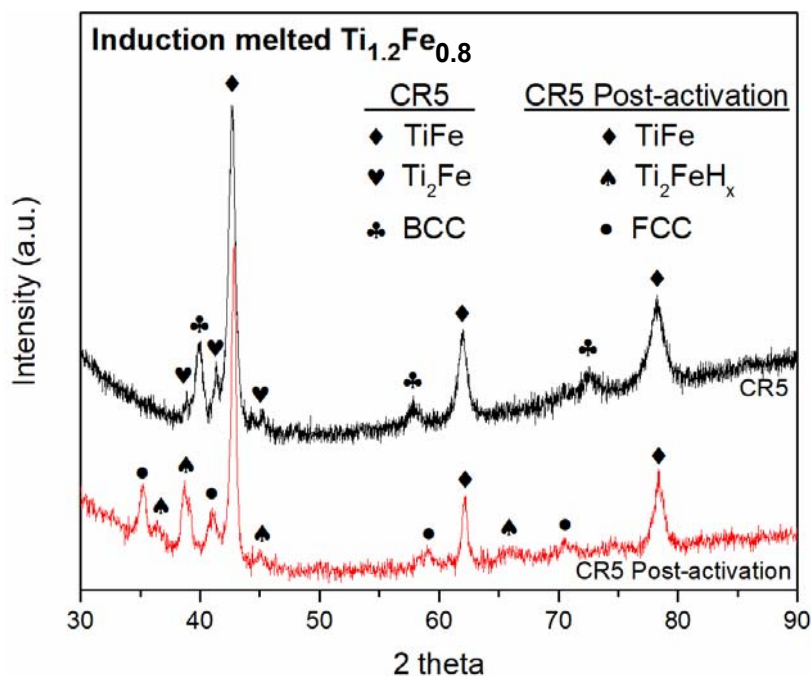


Figure 29. X-ray diffraction patterns of the induction melted $Ti_{1.2}Fe_{0.8}$ cold rolled 5 passes (CR5) and CR5 post-activation.

Table 12. Crystal structure parameters of Ti_2Fe and Ti_2FeH_x phases identified in Figure 30 (the uncertainty on the last significant digit is given by the number in parenthesis).

CR5			CR5 Post-activation		
Phase	Lattice parameters (Å)	Unit cell volume (Å ³)	Phase	Lattice parameters (Å)	Unit cell volume (Å ³)
Ti ₂ Fe	11.320(3)	1450.5(11)	Ti ₂ FeH _x	12.064(5)	1756(2)

Now considering the phase fractions obtained by Rietveld refinement in Table 11, the theoretical composition for TiFe (1.86 wt.% H), FCC (H/M = 2, 3.7 wt.% H) and the stoichiometry calculated by unit cell volume increase for Ti_2FeH_x , the hydrogen intake contribution during activation of each phase can be calculated as follows: the 64% of TiFe would contribute 1.19 wt.% H, the 10% of Ti_2FeH_x between 0.2 – 0.3 wt.% H and the 26% of BCC – 0.96 wt.% H, for a total of 2.35 – 2.45 wt.% H. These results are not far

off from the 2.6 wt.% H measured during activation. The effect of the absorption of each phase is not seen in the activation curve, meaning that in Figure 27 the activation curve presents only one slope this points to the system acting as a single phase.

5.3.5 Comparison with previous works

Table 13 shows the activation results and the phase fraction of TiFe, Ti₂Fe and BCC of previous studies with different Ti_xFe_{2-x}-Zr_y-M_z compositions. All the studies showed that the addition of these doping elements would result in secondary phases that improve the activation kinetics. The work done on Ti_{1.2}Fe by Park et al. [44], demonstrated how a Ti-Fe alloy with TiFe, Ti₂Fe and BCC phases can activate at 25 °C under 4000 kPa of hydrogen pressure with an incubation time of 4 min reaching full saturation in 5.8 h. The alloy in their study was arc-melted and all handling of the samples was performed under argon atmosphere. As previously mentioned, the induction melted Ti_{1.2}Fe_{0.8} alloy despite presenting a TiFe, Ti₂Fe and BCC system cold rolling was required to promote activation under 2000 kPa of hydrogen pressure and room temperature with an incubation time of ~ 40 min and saturation time of 6 h.

As seen in Table 13 the hydrogen capacity and the time to achieve saturation varies a lot between the different studies. The hydrogen capacity is directly correlated to the phase fraction of each phase in the specific alloy. Regarding the saturation time/kinetics, it seems that the samples synthesized at lab scale tend to present faster kinetic than those produced by induction melting. However, the samples that required CR cannot be compared with those that were simply crushed since this processing technique has been shown to improve kinetics. However, between the studies that report the activation kinetics after CR5, the sample with finer microstructure (gas-atomized) presents faster kinetics. Determining the effect of each phase on the kinetics will require future work to focus solely on phase abundance.

Table 13. Summary of activation results and phase fractions of previous studies and current work.

Composition	Synthesis	Phases present	Capacity	Ref.
$Ti_{1.2}Fe$	Arc-melting Homogenization Annealing 1473 K – 10 h Crushed under Ar	TiFe (91.8 wt.%) Ti ₂ Fe (2.8 wt.%) Ti ₄ Fe _(BCC) (5.4 wt.%)	2.1 wt.% H 6 hours 4MPa @25 °C	[44]
TiFe+2w.t%Mn + 4 wt.% Zr	Induction melting No heat treatment Crushed under Ar	TiFe (70 wt.%) Ti ₂ Fe (28 wt.%) Ti (2 w.t%)	2 wt.% H ~12 h 2MPa @25 °C	[66]
TiFe+2w.t%Mn + 4 wt.% Zr	Atomized powder No heat treatment CR5 - Air	TiFe (76 wt.%) Ti ₂ Fe (4 wt.%) BCC (20 w.t%)	2.3 wt.% H ~2 h 2MPa @25 °C	[74]
$Ti_{1.2}Fe_{0.8}$ + 4 wt.% Zr	Arc-melt No heat treatment Crushed under Ar	TiFe (57 wt.%) Ti ₂ Fe (19 wt.%) BCC (24 wt.%)	2.1 wt.% H ~2 h 2MPa @25 °C	[73]
$Ti_{1.2}Fe_{0.8}$	Induction melting No heat treatment CR5 - Air	TiFe (67.8 wt.%) Ti ₂ Fe (9.4 wt.%) BCC (22.8 wt.%)	2.6 wt.% H ~6 h 2MPa @25 °C	Current work

As the comparison between studies that used arc melting and induction melting is unfair because the microstructure obtained by each synthesis method is different and it is known that microstructure influences activation kinetics. To see the effect of the microstructure, a small 3-gram sample was prepared by arc-melting of $Ti_{1.2}Fe_{0.8}$. Figure 30 shows the activation curve of the arc-melted sample. It activated without the need of any heat treatment or mechanical processing, reaching a capacity of 2 wt.% H in ~12 hours.

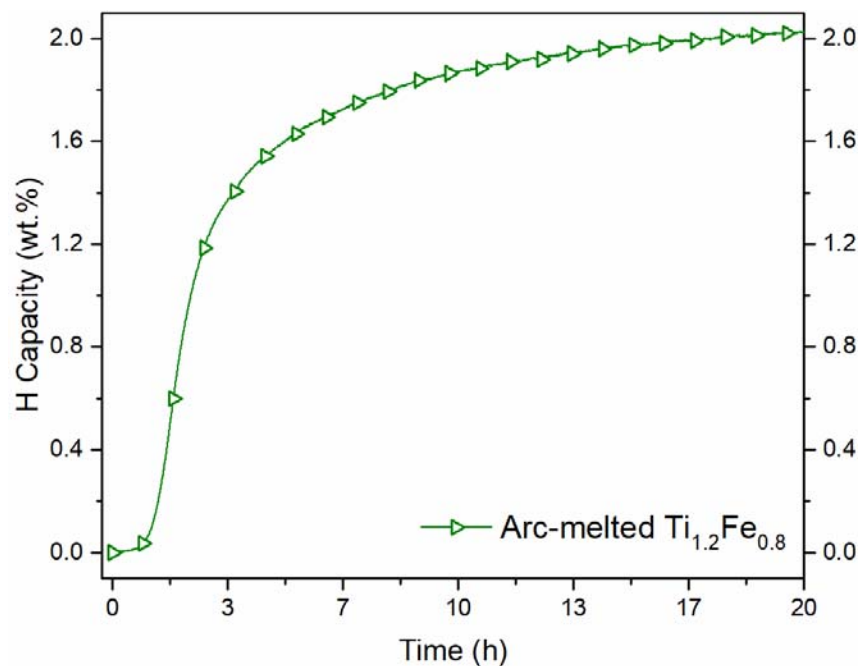


Figure 30. Activation curve of the arc-melted $\text{Ti}_{1.2}\text{Fe}_{0.8}$.

Figure 31 shows a side-to-side comparison of the microstructure obtained by induction melting (a) and arc-melting (b). It is clear from this figure that the arc-melted sample presents a much finer microstructure with a higher area abundance of the bright main phase, 77 % according to image analysis. The ability to activate without the need for cold rolling is attributed to the fine microstructure generated by arc-melting along with the secondary phases.

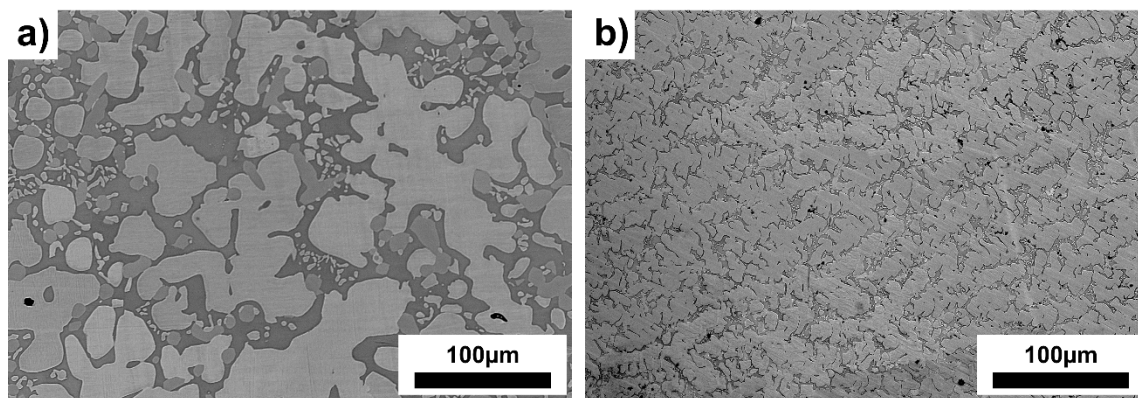


Figure 31. Backscattered electrons image of induction melted (a) and arc-melted (b) $\text{Ti}_{1.2}\text{Fe}_{0.8}$.

Figure 32 shows the XRD patterns of the arc-melted $Ti_{1.2}Fe_{0.8}$ alloy. The phases identified are TiFe, Ti_2Fe and BCC, matching those in the induction melted condition. The phase fraction obtained by Rietveld refinement are 80 wt.% TiFe, 4 wt.% Ti_2Fe and 16 wt.% BCC. This shows how lower percentages of the secondary phases can be enough to achieve activation under mild conditions if the microstructure is correct.

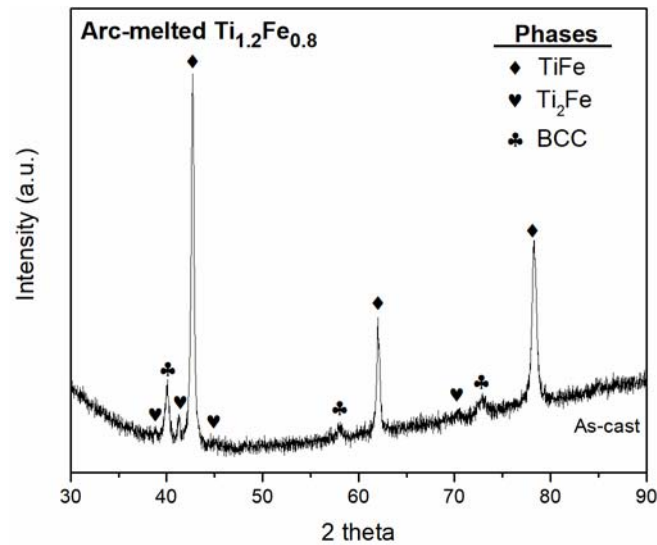


Figure 32. X-ray diffraction patterns of the induction melted $Ti_{1.2}Fe_{0.8}$.

5.3.6 Conclusions

- $Ti_{1.2}Fe_{0.8}$ forms secondary phases with the same crystal structure (Ti_2Fe and BCC) as those reported when alloying TiFe with Zr and Mn.
- Induction melted $Ti_{1.2}Fe_{0.8}$ alloy requires cold rolling to activate. It then reaches a capacity of 2.6 wt.% H with good kinetics.
- The microstructure obtained by arc-melting $Ti_{1.2}Fe_{0.8}$ provides better activation kinetics than that formed by induction melting.

CHAPTER VI

CONCLUSIONS

6.1 Conclusions

In this thesis the effect of microstructural, morphological and chemical variations on TiFe-based alloys for hydrogen storage were studied. The results showed how the microstructure obtained by different synthesis methods affects the activation kinetics of the alloys and how finer microstructure obtained by arc-melting have better activation kinetics than the same alloy synthesized by induction melting. Gas atomization was shown to be a novel synthesis route for the hydrogen storage field which yields TiFe-based alloys that can potentially be used in the hydrogen storage field. The effect of mechanical deformation by cold rolling has been shown to be a processing method that improves the activation kinetics of TiFe-based alloys. Additionally, it was shown that the same secondary phase structures (BCC – I-3m and Ti_2Fe – Fd-3m:2) formed when alloying TiFe with Zr and Mn can also be formed by the addition of overstoichiometric Ti.

6.2 Future work

6.2.1 Study of gas-atomized TiFe based alloys TiFe + 4wt.% Zr + 2 wt.% Mn and $Ti_{1.2}Fe$

In Chapter III it was seen that the atomized powder was unable to activate without cold rolling. However, the sample had been air-exposed for over 2 months when the experiments were performed. The study of freshly gas-atomized TiFe + 4 wt.% Zr + 2 wt.% Mn would allow to understand the effect of air exposure on the powder. Additionally, the study of gas-atomized overstoichiometric $Ti_{1.2}Fe$ would allow us to compare the different synthesis methods and better understand the benefits of gas-atomization. One way to perform these studies could be to partner with a company

that possess a gas-atomizer and would be interested in the development of metal-hydrides for hydrogen storage applications.

6.3 Perspective

The development of TiFe-based alloys mainly focuses on the improvement of activation kinetics. This focus is important since activation is the main obstacle facing the TiFe research however, the information on reversible capacity is lacking. Both the reversible capacity and the diffraction pattern after activation should be reported on when presenting a study on the activation behavior of TiFe-based alloys. For example, in our studies on overstoichiometric-Ti the secondary phases that improve the activation kinetics form stable hydrides that will ultimately not contribute to the reversible capacity. The possibility that only the TiFe phase contributes to the reversible capacity under mild conditions points to an ideal scenario where the goal is to obtain the highest wt.% of TiFe with just enough secondary phases abundance to improve the activation kinetics. This might not be the case for all secondary phases being formed but it is essential for researchers to report on it to better understand the alloy they studied.

RÉFÉRENCES BIBLIOGRAPHIQUES

- [1] D. L. Greene, J. M. Ogden, and Z. Lin, "Challenges in the designing, planning and deployment of hydrogen refueling infrastructure for fuel cell electric vehicles," *eTransportation*, vol. 6, 2020, doi: 10.1016/j.etrans.2020.100086.
- [2] L. E. R. Vega *et al.*, "Mechanical activation of TiFe for hydrogen storage by cold rolling under inert atmosphere," *International Journal of Hydrogen Energy*, vol. 43, no. 5, pp. 2913-2918, 2018.
- [3] J. Bellosta von Colbe *et al.*, "Application of hydrides in hydrogen storage and compression: Achievements, outlook and perspectives," *International Journal of Hydrogen Energy*, vol. 44, no. 15, pp. 7780-7808, 2019.
- [4] IEA, "The Future of Hydrogen," Paris, 2019.
- [5] J. O. Abe, A. P. I. Popoola, E. Ajenifuja, and O. M. Popoola, "Hydrogen energy, economy and storage: Review and recommendation," *International Journal of Hydrogen Energy*, vol. 44, no. 29, pp. 15072-15086, 2019, doi: 10.1016/j.ijhydene.2019.04.068.
- [6] L. Schlapbach, "Hydrogen-fuelled vehicles," *Nature*, vol. 460, pp. 809-811, 2009.
- [7] B. Sakintuna, F. Lamaridarkrim, and M. Hirscher, "Metal hydride materials for solid hydrogen storage: A review☆," *International Journal of Hydrogen Energy*, vol. 32, no. 9, pp. 1121-1140, 2007.
- [8] Z. Chen, Z. Ma, J. Zheng, X. Li, E. Akiba, and H.-W. Li, "Perspectives and challenges of hydrogen storage in solid-state hydrides," *Chinese Journal of Chemical Engineering*, 2020, doi: 10.1016/j.cjche.2020.08.024.
- [9] P. A. Chen, E.; Orimo, S.; Züttel, A.; Schlapbach, L., "Hydrogen Storage by Reversible Metal Hydride Formation," in *Hydrogen Science and Engineering: Materials, Processes, Systems and Technology*, D. E. Stolte, B. Ed., First ed.: Wiley-VCH Verlag GmbH & Co., 2016.
- [10] J. Huot, "Metal Hydrides," in *Handbook of Hydrogen Storage*, M. Hirscher Ed.: WILEY-VCH Verlag GmbH & Co. KGaA, 2010.
- [11] B. Cantor, "High-Entropy Alloys," in *Encyclopedia of Materials: Science and Technology* 2ed, 2011, pp. 1-3.
- [12] Y. Z. A. Faghri, *Transport Phenomena in Multiphase Systems*. Elsevier Inc., 2006.

- [13] L. Wang, K. Young, J. Nei, D. Pawlik, and K. Y. S. Ng, "Hydrogenation of AB₅ and AB₂ metal hydride alloys studied by in situ X-ray diffraction," *Journal of Alloys and Compounds*, vol. 616, pp. 300-305, 2014, doi: 10.1016/j.jallcom.2014.07.125.
- [14] X.-Q. Chen, W. Wolf, R. Podloucky, and P. Rogl, "Ab initio study of ground-state properties of the Laves phase compounds TiCr₂, ZrCr₂, and HfCr₂," *Physical Review B*, vol. 71, no. 17, 2005, doi: 10.1103/PhysRevB.71.174101.
- [15] G. Mazzolai *et al.*, "Hydrogen-storage capacities and H diffusion in bcc TiVCr alloys," *Journal of Alloys and Compounds*, vol. 466, no. 1-2, pp. 133-139, 2008, doi: 10.1016/j.jallcom.2007.11.040.
- [16] N. B. E. Dematteis, F. Cuevas, M. Latroche, and M. Baricco, "Substitutional effects in TiFe for hydrogen storage: a comprehensive review."
- [17] J. J. Reilly and R. H. Wiswall, "Formation and properties of iron titanium hydride," *Inorganic Chemistry*, vol. 13, no. 1, pp. 218-222, 1974/01/01 1974.
- [18] G. K. Sujana, Z. Pan, H. Li, D. Liang, and N. Alam, "An overview on TiFe intermetallic for solid-state hydrogen storage: microstructure, hydrogenation and fabrication processes," *Critical Reviews in Solid State and Materials Sciences*, pp. 1-18, 2019.
- [19] T. Schober and D. G. Westlake, "The activation of FeTi for hydrogen storage: A different view*," *Scripta Metallurgica*, vol. 15, pp. 913-918, 1981.
- [20] L. Schlapbach and T. Riesterer, "The activation of FeTi for hydrogen absorption," *Appl. Phys. A*, vol. 32, p. 169-182, 1983.
- [21] J. Manna, B. Tougas, and J. Huot, "Mechanical activation of air exposed TiFe + 4 wt% Zr alloy for hydrogenation by cold rolling and ball milling," *International Journal of Hydrogen Energy*, vol. 43, no. 45, pp. 20795-20800, 2018.
- [22] H. Emami, K. Edalati, J. Matsuda, E. Akiba, and Z. Horita, "Hydrogen storage performance of TiFe after processing by ball milling," *Acta Materialia*, vol. 88, pp. 190-195, 2015.
- [23] R. B. Falcão *et al.*, "An alternative route to produce easily activated nanocrystalline TiFe powder," *International Journal of Hydrogen Energy*, vol. 43, no. 33, pp. 16107-16116, 2018.
- [24] P. Lv, M. N. Guzik, S. Sartori, and J. Huot, "Effect of ball milling and cryomilling on the microstructure and first hydrogenation properties of TiFe+4 wt.% Zr alloy," *Journal of Materials Research and Technology*, vol. 8, no. 2, pp. 1828-1834, 2019.
- [25] C. Gosselin and J. Huot, "First Hydrogenation Enhancement in TiFe Alloys for Hydrogen Storage Doped with Yttrium," *Metals*, vol. 9, no. 2, 2019.

- [26] S. Kumar, G. P. Tiwari, S. Sonak, U. Jain, and N. Krishnamurthy, "High performance FeTi – 3.1 mass % V alloy for on board hydrogen storage solution," *Energy*, vol. 75, pp. 520-524, 2014.
- [27] W. Ali *et al.*, "Hydrogenation properties of Ti-Fe-Mn alloy with Cu and Y as additives," *International Journal of Hydrogen Energy*, vol. 42, no. 4, pp. 2229-2238, 2017.
- [28] H. Leng *et al.*, "Effect of cobalt on the microstructure and hydrogen sorption performances of TiFe_{0.8}Mn_{0.2} alloy," *International Journal of Hydrogen Energy*, vol. 45, no. 38, pp. 19553-19560, 2020.
- [29] H. Leng, Z. Yu, J. Yin, Q. Li, Z. Wu, and K.-C. Chou, "Effects of Ce on the hydrogen storage properties of TiFe 0.9 Mn 0.1 alloy," *International Journal of Hydrogen Energy*, vol. 42, no. 37, pp. 23731-23736, 2017.
- [30] T. Yang *et al.*, "Effect of chromium, manganese and yttrium on microstructure and hydrogen storage properties of TiFe-based alloy," *International Journal of Hydrogen Energy*, vol. 45, no. 21, pp. 12071-12081, 2020.
- [31] C. Gosselin and J. Huot, "Hydrogenation Properties of TiFe Doped with Zirconium," (in eng), *Materials (Basel)*, vol. 8, no. 11, pp. 7864-7872, Nov 20 2015.
- [32] P. Lv and J. Huot, "Hydrogenation improvement of TiFe by adding ZrMn₂," *Energy*, vol. 138, pp. 375-382, 2017/11/01/ 2017.
- [33] P. Jain, C. Gosselin, and J. Huot, "Effect of Zr, Ni and Zr 7 Ni 10 alloy on hydrogen storage characteristics of TiFe alloy," *International Journal of Hydrogen Energy*, vol. 40, no. 47, pp. 16921-16927, 2015.
- [34] P. Jain, C. Gosselin, N. Skryabina, D. Fruchart, and J. Huot, "Hydrogenation properties of TiFe with Zr₇Ni₁₀ alloy as additive," *Journal of Alloys and Compounds*, vol. 636, pp. 375-380, 2015.
- [35] P. Lv, Z. Liu, and V. Dixit, "Improved hydrogen storage properties of TiFe alloy by doping (Zr+2V) additive and using mechanical deformation," *International Journal of Hydrogen Energy*, vol. 44, no. 51, pp. 27843-27852, 2019.
- [36] C. Gosselin, D. Santos, and J. Huot, "First hydrogenation enhancement in TiFe alloys for hydrogen storage," *Journal of Physics D: Applied Physics*, vol. 50, no. 37, 2017, doi: 10.1088/1361-6463/aa7d6a.
- [37] M. Faisal, J.-Y. Suh, and Y.-S. Lee, "Understanding first cycle hydrogenation properties of Ti–Fe–Zr ternary alloys," *International Journal of Hydrogen Energy*, vol. 46, no. 5, pp. 4241-4251, 2021, doi: 10.1016/j.ijhydene.2020.11.025.

- [38] L. Zeng, G. Xu, L. Liu, W. Bai, and L. Zhang, "Experimental investigation of phase equilibria in the Ti-Fe-Zr system," *Calphad*, vol. 61, pp. 20-32, 2018, doi: 10.1016/j.calphad.2018.02.005.
- [39] Z. Surowiec, M. Wiertel, A. I. Beskrovnyi, J. Sarzy ski, and J. J. Milczarek, "Investigations of microscopic magnetic properties of the pseudo-binary system (Zr_{1-x}Ti_x)Fe₂," *Journal of Physics: Condensed Matter*, vol. 15, no. 37, pp. 6403-6414, 2003, doi: 10.1088/0953-8984/15/37/008.
- [40] T. Velikanova and K. Korniyenko, "Iron – Titanium – Zirconium," in *Iron Systems, Part 5*, (Landolt-Börnstein - Group IV Physical Chemistry, 2009, ch. Chapter 34, pp. 702-720.
- [41] G. Zhou, D. Zeng, and Z. Liu, "Phase equilibria in the Fe–Ti–Zr system at 1023K," *Journal of Alloys and Compounds*, vol. 490, no. 1-2, pp. 463-467, 2010, doi: 10.1016/j.jallcom.2009.10.046.
- [42] G.-j. Zhou, S. Jin, L.-b. Liu, H.-s. Liu, and Z.-p. Jin, "Determination of isothermal section of Fe-Ti-Zr ternary system at 1173 K," *Transactions of Nonferrous Metals Society of China*, vol. 17, no. 5, pp. 963-966, 2007, doi: 10.1016/s1003-6326(07)60208-8.
- [43] V. N. Fokin, E. E. Fokina, I. I. Korobov, and B. P. Tarasov, "Phase transformations in the systems Ti₂Fe–H₂ and Ti₂Fe–NH₃," *Russian Journal of Inorganic Chemistry*, vol. 61, no. 7, pp. 891-895, 2016, doi: 10.1134/s0036023616070044.
- [44] K. B. Park *et al.*, "Characterization of microstructure and surface oxide of Ti_{1.2}Fe hydrogen storage alloy," *International Journal of Hydrogen Energy*, vol. 46, no. 24, pp. 13082-13087, 2021, doi: 10.1016/j.ijhydene.2021.01.105.
- [45] V. P. Mordovina, A. V. Kasimtsev, V. P. Alekhin, and V. V. Zhigunov, "Industrial technologies for production of LaNi₅-based hydride materials," *Hydrogen Materials Science and Chemistry of Carbon Nanomaterials*, pp. 407-414, 2007.
- [46] A. K. Patel, B. Tougas, P. Sharma, and J. Huot, "Effect of cooling rate on the microstructure and hydrogen storage properties of TiFe with 4 wt% Zr as an additive," *Journal of Materials Research and Technology*, 2019/09/26/ 2019.
- [47] M. L. Anderson and I. E. Anderson, "Gas atomization of metal hydrides for Ni–MH battery applications," *Journal of Alloys and Compounds*, vol. 313, no. 1, pp. 47-52, 2000/12/15/ 2000.
- [48] S. R. Chung and T. P. Perng, "Effect of particle size on hydrogenation properties of a gas-atomized AB₅-type alloy," *Journal of Alloys and Compounds*, vol. 353, no. 1-2, pp. 289-294, 2003.
- [49] J. Ting *et al.*, "Gas atomization processing of designed dual-phase intermetallic hydrogen storage alloys," *Materials Science and Engineering: A*, vol. 329-331, pp. 372-376, 2002/06/01/ 2002.

- [50] H. Yoshinaga, Y. Arami, O. Kajita, and T. Sakai, "Highly densified-MH electrode using flaky nickel powder and gas-atomized hydrogen storage alloy powder," *Journal of Alloys and Compounds*, vol. 330-332, pp. 846-850, 2002/01/17/ 2002.
- [51] J.-H. Kim, H. Lee, K.-T. Hwang, and J.-S. Han, "Hydriding behavior in Zr-based AB₂ alloy by gas atomization process," *International Journal of Hydrogen Energy*, vol. 34, no. 23, pp. 9424-9430, 2009.
- [52] H. K. a. A. Lawley, *Powder metallurgy processing. New techniques and analyses*. New York, N.Y: Academic Press, 1978.
- [53] B. Z. a. E. J. Lavernia, *Handbook of Atomization and Sprays*. Springer, 2011.
- [54] N. Grant, "Rapid Solidification of Metallic Particulates," *JOM*, vol. 35, no. 1, pp. 20-27, 1983/01/01 1983, doi: 10.1007/BF03338180.
- [55] M. R. a. D. Conn, "Method for Producing Powder by Gas Atomization," Patent Appl. 359,978, 1991.
- [56] B. Zheng, Y. Lin, Y. Zhou, and E. J. Lavernia, "Gas Atomization of Amorphous Aluminum Powder: Part II. Experimental Investigation," *Metallurgical and Materials Transactions B*, vol. 40, no. 6, p. 995, 2009/08/26 2009, doi: 10.1007/s11663-009-9277-4.
- [57] V. B. Oliveira *et al.*, "Hydrogen Absorption/Desorption Behavior of a Cold-Rolled TiFe Intermetallic Compound," *Materials Research*, vol. 24, no. 6, 2021, doi: 10.1590/1980-5373-mr-2021-0204.
- [58] R. A. Silva *et al.*, "Room temperature hydrogen absorption by Mg and Mg TiFe nanocomposites processed by high-energy ball milling," *International Journal of Hydrogen Energy*, vol. 43, no. 27, pp. 12251-12259, 2018.
- [59] M. Kumar *et al.*, "Ball milling as a mechanochemical technology for fabrication of novel biochar nanomaterials," (in eng), *Bioresource technology*, Review vol. 312, p. 123613, Sep 2020, doi: 10.1016/j.biortech.2020.123613.
- [60] J. H. S. Flegler, and K. Klomparens *Scanning and Transmission Electron Microscopy: An Introduction* Oxford University Press, 1993.
- [61] M. I. Szyrkowska, *Microscopy Techniques | Scanning Electron Microscopy*, Second Edition ed. 2005, pp. 134-143.
- [62] D. Broom, *Hydrogen Storage Materials The Characterisation of Their Storage Properties* 1ed. Springer, 2011.
- [63] D. Broom, "Hydrogen Sorption Measurements on Potential Storage Materials.," *JRC OPOCE*, 2008, doi: 10.2790/86100.
- [64] C. C. B. Dutrow. "X-ray Powder Diffraction (XRD)." <https://serc.carleton.edu/18400> (accessed).

- [65] P. P. Ewald, "The Principles of X-ray Diffraction," in *Fifty Years of X-Ray Diffraction: Dedicated to the International Union of Crystallography on the Occasion of the Commemoration Meeting in Munich July 1962*, P. P. Ewald Ed. Boston, MA: Springer US, 1962, pp. 82-101.
- [66] A. K. Patel, A. Duguay, B. Tougas, C. Schade, P. Sharma, and J. Huot, "Microstructure and first hydrogenation properties of TiFe alloy with Zr and Mn as additives," *International Journal of Hydrogen Energy*, 2019.
- [67] A. K. Patel, A. Duguay, B. Tougas, C. Schade, P. Sharma, and J. Huot, "Microstructure and first hydrogenation properties of TiFe alloy with Zr and Mn as additives," *International Journal of Hydrogen Energy*, vol. 45, no. 1, pp. 787-797, 2020, doi: 10.1016/j.ijhydene.2019.10.239.
- [68] J. Manna, B. Tougas, and J. Huot, "First hydrogenation kinetics of Zr and Mn doped TiFe alloy after air exposure and reactivation by mechanical treatment," *International Journal of Hydrogen Energy*, 2020.
- [69] P. Lv and Z. Liu, "Effect of high zirconium content on hydrogenation properties and anti-poisoning ability of air-exposed TiFe alloy," *Journal of Materials Research and Technology*, vol. 8, no. 6, pp. 5972-5983, 2019, doi: 10.1016/j.jmrt.2019.09.072.
- [70] H. Buchner, Gutjahr, M. A., Beccu, K. D., and Saeufferer, H., "Hydrogen in intermetallic phases: the system titanium--nickel--hydrogen. Wasserstoff in intermetallischen phasen am beispiel des systems titan-nickel-wasserstoff.," Germany, 1972 1972.
- [71] A. K. Patel, P. Sharma, and J. Huot, "Effect of annealing on microstructure and hydrogenation properties of TiFe + X wt% Zr (X = 4, 8)," *International Journal of Hydrogen Energy*, vol. 43, no. 12, pp. 6238-6243, 2018, doi: 10.1016/j.ijhydene.2018.02.029.
- [72] D. M. D. Erika Michela Dematteis, Giovanni Capurso, Julian Jepsen, Fermin Cuevas, Michel Latroche,, "Fundamental hydrogen storage properties of TiFe-alloy with partial substitution of Fe by Ti and Mn," *Journal of Alloys and Compounds*, vol. 874, 2021.
- [73] E. Ulate-Kolitsky, B. Tougas, and J. Huot, "Hydrogenation of Ti_xFe_{2-x} -based alloys with overstoichiometric Ti ratio ($x = 1.1, 1.15$ and 1.2)," *International Journal of Hydrogen Energy*, vol. 46, no. 77, pp. 38363-38369, 2021, doi: 10.1016/j.ijhydene.2021.09.077.
- [74] E. Ulate-Kolitsky, B. Tougas, B. Neumann, C. Schade, and J. Huot, "First hydrogenation of mechanically processed TiFe-based alloy synthesized by gas atomization," *International Journal of Hydrogen Energy*, vol. 46, no. 10, pp. 7381-7389, 2021, doi: 10.1016/j.ijhydene.2020.11.237.

SECTION B

APPENDICES

ARTICLES

- [1] E. Ulate-Kolitsky, B. Neumann, C. Schade, J. Huot, First hydrogenation of mechanically processed TiFe-based alloy synthesized by gas atomization, *Int. J. Hydrogen Energy* 46 10 (2021) 7381-7389, <https://doi.org/10.1016/j.ijhydene.2020.11.237>.
- [2] Ulate-Kolitsky E, B. Tougas, J. Huot, Hydrogenation of Ti_xFe_{2-x} -based alloys with overstoichiometric Ti ratio ($x = 1.1, 1.15$ and 1.2), *International Journal of Hydrogen Energy*, <https://doi.org/10.1016/j.ijhydene.2021.09.077>
- [3] Ulate-Kolitsky E, B. Tougas, J. Huot, First hydrogenation of TiFe + 20 wt. % Ti ($Ti_{1.2}Fe_{0.8}$), Submitted to the *International Journal of Hydrogen Energy*.

Article 1

First hydrogenation of mechanically processed TiFe-based alloy synthesized by gas atomization

Ulate-Kolitsky E.¹, Tougas B.², Neumann B.³, Schade C.⁴, Huot J.^{1*}

¹ Institut de Recherche sur l'Hydrogène, Université Du Québec à Trois-Rivières, 3351 des Forges, Trois-Rivières, Québec, G9A 5H7, Canada

² Centre de Métallurgie du Québec, 3095 Rue Westinghouse Parc Industriel Des Hautes-Forges, Trois-Rivières, Québec, G9A 5E1, Canada

³ GKN Sinter Metals Engineering GmbH, Germany

⁴ GKN Hoeganaes Innovation Center & Advanced Materials - New Jersey, USA

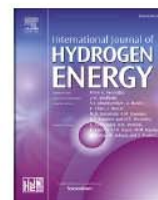
Abstract

The study shows the first hydrogenation (activation) of both a cold-rolled and a ball milled TiFe-based alloy synthesized by gas-atomization. Gas atomization's primary effect was on the microstructure: a TiFe-matrix surrounded by a finely distributed secondary phases. The as-received sample did not activate, probably due to the long air exposure before hydrogenation tests. Cold rolling for one and five passes (CR1-CR5) was tested as a way to reactivate the alloy. After CR1 and CR5 activation occurs with fast kinetics, reaching a capacity of 2.1-%wt. Ball milling also resulted in activation but the kinetics were sluggish, requiring more than 60 hours to reach full capacity. Based on the results shown and on the comparison between the work done on the same composition synthesized by induction casting it can be concluded that gas-atomization is a good candidate for the production of TiFe-based alloys that present good kinetics and capacity after air exposure.

Keywords: Microstructure; atomization; activation kinetics; cold-rolling; ball-milling.

Available online at www.sciencedirect.com

ScienceDirect

journal homepage: www.elsevier.com/locate/ijhe

First hydrogenation of mechanically processed TiFe-based alloy synthesized by gas atomization



E. Ulate-Kolitsky^{a,*}, B. Tougas^b, B. Neumann^c, C. Schade^d, J. Huot^a

^a Institut de Recherche sur L'hydrogène, Université Du Québec à Trois-Rivières, 3351 des Forges, Trois-Rivières, Québec, G9A 5H7, Canada

^b Centre de Métallurgie Du Québec, 3095 Rue Westinghouse Parc Industriel Des Hautes-Forges, Trois-Rivières, Québec, G9A 5E1, Canada

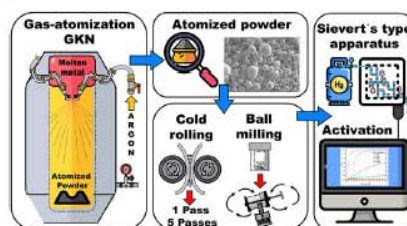
^c GKN Sinter Metals Engineering GmbH, Germany

^d GKN Hoeganaes Innovation Center & Advanced Materials - New Jersey, USA

HIGHLIGHTS

- TiFe-based alloy was synthesized by gas-atomization.
- The sample was air-exposed for 2 months before testing began.
- The alloy presented fast kinetics after cold rolling under air.

GRAPHICAL ABSTRACT



ARTICLE INFO

Article history:

Received 4 September 2020

Received in revised form

23 November 2020

Accepted 26 November 2020

Available online 17 December 2020

Keywords:

Microstructure

Atomization

Activation kinetics

Cold-rolling

Ball-milling

ABSTRACT

The study shows the first hydrogenation (activation) of both a cold-rolled and a ball milled TiFe-based alloy synthesized by gas-atomization. Gas atomization's primary effect was on the microstructure: a TiFe-matrix surrounded by finely distributed secondary phases. The as-received sample did not activate, probably due to the long air exposure before hydrogenation tests. Cold rolling for one and five passes (CR1-CR5) was tested as a way to reactivate the alloy. After CR1 and CR5 activation occurs with fast kinetics, reaching a capacity of 2.1-%wt. Ball milling also resulted in activation but the kinetics were sluggish, requiring more than 60 h to reach full capacity. Based on the results shown and on the comparison between the work done on the same composition synthesized by induction casting it can be concluded that gas-atomization is a good candidate for the production of TiFe-based alloys that present good kinetics and capacity after air exposure.

© 2020 Hydrogen Energy Publications LLC. Published by Elsevier Ltd. All rights reserved.

* Corresponding author.

E-mail address: elena@irh.ca (E. Ulate-Kolitsky).

<https://doi.org/10.1016/j.ijhydene.2020.11.237>

0360-3199/© 2020 Hydrogen Energy Publications LLC. Published by Elsevier Ltd. All rights reserved.

Introduction

Hydrogen has the potential to become a versatile and clean fuel for stationary, portable and mobile applications. For practical applications, storing hydrogen should be safe and economical. Beside the conventional methods of high pressure and liquid, the utilization of metal hydrides is an attractive and safe method to store hydrogen in a compact way. However, to be used in practical applications, metal hydrides have to show acceptable hydrogenation and dehydrogenation kinetics, good hydrogen capacity, cyclability and low cost [1]. Several alloys have been proposed as possible candidates e.g., Mg-alloys [2–4], LaNi₅ [5–7], complex hydrides [8,9], High Entropy Alloys [10,11]. The alloy TiFe is a well-known metal hydride that has a hydrogen absorption capacity of 1.86 wt% at low pressure at room temperature [12,13]. However, this alloy usually requires a heat treatment to achieve the first hydrogenation (activation) [12]. This activation process implies cycling between high temperature and room temperature under high hydrogen pressure, a process that is time consuming and increases the hydride cost.

Activation of TiFe has been improved by different approaches like mechanical processing such as ball milling, cold rolling, high-pressure torsion [14–18] and/or addition of transition metals [19–24]. It has been recently shown that adding zirconium or zirconium-based alloys to TiFe greatly enhanced the activation kinetics [25–29]. Patel et al. have reported fast activation and high capacity (2 wt%) for the composition TiFe + 2 wt% Mn + 4 wt% Zr [30].

Besides activation, the production cost of a metal hydride in an industrial scale is crucial for commercialization. The typical process to obtain metal hydride alloys is by fusion (arc-melting, induction melting, electron beam). Other methods such as electrochemical reduction, mechanical alloying, combustion synthesis, etc. are also used [6,13]. The determination or development of what could be a one-step process that results in a powdered alloy with an ideal microstructure is a task that has not been achieved. Most of the prior mentioned synthesis techniques require processing or heat treatment to achieve good hydrogenation properties. Gas atomization is a synthesis process that can directly produce metallic powders at an industrial scale. It will be interesting to see the effect of this synthesis method on the hydrogen storage of TiFe-based alloys to determine if it is a viable option.

The microstructure of an alloy will greatly affect its hydrogenation properties. Pattel et al. studied the effect of the cooling rate on the microstructure of TiFe + 4 wt% Zr by casting in a step mold with different thicknesses. Higher cooling rates resulted in finer distribution of the secondary phase that proved to be beneficial to the activation kinetics [31]. The study showed a linear trend between the change of the microstructure and the cooling rate.

Typical cooling rates for gas atomization are between 10⁴ and 10⁶ K/s [32,33]. In regards to the previous work by Pattel et al. atomization cooling rates are order of magnitude higher. This may have an impact on the alloy's microstructure and thus on the hydrogen storage properties. To our knowledge, there have been no previous investigations on the

hydrogenation behavior of atomized TiFe-based alloys. There is some work done on metal hydride powders produced by gas atomization for hydrogen storage and for nickel-metal hydride batteries. Some focus on electrochemical cycling and the discharge capacity: AB₅-type alloys (LaNi_{4.75}Sr_{0.25}, MmNi_{3.6}Co_{0.56}Mn_{0.56}Al_{0.28}, Zr-based) [34–37], while others did report the gas-phase hydrogenation (MmNi_{3.6}Co_{0.56}Mn_{0.56}Al_{0.28} and Zr-based AB₂) [35,38]. Kim et al. [38], showed that, for the AB₂ alloy Zr_{0.55}Ti_{0.45}V_{0.54}Mn_{0.24}Ni_{0.88}Co_{0.16}Cr_{0.16} produced by gas atomization, the particles smaller than 50 μm present a highly sloped plateau and a larger hysteresis loop than particles larger than 50 μm as well as a decrease of the storage capacity. This was explained by a partially amorphous phase which inhibited the hydride–dehydrate reaction between the gas–solid. Chung et al. [35] found that, particles smaller than 10 μm showed slower kinetics and lower capacity than larger particles of AB₅ type alloy. However, no amorphous phase was found.

In this paper, we report the effect of cold rolling and ball milling on hydrogen storage behavior of TiFe + 2 wt% Mn + 4 wt% Zr alloy synthesized by gas atomization. This composition was chosen due to its good activation kinetics and high hydrogen capacity [30]. Comparison with the same composition obtained by a traditional casting method is also presented.

Material and methods

Gas atomization was done by GKN Hoeganaes Innovation Center & Advanced Materials, using industrial grade Fe (ASTM 1005), Ti (ASTM B265 grade 1), Zr 702 (99.2%) and electrolytic manganese Mn (99.7%). The atomization was done under pure argon with a VIGA-type furnace with a free fall atomization ring configuration. The resulting powder alloy was packed in air.

The morphology and microstructure of the powder were analyzed using a scanning electron microscope (Hitachi SU3500) equipped with an EDX - Energy Dispersive X-ray spectrometer (Oxford Instrument Model X-Max^{NSO}). Image analysis was performed using ImageJ software.

Activation kinetics was measured using a homemade Sieverts' type apparatus, at room temperature (RT) and under 20 bars of hydrogen. The samples were studied under three conditions, i) As-received, ii) Cold Rolled (CR) and iii) Ball milled (BM). Cold Rolling was done in air using a modified version of Durston DRM 130 model where the powder samples could be cold rolled vertically between stainless steel plates to avoid contamination of the powder by the rollers. Samples were cold rolled for 1 or 5 passes (CR1, CR5). Ball milling was done for 5, 10 and 30 min (BM5, BM10, BM30) on a SPEX 8000 M (1725 RPM) apparatus using a ball to sample mass ratio of 10:1. Ball milled powder was processed and handled under argon.

The crystal structure of the samples was analyzed by X-ray Diffraction (XRD) using a Bruker D8 powder diffractometer with CuK α radiation. Crystal structure parameters were evaluated with the Rietveld refinement method using TOPAS software (V6.0).

The rate-limiting step was determined using several kinetic models' equations to evaluate the best fit for the CR1 and

CR5 samples. The models used were Chemisorption, JMA2D, JMA3D, CV2D, CV3D, GB2D and GB3D.

Results and discussion

Fig. 1a and b shows the microstructure of the as-atomized particles. We see that the internal structure of the particle consists of a matrix (grey phase), a darker grey secondary phase and a bright phase. Fig. 2 shows a higher magnification image of the regions analyzed by EDX. The chemical composition of the bulk and each specific region was measured by EDX and the results are shown in Table 1.

The bulk measurement shows that the alloy is actually titanium-rich and the composition could be written as $Ti_{1.11}Fe_{0.80}Mn_{0.04}Zr_{0.05}$. This is different from the nominal composition ($Ti_{0.96}Fe_{0.96}Mn_{0.04}Zr_{0.05}$) but it falls within the composition range for TiFe phase according to the Ti–Fe phase diagram [39]. The Mn and Zr abundances match quite closely the nominal composition.

The matrix (Spectrum 1) is essentially TiFe alloy with slight amount of Mn and very small proportion of Zr. The secondary phase (Spectrum 2) is Ti-rich and has higher content of Mn and Zr than the matrix. In fact, assuming that Mn and Zr are on the same site as Fe, this phase has a stoichiometry close to $Ti_2(Fe,Mn,Zr)$. Zirconium is mainly located in the bright regions (Spectrum 3). The phase fractions were calculated by image processing, the matrix accounts for 76% of the alloy, with the secondary and bright phases are respectively 20% and 4% of the total surface.

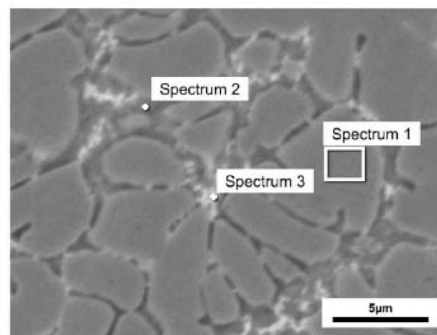


Fig. 2 – Backscattered electrons image of atomized particle cross section. Spectrum 1: matrix; spectrum 2: dark grey phase; spectrum 3: bright precipitate.

Fig. 1c and d shows the induction melted TiFe +2 wt% Mn + 4 wt% Zr alloy previously reported by Patel et al. [30]. A clear difference is notable with the atomized alloy. The microstructure is much finer for the atomized powder. The cast alloy presents a eutectic microstructure within the interphase region. The eutectic reaction is between the matrix (TiFe) and the bright phase (Zr-rich 20 at%). This indicates that atomization is a way to oversaturate the Zr in the interphase by avoiding a eutectic reaction thanks to rapid solidification.

The as-atomized powder was subjected to 20 bars of hydrogen at room temperature for a period of at least 24 h. No hydrogen uptake was registered. This is thought to be caused by the long-term air exposure undergone by the

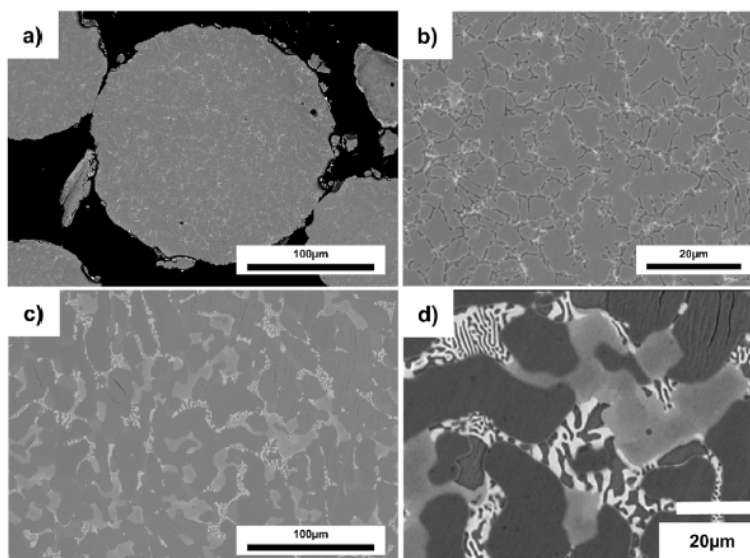


Fig. 1 – Backscattered electrons image of an atomized TiFe +2 wt% Mn + 4 wt% Zr particle cross section. a) low magnification; b) high magnification. Backscattered electron image induction melted TiFe +2 wt% Mn + 4 wt% Zr c) low magnification; d) high magnification [30].

Table 1 – Chemical composition, in at.%, of the gas atomized EDX analysis (uncertainty is ± 1 for all values).

	Nominal composition	Bulk composition	Spectrum 1	Spectrum 2	Spectrum 3
Ti	47.9	55.6	51.0	71.2	58.4
Fe	47.9	39.8	46.9	21.5	23.2
Mn	1.9	2.2	1.7	2.2	2.4
Zr	2.3	2.4	0.4	5.1	16.0

sample. After the powder was synthesized, it was packed in air and remained under this condition for 2 months before the activation attempt was performed. It is known that, after air exposure, TiFe is resistant to hydrogenation [14,40–42].

It has been shown in other metal hydrides systems that cold rolling and ball milling could improve the activation kinetics or regenerate powders that were exposed to the air and were inert to hydrogen [14,15,17]. It has also been shown that the milling time should be kept minimal [18]. Therefore, in the present study we performed 1 and 5 cold rolling passes in air while the ball milling was performed for 5, 10 and 30 min. The micrographs of the processed powder using these two techniques can be seen in Fig. 3.

Fig. 3a shows the as-received atomized powder. The particles are mainly spherical, some present small satellites, where two spheres are joined. The particle size distribution was obtained by sieving 100 g of the powder and the mean diameter, D_{50} , was determined to be 105 μm .

Fig. 3b and c shows respectively the CR1 and CR5 samples. The CR1 image shows that most of the big spheres were cracked while there is some consolidation of the smaller particles forming a porous plate sample. For CR5 the cracking of the big sphere is less apparent, and most particles are compressed together in the same way to CR1 formed a porous plate structure.

Fig. 3d, e and 3f show the ball milled samples for 5, 10 and 30 min respectively. Ball milling is a high energy process and

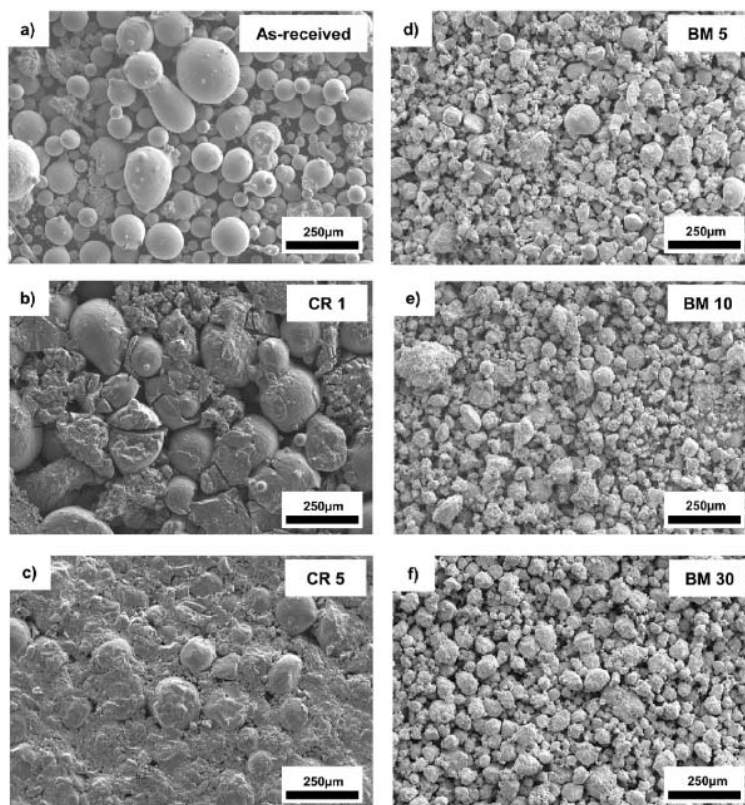


Fig. 3 – Morphology of atomized powder by processing: a) as atomized, b) cold rolled 1 pass (CR1), c) cold rolled 5 passes (CR5), d) ball milled 5 min, e) ball milled 10 min and f) ball milled 30 min.

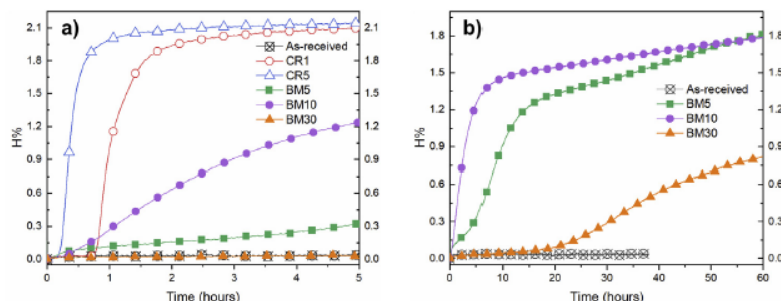


Fig. 4 – a) Activation under 20 bars of hydrogen pressure and at RT for all samples, b) long-term activation for BM5, BM10 and BM30.

after 5 min of milling the spheres are broken up into fine irregular powder particles. Further increase of BM time results in a decrease of particle size and the formation of agglomerations of small particles.

Fig. 4a shows the activation curves of all the samples. The as-received sample did not activate even after more than 24 h. The fastest activation and highest capacity were achieved by the CR5 sample. Both the CR1 and CR5 present high kinetics, reaching saturation in 3 and 2 h respectively and no loss of capacity. All ball milled samples presented very slow kinetics. BM5 and BM10 reached a capacity of ~1.8 wt% but were still slowly absorbing when the experiment was stopped after 60 h (see Fig. 4b). BM30 kinetics suffered a severe decrease of kinetics reaching only ~0.85 wt% after 60 h of hydrogen exposure. Peng et al. [18] correlated the BM processing time with a decrease of crystallite size and a decrease of capacity. They also discuss the formation of grain boundaries that act as diffusion points for the hydrogen but ultimately do not store hydrogen. Emami et al. [16] described the highly strained grain boundaries as trapping sites for the hydrogen. The CR process also induces a decrease in the crystallite size and an increase of the microstrain. However, the effect is mild compared to the highly energetic deformation caused by BM.

Fig. 5a shows the XRD patterns of the powder for the conditions shown in Fig. 3: As-atomized, CR1, CR5, BM5, BM10 and BM30. Fig. 5b shows a side to side comparison between CR5 and CR5 after hydrogenation and desorption. In the patterns in Fig. 5a the following phases were identified: TiFe, Ti₂Fe and a BCC phase. By correlating the phases identified by SEM and EDX, it can be assumed that the matrix and dark grey phase are respectively TiFe and Ti₂Fe. The presence of the BCC phase is more problematic and will be discussed below. In the pattern shown in Fig. 5b for CR5 after dehydrogenation the TiFe phase was present and a new phase peak appeared at lower angles. There was no clear evidence of the Ti₂Fe phase.

Table 2 presents the Rietveld refinement performed on the patterns of Fig. 5a, as the cold rolled samples presented the best hydrogenation kinetic, the pattern for CR5-after activation and the patterns of the CR1-after activation (not shown in Fig. 5b) were also refined. Starting with the as-atomized sample, three phases were identified: TiFe, Ti₂Fe and a body-centered cubic (BCC) phase. They correspond respectively to the matrix, dark grey and bright phases seen in Fig. 2. The Bragg's peaks of the BCC phase are very broad and almost buried in the background at high angles. This made the phase quantification difficult. However, by keeping the BCC phase

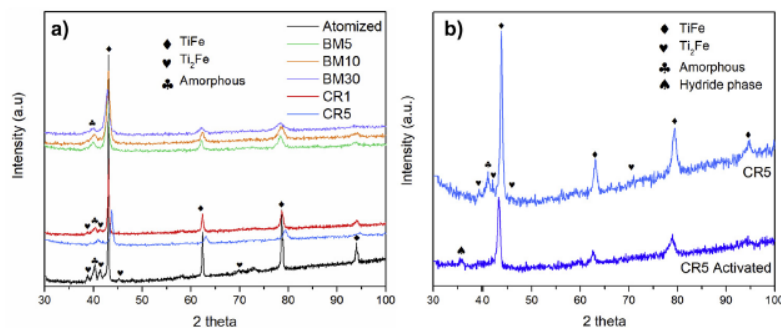


Fig. 5 – X-ray diffraction patterns of a) As-atomized powder, BM5, BM10, BM30, CR1 and CR5; b) CR5 before and after activation.

Table 2 – Rietveld refinement of TiFe-phase and amorphous peak for conditions (the uncertainty on the last significant digit is given by the number in parenthesis).

	Crystallite size (nm)	Strain (μm)	Lattice parameter a (\AA)
As-atomized	77 (3)	0.0417 (1)	2.9878 (1)
CR1	30 (1)	0.077 (4)	2.9882 (3)
CR5	19 (2)	0.14 (1)	2.9881 (9)
BM5	14.2 (6)	0.14 (1)	2.9896 (8)
BM10	12.6 (5)	0.20 (1)	2.9917 (9)
BM30	9 (6)	0.26 (2)	2.9892 (2)
CR1 after activation	25 (2)	0.158 (7)	2.9913 (6)
CR5 after activation	18 (2)	0.22 (2)	2.988 (1)

abundance to a value of 4 wt% as determined from the SEM observations, the abundance of the TiFe and Ti_2Fe were refined to be respectively 77% and 19% which is what was determined from Fig. 1. The lattice parameter of Ti_2Fe phase was determined to be 11.4227 (2) \AA and crystallite size of 6.6 (5) nm. As the BCC phase is of such low abundance, the crystallite size and microstrain have a high error attached to them and therefore are not reported.

The cold rolling and ball milling process decreased the crystallite size (CS) and increased the microstrain of the TiFe phase. As BM is an energetic process the reduction of CS was more important than for CR. CR5 showed the same strain effect as BM for only 5 min. Higher microstrain is also produced by BM. For all patterns, the BCC phase is reduced to one identifiable Bragg peaks at 40° . In fact, a better fit of the pattern is possible by using an amorphous phase instead. However, as we do not have other proofs of transformation of BCC to amorphous phase upon a few cold rolling passes or short ball milling times, the BCC phase is used for the refinements even if just one peak was visible. The Ti_2Fe phase is also affected and the peaks are too broad and the intensity too small for the refinement to accurately determine the CS and strain values.

The patterns of CR1 and CR5 after activation and desorption, showed the increase in microstrain in the TiFe phase. This increase comes from the expansion stress the lattice undergoes when hydrogen is introduced and later removed. After desorption a new Bragg peak appears at 35° pointing to the formation of a stable hydride phase from one of the secondary phases. Since the secondary phases cannot be reliably discerned from the background, their hydrogen uptake cannot be estimated.

The Ti_2Fe metastable phase [43], has not been formally studied regarding its hydrogenation properties due to its difficulty to be synthesized by its own. Future work will be performed in order to obtain more information of the BCC and Ti_2Fe -like phase.

Cold rolling showed a clear kinetic advantage. This may be due to a change of the rate-limiting step of the reaction. Table 3 list the rate-limiting step models that we investigated. To determine the correct rate-limiting step, the left side of each equation was plotted as a function of time. The fits were for a completion ratio ($\alpha = \%H_{\text{abs}}/\%H_{\text{max}}$) from 10 to 90% [44]. The

Table 3 – Rate limiting step models and R^2 values for activation of cold rolling 1 and 5 passes [44–48].

Equation	Model description	Model name	
		CR1	CR5
$\alpha = kt$	Surface controlled	0.8334	0.7878
$[-\ln(1-\alpha)]^{1/2} = kt$	2D growth of existing nuclei with constant interface velocity	0.9757	0.9477
$[-\ln(1-\alpha)]^{1/3} = kt$	3D growth of existing nuclei with constant interface velocity	0.9757	0.9477
$1 - (1-\alpha)^{1/2} = kt$	2D growth with constant interface velocity	0.9196	0.9697
$1 - (1-\alpha)^{1/3} = kt$	3D growth with constant interface velocity	0.9421	0.9808
$(1-\alpha)\ln(1-\alpha) + \alpha = kt$	2D growth, diffusion controlled with decreasing interface velocity	0.9643	0.9302
$1 - (2\alpha/3) - (1-\alpha)^{2/3} = kt$	3D growth, diffusion controlled with decreasing interface velocity	0.9764	0.9993

Underline and bold signifies the models that most closely match the rate limiting step for CR1 and CR5 kinetics.

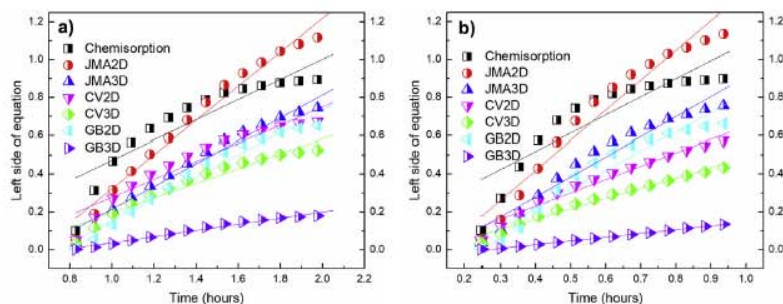


Fig. 6 – Rate limiting step curves for the first hydrogenation of the (a) CR1 and (b) CR5 samples. The straight lines are the best linear fit for each model.

Table 4 – Effect of cold rolling TiFe-based alloys.

	Synthesis process	Activation	Ref.
TiFe+2 wt% Mn 4 wt% Zr (Fresh sample)	Induction melting	2 wt% 12 h	[30]
TiFe+2 wt% Mn 4 wt% Zr (7 days in Air_CR5) (30 days in Air_CR5)	Induction melting	>24 h 1.3 wt% 1.2 wt%	[42]
TiFe+2 wt% Mn 4 wt% Zr (+60 days in Air_CR5)	Gas atomization	2.1 wt% 2 h	This work

model that results on the best linear fit is the rate-limiting step. Fig. 6a and b respectively show the regressions for CR1 and CR5 samples and the corresponding R^2 values are listed in Table 3. For the CR1 sample the JMA2D, JMA3D and GB3D models presents close R^2 values. This makes pinpointing the rate-limiting set to one specific model difficult. The CR5 kinetics more clearly obey to GB3D model.

In order to discuss the influence of gas-atomization as a synthesis technique a comparison is made with the work done by Patel et al. were the same alloy composition, TiFe+2 wt% Mn 4 wt% Zr, was obtained by induction melting under vacuum [30]. A conclusion of that work was that the Zr-rich secondary phase is responsible for the fast-first hydrogenation. In this work, the atomized powder required mechanical processing in order to have activation despite a much finer microstructure. However, as the atomized powder was exposed to the air for more than two months while the sample synthesized by induction melting was always protected means that a definitive conclusion about the microstructure scale could not be reached at this moment. Future work will be performed to evaluate fresh powder without air exposition.

An interesting comparison could be made with Manna et al. work for the same system, TiFe+2 wt% Mn 4 wt% Zr [42]. Their samples were produced by induction melting, hand crushed and left in air for 7 and 30 days in order to see the effect of air exposure and the regeneration ability of CR and BM. The 7- and 30-day samples did not activate after air exposure but were able to activate after CR5 in air. The present work's processing was carried out under the same experimental conditions as reference [42]. As presented above, cold rolling was also beneficial to regenerate the atomized alloy exposed to the air for more than two months. However, as seen in Table 4 cold rolling was much more efficient on the atomized powder than on the induction melt one. The kinetic was faster and the capacity higher. The induction melted sample presented a loss of kinetics and capacity. This may be

an indication that the effectiveness of cold rolling highly depends on the microstructure of the alloy.

Conclusions

- Gas atomization resulted in TiFe matrix with finely distributed secondary phases. No eutectic microstructure was observed by SEM, previously reported for the TiFe + 2 wt%Zr + 4 wt%Mn system produced by induction melting.
- The air exposed atomized powder did not absorb hydrogen and had to be regenerated by cold rolling or ball milling. Cold rolling was shown to be more efficient than ball milling for regeneration. The cold rolled samples absorbed hydrogen quickly and achieved full hydrogen capacity.
- From comparison with induction melted alloys, it seems that the effectiveness of cold rolling depends on the microstructure of the alloy.

Declaration of competing interest

The authors declare that they have no known competing financial interests or personal relationships that could have appeared to influence the work reported in this paper.

REFERENCES

- [1] Bellosta von Colbe J, et al. Application of hydrides in hydrogen storage and compression: achievements, outlook and perspectives. *Int J Hydrogen Energy* 2019;44(15):7780–808.

- [2] Luo Q, Li J, Li B, Liu B, Shao H, Li Q. Kinetics in Mg-based hydrogen storage materials: enhancement and mechanism. *Journal of Magnesium and Alloys* 2019;7(1):58–71.
- [3] de Rango P, Marty P, Fruchart D. Hydrogen storage systems based on magnesium hydride: from laboratory tests to fuel cell integration. *Appl Phys A* 2016;122(2).
- [4] Yartys VA, et al. Magnesium based materials for hydrogen based energy storage: past, present and future. *Int J Hydrogen Energy* 2019;44(15):7809–59.
- [5] Liang G, Huot J, Schulz R. Hydrogen storage properties of the mechanically alloyed LaNi₅-based materials. *J Alloys Compd* 2001;320(1).
- [6] Mordovina VP, Kasimov AV, Alekhin VP, Zhigunov VV. Industrial technologies for production of LaNi₅-based hydride materials. *Hydrogen materials science and chemistry of carbon nanomaterials*. 2007. p. 407–14.
- [7] Tarasov BP, et al. Metal hydride hydrogen storage and compression systems for energy storage technologies. *Int J Hydrogen Energy* 2020. <https://doi.org/10.1016/j.ijhydene.2020.07.085>.
- [8] Lombardo L, Yang H, Züttel A. Study of borohydride ionic liquids as hydrogen storage materials. *Journal of Energy Chemistry* 2019;33:17–21.
- [9] Weidenthaler C. Crystal structure evolution of complex metal aluminum hydrides upon hydrogen release. *Journal of Energy Chemistry* 2020;42:133–43.
- [10] Miracle DB, Senkov ON. A critical review of high entropy alloys and related concepts. *Acta Mater* 2017;01/01/2017;122:448–511.
- [11] Floriano R, et al. Hydrogen storage in TiZrNbFeNi high entropy alloys, designed by thermodynamic calculations. *Int J Hydrogen Energy* 2020;45(58):33759–70.
- [12] Reilly JJ, Wiswall RH. Formation and properties of iron titanium hydride. *Inorg Chem* 1974;13(1):218–22. 01/01 1974.
- [13] Sujan GK, Pan Z, Li H, Liang D, Alam N. An overview on TiFe intermetallic for solid-state hydrogen storage: microstructure, hydrogenation and fabrication processes. *Critical reviews in solid state and materials sciences* 2019:1–18.
- [14] Manna J, Tougas B, Huot J. Mechanical activation of air exposed TiFe + 4 wt% Zr alloy for hydrogenation by cold rolling and ball milling. *Int J Hydrogen Energy* 2018;43(45):20795–800.
- [15] Vega LER, et al. Mechanical activation of TiFe for hydrogen storage by cold rolling under inert atmosphere. *Int J Hydrogen Energy* 2018;43(5):2913–8.
- [16] Emami H, Edalati K, Matsuda J, Akiba E, Horita Z. Hydrogen storage performance of TiFe after processing by ball milling. *Acta Mater* 2015;88:190–5.
- [17] Falcão RB, et al. An alternative route to produce easily activated nanocrystalline TiFe powder. *Int J Hydrogen Energy* 2018;43(33):16107–16.
- [18] Lv P, Guzik MN, Sartori S, Huot J. Effect of ball milling and cryomilling on the microstructure and first hydrogenation properties of TiFe+4 wt.% Zr alloy. *Journal of Materials Research and Technology* 2019;8(2):1828–34.
- [19] Gosselin C, Huot J. First hydrogenation enhancement in TiFe alloys for hydrogen storage doped with yttrium. *Metals* 2019;9(2).
- [20] Kumar S, Tiwari GP, Sonak S, Jain U, Krishnamurthy N. High performance FeTi – 3.1 mass % V alloy for on board hydrogen storage solution. *Energy* 2014;75:520–4.
- [21] Ali W, et al. Hydrogenation properties of Ti-Fe-Mn alloy with Cu and Y as additives. *Int J Hydrogen Energy* 2017;42(4):2229–38.
- [22] Leng H, et al. Effect of cobalt on the microstructure and hydrogen sorption performances of TiFe_{0.8}Mn_{0.2} alloy. *Int J Hydrogen Energy* 2020;45(38):19553–60.
- [23] Leng H, Yu Z, Yin J, Li Q, Wu Z, Chou K-C. Effects of Ce on the hydrogen storage properties of TiFe 0.9 Mn 0.1 alloy. *Int J Hydrogen Energy* 2017;42(37):23731–6.
- [24] Yang T, et al. Effect of chromium, manganese and yttrium on microstructure and hydrogen storage properties of TiFe-based alloy. *Int J Hydrogen Energy* 2020;45(21):12071–81.
- [25] Gosselin C, Huot J. Hydrogenation properties of TiFe doped with zirconium. *Materials* Nov 20 2015;8(11):7864–72.
- [26] Lv P, Huot J. Hydrogenation improvement of TiFe by adding ZrMn₂. *Energy* 2017;138:375–82. 11/01/2017.
- [27] Jain P, Gosselin C, Huot J. Effect of Zr, Ni and Zr 7 Ni 10 alloy on hydrogen storage characteristics of TiFe alloy. *Int J Hydrogen Energy* 2015;40(47):16921–7.
- [28] Jain P, Gosselin C, Skryabina N, Fruchart D, Huot J. Hydrogenation properties of TiFe with Zr7Ni10 alloy as additive. *J Alloys Compd* 2015;636:375–80.
- [29] Lv P, Liu Z, Dixit V. Improved hydrogen storage properties of TiFe alloy by doping (Zr+2V) additive and using mechanical deformation. *Int J Hydrogen Energy* 2019;44(51):27843–52.
- [30] Patel AK, Duguay A, Tougas B, Schade C, Sharma P, Huot J. Microstructure and first hydrogenation properties of TiFe alloy with Zr and Mn as additives. *Int J Hydrogen Energy* 2020;45(1):787–97. <https://doi.org/10.1016/j.ijhydene.2019.10.239>.
- [31] Patel AK, Tougas B, Sharma P, Huot J. Effect of cooling rate on the microstructure and hydrogen storage properties of TiFe with 4 wt% Zr as an additive. *Journal of Materials Research and Technology* 2019;8(6).
- [32] Grant NJ. Rapid solidification of metallic particulates. *JOM* 1983;35(1):20–7.
- [33] Jacobson LA, McKittrick J. Rapid solidification processing. *Mater Sci Eng R Rep* 1994;11(8):355–408.
- [34] Anderson ML, Anderson IE. Gas atomization of metal hydrides for Ni–MH battery applications. *J Alloys Compd* 2000;313(1):47–52.
- [35] Chung SR, Perng TP. Effect of particle size on hydrogenation properties of a gas-atomized AB₅-type alloy. *J Alloys Compd* 2003;353(1–2):289–94.
- [36] Ting J, et al. Gas atomization processing of designed dual-phase intermetallic hydrogen storage alloys. *Mater Sci Eng, A* 2002;329–331:372–6.
- [37] Yoshinaga H, Arami Y, Kajita O, Sakai T. Highly densified-MH electrode using flaky nickel powder and gas-atomized hydrogen storage alloy powder. *J Alloys Compd* 2002;330–332:846–50.
- [38] Kim J-H, Lee H, Hwang K-T, Han J-S. Hydriding behavior in Zr-based AB₂ alloy by gas atomization process. *Int J Hydrogen Energy* 2009;34(23):9424–30.
- [39] *Alloy phase diagrams* (ASM handbook). Materials Park, Ohio: ASM International; 1992.
- [40] T S, DG W. The activation of FeTi for hydrogen storage: a different view*. *Scripta Metall* 1981;15:913–8.
- [41] Lv P, Liu Z. Effect of high zirconium content on hydrogenation properties and anti-poisoning ability of air-exposed TiFe alloy. *Journal of Materials Research and Technology* 2019;8(6).
- [42] Manna J, Tougas B, Huot J. First hydrogenation kinetics of Zr and Mn doped TiFe alloy after air exposure and reactivation by mechanical treatment. *Int J Hydrogen Energy* 2020;45(20).
- [43] C D, ZK H, LB W, QH S, YK W, KH K. A new icosahedral quasicrystal in rapidly solidified FeTi₂. *Scripta Metall* 1986;20:1155–8.
- [44] Lang J, Eagles M, Conradi MS, Huot J. Hydrogenation rate limiting step, diffusion and thermal conductivity in cold rolled magnesium hydride. *J Alloys Compd* 2014;583:116–20.
- [45] An XH, Pan YB, Luo Q, Zhang X, Zhang JY, Li Q. Application of a new kinetic model for the hydriding kinetics of LaNi₅-xAlx (0 < x < 1.0) alloys. *J Alloys Compd* 2010;506(1):63–9.

-
- [46] Khajavi S, Rajabi M, Huot J. Effect of cold rolling and ball milling on first hydrogenation of $\text{Ti}_{0.5}\text{Zr}_{0.5}(\text{Mn}_{1-x}\text{Fe}_x)\text{Cr}_1$, $x = 0, 0.2, 0.4$. *J Alloys Compd* 2019;775:912–20.
- [47] Lv P, Liu Z, Patel AK, Zhou X, Huot J. Influence of ball milling, cold rolling and doping (Zr + 2Cr) on microstructure, first hydrogenation properties and anti-poisoning ability of TiFe alloy. *Met Mater Int* 2019. <https://doi.org/10.1007/s12540-019-00501-1>.
- [48] Pang Y, Li Q. A review on kinetic models and corresponding analysis methods for hydrogen storage materials. *Int J Hydrogen Energy* 2016;41(40):18072–87.

Article 2**Hydrogenation of Ti_xFe_{2-x} -based alloys with overstoichiometric Ti ratio
($x = 1.1, 1.15$ and 1.2)**Ulate-Kolitsky E.^{1*}, Tougas B.², Huot J.¹

¹Institut de Recherche sur l'Hydrogène, Université du Québec à Trois-Rivières, 3351 des Forges, Trois-Rivières, G9A 5H7, Canada

²Centre de Métallurgie du Québec, 3095 Rue Westinghouse Parc Industriel Des Hautes-Forges, Trois-Rivières, Québec, G9A 5E1, Canada

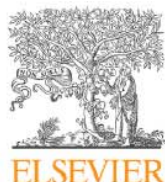
Abstract

The hydrogenation behavior of $Ti_xFe_{2-x} + 4$ wt.% Zr alloys, for $x = 1.1, 1.15$ and 1.2 has been investigated. All compositions presented a multiphase microstructure with a TiFe-matrix along with a secondary Ti_2Fe -like phase and Ti-rich BCC phase. The phase fraction varied with “x”. The increase of titanium abundance makes the alloy more stable, but this comes with a loss of hydrogen capacity. The hydrogen absorbed by the TiFe phase for each composition matched the contribution expected for the corresponding phase abundance. The secondary phases formed stable hydrides Ti_2FeH_x and FCC, these were formed during activation and did not desorb under the experimental conditions. The stoichiometry of the stable hydrides was calculated based on the Rietveld refinement results.

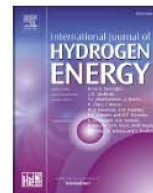
Keywords: TiFe; overstoichiometric-Ti; activation kinetics; Ti_2Fe ; stable hydrides.

ARTICLE IN PRESS

INTERNATIONAL JOURNAL OF HYDROGEN ENERGY XXX (XXXX) XXX

Available online at www.sciencedirect.com

ScienceDirect

journal homepage: www.elsevier.com/locate/he

Hydrogenation of Ti_xFe_{2-x} -based alloys with overstoichiometric Ti ratio ($x = 1.1, 1.15$ and 1.2)

E. Ulate-Kolitsky ^{a,*}, B. Tougas ^b, J. Huot ^a^a Hydrogen Research Institute, Université du Québec à Trois-Rivières, Trois-Rivières, Québec, Canada^b Centre de Métallurgie du Québec, Canada

HIGHLIGHTS

- All samples presented good activation kinetics at RT and 20 bar of hydrogen.
- The stability of the alloy increases with x however reversible capacity is reduced.
- Ti_2Fe -like phase forms a stable hydride with a calculated H/M between 4 and 3.

ARTICLE INFO

Article history:

Received 12 July 2021

Received in revised form

7 September 2021

Accepted 8 September 2021

Available online xxx

Keywords:

TiFe

Overstoichiometric-Ti

Activation kinetics

 Ti_2Fe

Stable hydrides

ABSTRACT

The hydrogenation behavior of $Ti_xFe_{2-x}+4$ wt% Zr alloys, $x = 1.1, 1.15$ and 1.2 has been investigated. All compositions presented a multiphase microstructure with a TiFe-matrix along with a secondary Ti_2Fe -like phase and a Ti-rich BCC phase. The phase fraction varied with "x". The increase of titanium abundance makes the alloy more stable, but this comes with a loss of hydrogen capacity. The formation of stable hydrides (Ti_2FeH_x and FCC) by the secondary phases is reported. The full capacity according to the Rietveld refinement data is calculated. The contribution of each phase matches well with the reversible capacity measured experimentally. The results shown and discussed give insight into the hydrogenation properties of the secondary phases and their effect on a TiFe-based alloy.

© 2021 Hydrogen Energy Publications LLC. Published by Elsevier Ltd. All rights reserved.

Introduction

Due to its low cost and mild operating conditions (room temperature and low pressure) TiFe is an attractive metal hydride for hydrogen storage [1,2]. However, the first hydrogenation or so-called "activation" is usually slow at room temperature. Generally, some form of heat treatment is needed to speed up the activation kinetics. The activation mechanisms have been described being dependent on the

surface condition [3,4]. To improve the activation kinetics different approaches have been studied such as mechanical processing like ball milling [5–9], cold rolling [9,10] and high-pressure torsion [11,12] or the addition of elements such as Cr, Mg, Mn, Ni, V, Y and Zr [6,13–28]. This addition of elements has been shown to improve the activation kinetics and form secondary phases that act as gateways for hydrogen into the TiFe phase and decrease its sensitivity to air [29–31].

Previous studies have shown how the addition of Zr greatly improves the TiFe activation kinetics by forming secondary

* Corresponding author.

E-mail addresses: elena@irh.ca, elena.ulatekolitsky@gmail.com (E. Ulate-Kolitsky).<https://doi.org/10.1016/j.ijhydene.2021.09.077>

0360-3199/© 2021 Hydrogen Energy Publications LLC. Published by Elsevier Ltd. All rights reserved.

phases. The addition of 4 wt% represents the minimum threshold in order to achieve activation without any activation pretreatment [32]. Further increase of Zr proportion enhances the abundance of the secondary phases which improves the kinetics but decreases the reversible capacity [33]. Han et al. measured the effect of added zirconium on the bond characteristics in TiFe alloys and found that the Ti_2Fe and $TiFe_2$ phases formed by the addition of Zr have the same work function while TiFe work function is slightly higher [34].

Extensive work has been done on the phase equilibria diagram of the Ti-Fe-Zr system [35–40]. Zeng et al. experimentally investigated the phase relations of isothermal sections of the Ti-Fe-Zr ternary system at 875 and 1173 K. Four stable ternary phases were identified as τ_1 , τ_2 , τ_3 , τ_4 and eight three-phase equilibria regions were detected. The τ_1 and τ_3 phases presented a C14 structure and the τ_2 , τ_4 phase presented a Fd3-m cubic structure [36]. The ternary phases are of interest for metal hydride research since they are likely to be formed as secondary phases.

Faisal et al. investigated the first cycle hydrogenation properties of Ti-Fe-Zr ternary alloys but their compositions were highly Ti understoichiometric (25 at.% Ti, 50 at.% Fe, 25 at.% Zr) and (38.1 at.% Ti, 33.3 at.% Fe, 28.6 at.% Zr) [35]. It is therefore difficult to compare their finding with the present Ti overstoichiometric system. Nevertheless, their XPS studies indicates the presence of an Fe^0 metallic state directly below the alloy surface, may catalyze hydrogen dissociation at room temperature.

The TiFe alloy with overstoichiometric Ti has been previously studied with the goal of obtaining the metastable phase Ti_2Fe [2,41]. Reilly et al. were the first to try to obtain Ti_2Fe with the goal of studying its hydrogenation properties. However after synthesizing and annealing at 1000 K the stoichiometry Ti_2Fe (63% Ti – 37% Fe) the attempt was unsuccessful and the phases formed were TiFe and Ti [2]. Park et al. synthesized and annealed at 1470 K the composition $Ti_{1.2}Fe$ (60% Ti – 40% Fe). They obtained three phases TiFe (92%), Ti_2Fe (3%) and $Ti_4Fe_{(BCC)}$ (5%). The $Ti_{1.2}Fe$ alloy was able to activate at low pressure and room temperature reaching 2.1 wt% H in 6 h. The composition of each phase was measured separately to study the surface of each phase by XPS. However only the TiFe and

$Ti_4Fe_{(BCC)}$ alloys were able to be synthesized as the Ti_2Fe composition was not possible to synthesize as a single-phase alloy. From this work it was concluded that the improvement of the kinetics is due to the formation of the Ti_2Fe and $Ti_4Fe_{(BCC)}$ phases, or the formation of a Ti-rich oxide layer measured on the $Ti_4Fe_{(BCC)}$ alloy [42].

In this paper we report the hydrogenation behavior of Ti overstoichiometry $Ti_xFe_{2-x} + 4$ wt% Zr ($x = 1.1, 1.15$ and 1.2), and the contribution of the secondary phases.

Methodology

Industrial grade Fe (AISI 1005), Ti (CP Grade 1) and Zr (99.5% pure Alfa Aesar) were used to synthesize all samples. The compositions $Ti_xFe_{2-x} + 4$ wt% Zr ($x = 1.1, 1.15, 1.2$) were prepared by arc melting under argon atmosphere. To achieve homogeneity, each pellet was turned and melted three times. After synthesis, the samples were transferred to an argon filled glovebox for further manipulation. The pellets were crushed in a hardened steel mortar and pestle. The hydrogen storage properties were measured using a home-made Sieverts-type apparatus. The initial hydrogen pressure for kinetic measurements was 20 bars for absorption and 0.1 bar for desorption. All measurements were taken at room temperature.

The crystal structure was determined by X-ray diffraction (XRD) on a Bruker D8 Focus diffractometer with $CuK\alpha$ radiation. Lattice parameters were calculated by Rietveld refinement using the TOPAS software (V6.0) [43]. Microstructural and chemical analysis of the samples were performed on a Hitachi SU3500 scanning electron microscope (SEM) equipped with an Oxford Max⁵⁰ Energy Dispersive X-ray spectrometer (EDS). Image analysis was performed using ImageJ software [44].

Results and discussion

Fig. 1 shows the morphology of all studied compositions. They all show a light grey matrix and secondaries grey and bright

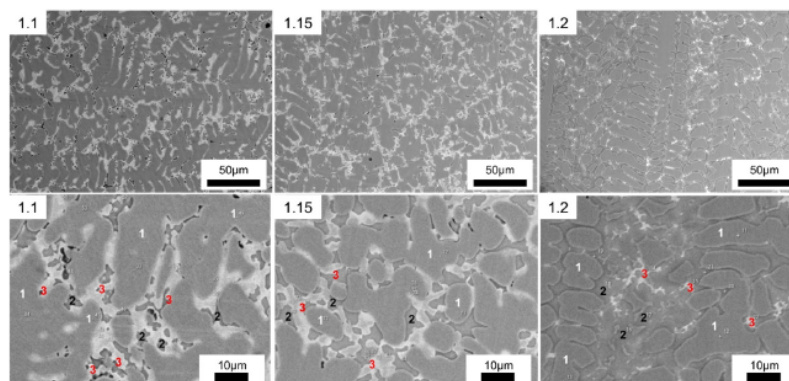


Fig. 1 – Backscattered electron micrograph of overstoichiometric-Ti, $Ti_xFe_{2-x} + 4$ wt% Zr ($x = 1.1, 1.15$ and 1.2).

regions. Increasing Ti from $x = 1.1$ to 1.15 does not drastically change the microstructure. The $x = 1.2$ composition shows a notable decrease of the total area of the secondary bright region. The surface area percentage of the different regions was measured by image analysis. For $x = 1.1$ and 1.15 compositions, the matrix covered about 69% of the area and the secondary regions 31%. In the $x = 1.2$ composition, the secondary bright region covered around 10%. Because of the similar contrast of the matrix and secondary grey region we were unable to quantify by image analysis the relative proportion of these two phases.

The bottom row of Fig. 1 shows the microstructure at higher magnification. The chemical composition of the matrix (1), secondary grey region (2) and secondary bright region (3) was measured by EDS point analysis.

Table 1 presents the EDS measurements for each region. The matrix for the three compositions has the TiFe stoichiometry with only a small substitution of Ti by Zr in the $x = 1.1$ alloy. The secondary grey region composition is essentially the same for the three alloys.

Fig. 2 shows the XRD pattern of all compositions. The main phase is TiFe which corroborates the EDS measurements of the matrix. The other peaks could be indexed to a Ti_2Fe phase

and a BCC phase. The three-phase microstructure matches the phase equilibria reported by Zeng et al. for the (60.6 at.% Ti, 34.6 at.% Fe and 4.8 at.% Zr) alloy. This alloy reportedly presented three stable phases TiFe, a cubic phase called τ_4 of composition (33.3 at.% Fe, 50.4–60.9 at.% Ti) and a $\beta(Ti,Zr)$ phase (Structure type W) [36]. As indicated in Table 2, the secondary bright region for compositions $x = 1.1$ and 1.15 has a Fe abundance close to 33 at.%. This matches perfectly the τ_4 line composition discussed by Zeng et al. [36]. Thus, the secondary region may be associated with the Ti_2Fe -like phase where Zr substitutes Ti and can be written as $(Ti, Zr)_2Fe$. For the $x = 1.2$, as seen in Fig. 1, the secondary bright region has a much smaller area and a different chemical composition. This is reflected in the diffraction pattern where the relative intensities of the Ti_2Fe peaks are reduced. In the case of $x = 1.2$ the stoichiometry associated with this phase in Table 1 is far from the line compound mentioned by Zeng et al. We still indexed this phase as τ_4 but because of the weak peak intensities we could not be affirmative about this.

The BCC structure is associated to the secondary grey region identified in Table 1. The averaged composition of the BCC phase (23 at.% Fe, 73 at.% Ti and 4 at.% Zr) agrees with the $\beta(Ti,Zr)_{BCC}$ phase in Zeng et al.'s work for the A18 alloy (17.5 at.% Fe, 79.3 at.% Ti and 3.2 at.% Zr).

Fig. 3 shows a secondary electron image of the $x = 1.1$ composition. Compared to the high magnification shown in Fig. 1, it is clear that the secondary region is lower than the matrix. This means that the secondary phase is softer than the TiFe phase. The Ti-rich BCC phase would be expected to be softer than an intermetallic hence going deeper in the microstructure with polishing further corroborating the match between the regions observed by SEM and the XRD phases.

Table 2 shows the Rietveld refinement results of the XRD patterns shown in Fig. 2. For the compositions $x = 1.1$ and 1.15, the phase abundance estimated from EDS agrees with the phase fractions calculated from Rietveld refinement. For the $x = 1.2$ compositions, the situation is not as straightforward. The backscattered images show only 10% of the secondary bright region as measured by image analysis. This does not match quantitatively the 19 wt%. However, as mentioned above, because of the weak Bragg's peaks we

Table 1 – EDS analysis of overstoichiometric-Ti, $Ti_xFe_{2-x} + 4$ wt% Zr ($x = 1.1, 1.15$ and 1.2).

X	Spectrum	Region	Average at.%		
			Fe	Ti	Zr
1.1	1	Matrix	51	48	1
	2	Grey region	23	73	4
	3	Bright region I	32	60	8
1.15	1	Matrix	48	52	0
	2	Grey region	25	71	4
	3	Bright region I	33	60	7
1.2	1	Matrix	48	52	0
	2	Grey region	21	75	4
	3	Bright region II	24	61	15

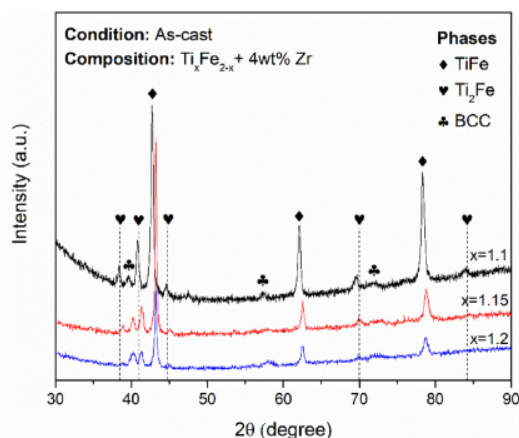


Fig. 2 – X-ray diffraction patterns of overstoichiometric-Ti, $Ti_xFe_{2-x} + 4$ wt% Zr for $x = 1.1, 1.15$ and 1.2.

Table 2 – Rietveld refinement of overstoichiometric-Ti, $Ti_xFe_{2-x} + 4$ wt% Zr where, $x = 1.1, 1.15$ and 1.2 (the uncertainty on the last significant digit is given by the number in parentheses).

	Phase	Phase fraction wt%	Lattice parameters "a" (Å)	Unit cell volume (Å ³)
$x = 1.1$	TiFe	68	2.9844 (1)	26.582 (4)
	Ti_2Fe	28	11.451 (1)	1501.4 (4)
	BCC	4	3.205 (1)	32.91 (3)
$x = 1.15$	TiFe	65	2.9867 (2)	26.642 (6)
	Ti_2Fe	25	11.456 (2)	1503.4 (7)
	BCC	10	3.2021 (9)	32.83 (3)
$x = 1.2$	TiFe	57	2.9895 (4)	26.71 (1)
	Ti_2Fe	19	11.469 (3)	1509 (1)
	BCC	24	3.203 (1)	32.85 (3)

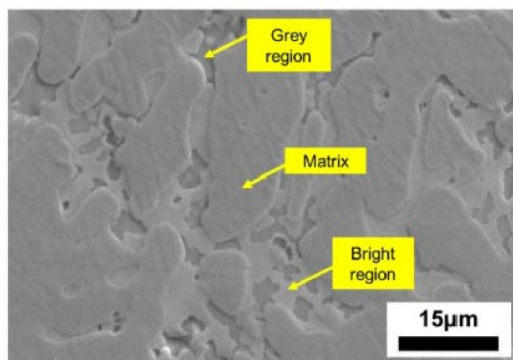


Fig. 3 – Secondary electron micrograph of $\text{Ti}_{1.1}\text{Fe}_{0.9} + 4 \text{ wt } \% \text{ Zr}$.

could not be completely affirmative that this phase has a Ti_2Fe structure.

Fig. 4 shows the activation curves for the as-cast alloys. All samples absorbed hydrogen relatively quickly, reaching full capacity after about 2 h. The activation capacity reached by all samples is higher than the 1.86 wt% H capacity of pure TiFe. This means that the secondary phases are also absorbing hydrogen. Using the phase abundance determined by Rietveld refinement, the contribution of TiFe phase for $x = 1.1, 1.15$ and 1.2 is respectively 1.26 wt% H, 1.21 wt% H and 1.06 wt% H. Thus, the missing capacity should be coming from the secondary phases.

Table 3 shows the activation results of previous studies with different $\text{Ti}_x\text{Fe}_y\text{-Zr}_z\text{-M}_2$ compositions, and the respective secondary phases reported. From a purely kinetic standpoint the samples with Ti overstoichiometry ($x = 1.1, 1.15$ and 1.2) all present the fastest activation. The work done on $\text{TiFe} + 2 \text{ wt } \% \text{ Mn} + 4 \text{ wt } \% \text{ Zr}$ [17], presents the most similar phase fractions of TiFe and Ti_2Fe phases however the kinetics are slower. This points to a synergetic effect occurring due to presence of

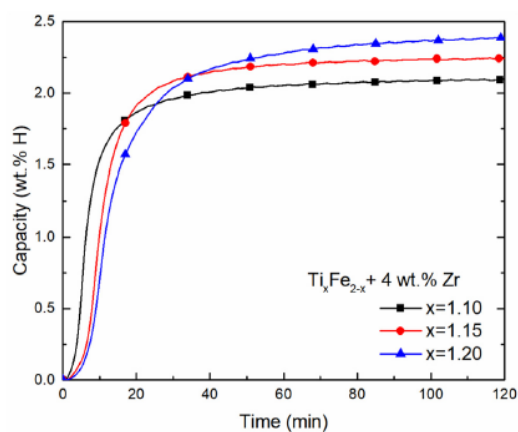


Fig. 4 – Activation of overstoichiometric-Ti, $\text{Ti}_x\text{Fe}_{2-x} + 4 \text{ wt } \% \text{ Zr}$ ($x = 1.1, 1.15$ and 1.2).

BCC with the Ti_2Fe . Also, the capacity increase with Ti points to the BCC phase absorbing hydrogen during activation. However, the kinetics are not further improved by the increase of BCC phase. It is important to keep in mind how the uptake on hydrogen by the secondary phases may ultimately affect the reversible capacity because of the high stability of the secondary hydride phase.

The compositions $x = 1.1, 1.15, 1.2$ were cycled 10 times to corroborate that the reversible capacity was stable (1.21 wt% H, 1.2 wt% H and 1.1 wt% H respectively). The reversible capacity closely matched the contribution calculated for the TiFe phase. Fig. 5 shows the XRD patterns of the samples after cycling (10 cycles). The phases identified are TiFe, a Ti_2Fe -like phase and an FCC phase.

Table 4 shows the lattice parameter and unit cell volume for each phase identified in Fig. 5. Considering that the structure type of the Ti_2Fe phase is Ti_2Ni , we can expect that the Ti_2Fe -like hydride presents the same structure as Ti_2Ni hydride ($\text{Ti}_2\text{NiH}_{2.5}$, Fd-3m, Pearson's symbol cF96) [46]. The volume expansion by a Ti_2Fe -like phase due to hydrogen uptake has been previously reported for two alloys that presented a $(\text{Ti,Zr})_2\text{Fe}$ minor phase. The volume change was reported as 16.4% and 24.4% [35].

The stoichiometry of the hydrided Ti_2Fe -like phase for the $x = 1.1, 1.15$ and 1.2 compositions were determined by the unit cell volume increase due to the hydrogen uptake. In the case of $x = 1.1$ the volume increase is 266 \AA^3 (~16%). Considering 32 formula units per unit cell, this gives a volume per formula unit of 8.3 \AA^3 . Assuming that a single hydrogen atom usually occupies a volume between 2 and 3 \AA^3 , this gives a range of stoichiometry between Ti_2FeH_4 (2.6 wt% H) and $\text{Ti}_2\text{FeH}_{2.8}$ (1.8 wt% H). Similar range has been found for the other two compositions. Using the phase abundance from Table 2, the contribution of the Ti_2Fe -like phase for sample $x = 1.1$ would then be 0.72–0.5 wt% H. Similarly, the capacity coming from Ti_2Fe -like phase for $x = 1.15$ is between 0.57 and 0.39 wt% H and for $x = 1.2$ it is between 0.5 and 0.34 wt% H.

It is well known that the dihydride of a BCC phase is FCC. Thus, the origin of the FCC could be directly related to the presence of a BCC phase in the as-cast alloy. Considering the phase fraction of BCC given in Table 2, the full capacity of the BCC phase for samples, $x = 1.1, 1.15$ and 1.2 are respectively 3 wt% H, 5.6 wt% H and 3.8 wt% H. As the H/M of the FCC phase is 2, the 'theoretical' capacity of the FCC should be 3.7 wt% H which agrees relatively well with the estimation from X-ray diffraction patterns.

Fig. 6 presents the pressure composition isotherm (PCI) curves after activation and desorption. The absorption 1st plateau (~200 kPa) for all samples is at a lower pressure than the ones reported for pure-TiFe where the absorption plateau is ~500 kPa. However, this drop in plateau pressure has been previously reported for $\text{TiFe} + X \text{ wt } \% \text{ Zr}$ [30]. Regarding the effect of increasing x , it slightly stabilizes the hydride as indicated by a lower pressure of the plateau. The plateau pressure decreasing with the increase of x value is possibly due to the slight change of composition of TiFe phase. As seen in Table 2, this change of composition leads to an increase of the lattice parameter with x . A bigger lattice parameter means a bigger interstice for hydrogen and thus a lower plateau pressure.

Table 3 – Summary of activation results of previous studies and current work.

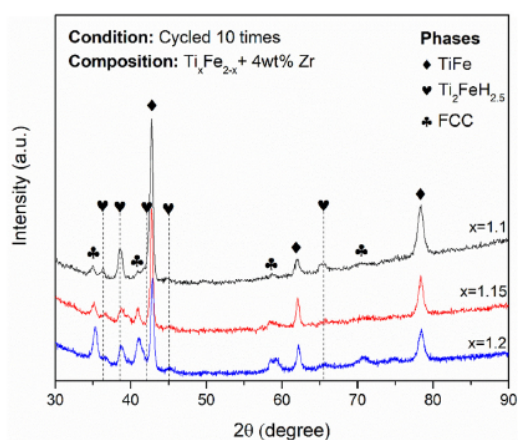
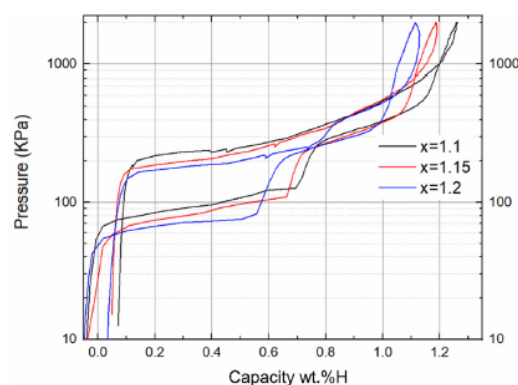
Composition	Synthesis	Phases present	Capacity	Ref.
TiFe+4 wt% Zr	Arc-melting No heat treatment	TiFe Minor secondary phases not identified	1.45 wt% H 7 h 2.5 MPa @25 °C	[33]
TiFe+4 wt% Zr	Arc-melting Annealed 1173 K–24 h	TiFe Minor secondary phases not identified	0.1 wt% H 6 h (poor kinetics) 2 MPa @25 °C	[45]
Ti _{1.2} Fe	Arc-melting Homogenization Annealing 1473 K–10 h	TiFe (91.8 wt%) Ti ₂ Fe (2.8 wt%) Ti ₄ Fe _(BCC) (5.4 wt%)	2.1 wt% H 6 h 4 MPa @25 °C	[42]
TiFe+2 wt% Mn +4 wt% Zr	Induction melting No heat treatment	TiFe (70 wt%) Ti ₂ Fe(28 wt%) Ti (2 wt%)	2 wt% H ~10 h 2 MPa @25 °C	[17]
TiFe _{0.85} Mn _{0.05}	Induction melting Annealed 1273 K–168 h Water quenched	TiFe (94.8 wt%) B-Ti (2.8 wt%) Ti ₄ Fe ₂ O (2.4 wt%)	1.73 wt% H Total time 7 h with 6 h incubation 2.5 MPa @25 °C	[26]
Ti _{1.1} Fe _{0.9} +4 wt% Zr	Arc-melting No heat treatment	TiFe (68 wt%) Ti ₂ Fe (28 wt%) BCC (4 wt%)	2.1 wt% H 2 h 2 MPa @25 °C	Current work
Ti _{1.15} Fe _{0.85} +4 wt% Zr		TiFe (65 wt%) Ti ₂ Fe (25 wt%) BCC (10 wt%)	2.25 wt% H 2 h 2 MPa @25 °C	
Ti _{1.2} Fe _{0.8} +4 wt% Zr		TiFe (57 wt%) Ti ₂ Fe (19 wt%) BCC (24 wt%)	2.4 wt% H 2 h 2 MPa @25 °C	

The small loop, seen at high pressure for the three isotherms is due to experimental artefact. At high pressure, there is a systematic shift of the pressure due to the hysteresis of the strain gauge. This loop has also the effect of shifting the capacity toward lower value. As the effect is accumulative, this is the reason for the small negative value of the capacity at the end of desorption.

The PCI capacity closely matches the calculated capacities attributed to TiFe phase. This confirms how the TiFe phase is responsible for the reversible capacity of the alloy. PCI

Table 4 – Lattice parameter and unit cell volume of cycled overstoichiometric-Ti, Ti_xFe_{2-x} + 4 wt% Zr where, x = 1.1, 1.15 and 1.2 (the uncertainty on the last significant digit is given by the number in parenthesis).

	Phase	Lattice parameters (Å)	Unit cell volume (Å ³)
x = 1.1	TiFe	2.9877 (3)	26.670 (7)
	Ti ₂ FeH _x	12.092 (2)	1768 (1)
	FCC	4.421 (2)	86.4 (1)
x = 1.15	TiFe	2.9868 (4)	26.65 (1)
	Ti ₂ FeH _x	12.010 (7)	1732 (3)
	FCC	4.418 (2)	86.2 (1)
x = 1.2	TiFe	2.9910 (4)	26.75 (1)
	Ti ₂ FeH _x	12.094 (4)	1769 (2)
	FCC	4.4157 (9)	86.10 (5)

**Fig. 5 – X-ray diffraction patterns of the cycled overstoichiometric-Ti, Ti_xFe_{2-x} + 4 wt% Zr (x = 1.1, 1.15 and 1.2).****Fig. 6 – Pressure Composition Isotherm (23 °C) of overstoichiometric-Ti, Ti_xFe_{2-x} + 4 wt% Zr (x = 1.1, 1.15 and 1.2).**

measurements after cycling (not shown) indicated that the reversible capacity remained stable with cycling.

Conclusions

Alloys of composition $Ti_xFe_{2-x} + 4$ wt% Zr alloys, with $x = 1.1, 1.15$ and 1.2 were investigated. We found that all alloys are composed of a main TiFe phase with zirconium-rich secondary phases. The secondary phases were identified as a Ti_2Fe -like phase and a Ti-rich BCC phase. The secondary phases match the τ_4 and $\beta(Ti,Zr)$ phases described by Zeng et al. The first hydrogenation kinetics are fast due to the presence of these secondary phases which act as gateways for hydrogen. Both secondary phases form stable hydrides that do not desorb under the present experimental conditions (vacuum at room temperature). The hydride capacity of all phases was determined and match well with the reversible capacity measured experimentally. The reversible capacity is fully attributed to the TiFe phase. Pressure-composition isotherms taken at room temperature shown that increasing the relative amount of titanium makes the alloy more stable by increasing the Ti content in the TiFe phase.

Declaration of competing interest

The authors declare that they have no known competing financial interests or personal relationships that could have appeared to influence the work reported in this paper.

REFERENCES

- [1] Sujjan GK, Pan Z, Li H, Liang D, Alam N. An overview on TiFe intermetallic for solid-state hydrogen storage: microstructure, hydrogenation and fabrication processes. *Crit Rev Solid State Mater Sci* 2019;1–18.
- [2] Reilly JJ, Wiswall RH. Formation and properties of iron titanium hydride. *Inorg Chem* 1974;13(1):218–22. 1974/01/01.
- [3] Schober T, Westlake DG. The activation of fcti for hydrogen storage: a different view. *Scripta Metall* 1981;15:913–8.
- [4] Schlapbach L, Riesterer T. The activation of FeTi for hydrogen absorption. *Appl Phys A* 1983;32:169–82.
- [5] Lv P, Guzik MN, Sartori S, Huot J. Effect of ball milling and cryomilling on the microstructure and first hydrogenation properties of TiFe+4 wt.% Zr alloy. *J Mater Res Technol* 2019;8(2):1828–34.
- [6] Silva RA, et al. Room temperature hydrogen absorption by Mg and Mg TiFe nanocomposites processed by high-energy ball milling. *Int J Hydrogen Energy* 2018;43(27):12251–9.
- [7] Falcão RB, et al. An alternative route to produce easily activated nanocrystalline TiFe powder. *Int J Hydrogen Energy* 2018;43(33):16107–16.
- [8] Guo F, Namba K, Miyaoka H, Jain A, Ichikawa T. Hydrogen storage behavior of TiFe alloy activated by different methods. *Mater Lett X* 2021;9. <https://doi.org/10.1016/j.mblux.2021.100061>.
- [9] Ulate-Kolitsky E, Tougas B, Neumann B, Schade C, Huot J. First hydrogenation of mechanically processed TiFe-based alloy synthesized by gas atomization. *Int J Hydrogen Energy* 2021;46(10):7381–9. <https://doi.org/10.1016/j.ijhydene.2020.11.237>.
- [10] Vega LER, et al. Mechanical activation of TiFe for hydrogen storage by cold rolling under inert atmosphere. *Int J Hydrogen Energy* 2018;43(5):2913–8.
- [11] Edalati K, Matsuda J, Yanagida A, Akiba E, Horita Z. Activation of TiFe for hydrogen storage by plastic deformation using groove rolling and high-pressure torsion: similarities and differences. *Int J Hydrogen Energy* 2014;39(28):15589–94.
- [12] Edalati K, Matsuda J, Arita M, Daio T, Akiba E, Horita Z. Mechanism of activation of TiFe intermetallics for hydrogen storage by severe plastic deformation using high-pressure torsion. *Appl Phys Lett* 2013;103(14). <https://doi.org/10.1063/1.4823555>.
- [13] Jung JY, Lee Y-S, Suh J-Y, Huh J-Y, Cho YW. Tailoring the equilibrium hydrogen pressure of TiFe via vanadium substitution. *J Alloys Compd* 2021;854. <https://doi.org/10.1016/j.jallcom.2020.157263>.
- [14] Jung JY, et al. Effect of Cr addition on room temperature hydrogenation of TiFe alloys. *Int J Hydrogen Energy* 2021. <https://doi.org/10.1016/j.ijhydene.2021.03.096>.
- [15] Ha T, et al. Hydrogen storage behavior and microstructural feature of a TiFe–ZrCr2 alloy. *J Alloys Compd* 2021;853. <https://doi.org/10.1016/j.jallcom.2020.157099>.
- [16] Yang T, et al. Effect of chromium, manganese and yttrium on microstructure and hydrogen storage properties of TiFe-based alloy. *Int J Hydrogen Energy* 2020;45(21):12071–81.
- [17] Patel AK, Duguay A, Tougas B, Schade C, Sharma P, Huot J. Microstructure and first hydrogenation properties of TiFe alloy with Zr and Mn as additives. *Int J Hydrogen Energy* 2019;45(1).
- [18] Lv P, Liu Z, Dixit V. Improved hydrogen storage properties of TiFe alloy by doping (Zr+V) additive and using mechanical deformation. *Int J Hydrogen Energy* 2019;44(51):27843–52.
- [19] Gosselin C, Huot J. First hydrogenation enhancement in TiFe alloys for hydrogen storage doped with yttrium. *Metals* 2019;9(2).
- [20] Lv P, Huot J. Hydrogenation improvement of TiFe by adding ZrMn2. *Energy* 2017;138:375–82. 2017/11/01.
- [21] Ali W, et al. Hydrogenation properties of Ti-Fe-Mn alloy with Cu and Y as additives. *Int J Hydrogen Energy* 2017;42(4):2229–38. <https://doi.org/10.1016/j.ijhydene.2016.09.037>.
- [22] Jain P, Gosselin C, Skryabina N, Fruchart D, Huot J. Hydrogenation properties of TiFe with Zr7Ni10 alloy as additive. *J Alloys Compd* 2015;636:375–80.
- [23] Jain P, Gosselin C, Huot J. Effect of Zr, Ni and Zr 7 Ni 10 alloy on hydrogen storage characteristics of TiFe alloy. *Int J Hydrogen Energy* 2015;40(47):16921–7.
- [24] Kumar S, Tiwari GP, Sonak S, Jain U, Krishnamurthy N. High performance FeTi – 3.1 mass % V alloy for on board hydrogen storage solution. *Energy* 2014;75:520–4.
- [25] Park KB, et al. Effect of Fe substitution by Mn and Cr on first hydrogenation kinetics of air-exposed TiFe-based hydrogen storage alloy. *Mater Char* 2021;178. <https://doi.org/10.1016/j.matchar.2021.111246>.
- [26] Dematteis Erika Michela, Capurso Giovanni, Jepsen Julian, Cuevas Fermin, Latroche Michel. Fundamental hydrogen storage properties of TiFe-alloy with partial substitution of Fe by Ti and Mn. *J Alloys Compd* 2021;874.
- [27] Lv P, Huot J. Hydrogen storage properties of Ti0.95FeZr0.05, TiFe0.95Zr0.05 and TiFeZr0.05 alloys. *Int J Hydrogen Energy* 2016;41(47):22128–33.
- [28] Guéguen A, Latroche M. Influence of the addition of vanadium on the hydrogenation properties of the compounds TiFe0.9Vx and TiFe0.8Mn0.1Vx ($x = 0, 0.05$ and 0.1). *J Alloys Compd* 2011;509(18):5562–6. <https://doi.org/10.1016/j.jallcom.2011.02.036>.

- [29] Manna J, Tougas B, Huot J. First hydrogenation kinetics of Zr and Mn doped TiFe alloy after air exposure and reactivation by mechanical treatment. *Int J Hydrogen Energy* 2020;45(20).
- [30] Lv P, Liu Z. Effect of high zirconium content on hydrogenation properties and anti-poisoning ability of air-exposed TiFe alloy. *J Mater Res Technol* 2019;8(6):5972–83. <https://doi.org/10.1016/j.jmrt.2019.09.072>.
- [31] Manna J, Tougas B, Huot J. Mechanical activation of air exposed TiFe + 4 wt% Zr alloy for hydrogenation by cold rolling and ball milling. *Int J Hydrogen Energy* 2018;43(45):20795–800.
- [32] Gosselin C, Huot J. Hydrogenation properties of TiFe doped with zirconium (in eng) *Materials* Nov 20 2015;8(11):7864–72.
- [33] Gosselin C, Santos D, Huot J. First hydrogenation enhancement in TiFe alloys for hydrogen storage. *J Phys Appl Phys* 2017;50(37). <https://doi.org/10.1088/1361-6463/aa7d6a>.
- [34] Han H, et al. Determining the effect of added zirconium on the bond character in TiFe alloys using scanning Kelvin probe force microscopy. *Appl Surf Sci* 2020;517. <https://doi.org/10.1016/j.apsusc.2020.146163>.
- [35] Faisal M, Suh J-Y, Lee Y-S. Understanding first cycle hydrogenation properties of Ti–Fe–Zr ternary alloys. *Int J Hydrogen Energy* 2021;46(5):4241–51. <https://doi.org/10.1016/j.ijhydene.2020.11.025>.
- [36] Zeng L, Xu G, Liu L, Bai W, Zhang L. Experimental investigation of phase equilibria in the Ti-Fe-Zr system. *Calphad* 2018;61:20–32. <https://doi.org/10.1016/j.calphad.2018.02.005>.
- [37] Surowiec Z, Wiertel M, Beskrovnyi AI, Sarzy ski J, Milczarek JJ. Investigations of microscopic magnetic properties of the pseudo-binary system (Zr_{1-x}Ti_x)Fe₂. *J Phys Condens Matter* 2003;15(37):6403–14. <https://doi.org/10.1088/0953-8984/15/37/008>.
- [38] Velikanova T, Komiyyenko K. Iron – titanium – zirconium. In: *Iron systems, part 5, Landolt-Börnstein - group IV physical chemistry*; 2009. p. 702–20 [Chapter 34].
- [39] Zhou G, Zeng D, Liu Z. Phase equilibria in the Fe–Ti–Zr system at 1023K. *J Alloys Compd* 2010;490(1–2):463–7. <https://doi.org/10.1016/j.jallcom.2009.10.046>.
- [40] Zhou G-j, Jin S, Liu L-b, Liu H-s, Jin Z-p. Determination of isothermal section of Fe-Ti-Zr ternary system at 1173 K. *Trans Nonferrous Metals Soc China* 2007;17(5):963–6. [https://doi.org/10.1016/s1003-6326\(07\)60208-8](https://doi.org/10.1016/s1003-6326(07)60208-8).
- [41] Fokin VN, Fokina EE, Korobov II, Tarasov BP. Phase transformations in the systems Ti₂Fe–H₂ and Ti₂Fe–NH₃. *Russ J Inorg Chem* 2016;61(7):891–5. <https://doi.org/10.1134/s0036023616070044>.
- [42] Park KB, et al. Characterization of microstructure and surface oxide of Ti_{1.2}Fe hydrogen storage alloy. *Int J Hydrogen Energy* 2021;46(24):13082–7. <https://doi.org/10.1016/j.ijhydene.2021.01.105>.
- [43] Coelho Alan A. TOPAS. Bruker; 2021. V6.
- [44] ImageJ. Bethesda, Maryland, USA: U. S. National Institutes of Health; 1997-2018 [Online]. Available: <https://imagej.nih.gov/ij/>.
- [45] Patel AK, Sharma P, Huot J. Effect of annealing on microstructure and hydrogenation properties of TiFe + X wt % Zr (X = 4, 8). *Int J Hydrogen Energy* 2018;43(12):6238–43. <https://doi.org/10.1016/j.ijhydene.2018.02.029>.
- [46] Buchner H, Gutjahr MA, Beccu KD, Saeufferer H. Hydrogen in intermetallic phases: the system titanium–nickel–hydrogen. *Wasserstoff in intermetallischen Phasen am Beispiel des Systems Titan–Nickel–Wasserstoff* 1972; 1972. Germany.

Article 3**First hydrogenation of TiFe + 20 wt.% Ti (Ti_{1.2}Fe_{0.8})**Elena Ulate-Kolitsky^{1*}, Bernard Tougas², Jacques Huot¹

¹Institut de Recherche sur l'Hydrogène, Université du Québec à Trois-Rivières, 3351 des Forges, Trois-Rivières, G9A 5H7, Canada

²Centre de Métallurgie du Québec, 3095 Rue Westinghouse Parc Industriel Des Hautes-Forges, Trois-Rivières, Québec, G9A 5E1, Canada

In this paper, we report the first hydrogenation (activation) of Ti_{1.2}Fe_{0.8} alloy synthesized by induction-melting (9 kg ingot). The alloy presented a three-phases structure composed of a main TiFe phase, a secondary Ti₂Fe phase and a Ti-rich BCC phase. The alloy required cold rolling to achieve activation at room temperature. However, it did so with good kinetics, reaching saturation (2.6 wt.% H) in about 6 hours. After activation, the phases identified were TiFe, Ti₂FeH_x and an FCC phase. The Ti₂FeH_x and FCC are the stable hydrides formed by the secondary Ti₂Fe and BCC phases respectively. The stoichiometry of the Ti₂FeH_x was calculated to be between $x = 3.2 - 4.75$. As the microstructure obtained by an industrial-scale synthesis method (induction-melted) may be different than the one obtained by laboratory-scale method (arc-melting), a small 3-gram sample of Ti_{1.2}Fe_{0.8} was synthesized by arc-melting. The lab-scale sample activated (2 wt.% H in ~ 12 h) without the need of cold rolling. The phases identified for the lab-scale sample matched those found for the induction-melted sample. The phase fractions differed between the samples; the lab-scale sample presented a lower abundance and a finer distribution of the secondary phases. This explains the difference in the kinetics and H capacity. Based on these results it can be concluded that the alloy of composition Ti_{1.2}Fe_{0.8} can absorb hydrogen without the need for a heat treatment and that finer microstructures have a strong influence on the activation kinetics regardless of the secondary phases' phase fractions.

Keywords: TiFe; overstoichiometry; activation kinetics; Ti₂Fe; stable hydrides.

International Journal of Hydrogen Energy
First hydrogenation of TiFe + 20 wt.% Ti (Ti_{1.2}Fe_{0.8})
 --Manuscript Draft--

Manuscript Number:	
Article Type:	Full Length Article
Section/Category:	Hydrides / Hydrogen Storage
Keywords:	TiFe; overstoichiometry; activation kinetics; Ti ₂ Fe; stable hydrides
Corresponding Author:	Elena Ulate-Kolitsky Université du Québec à Trois-Rivières: Université du Québec a Trois-Rivieres Trois-Rivieres, Quebec CANADA
First Author:	Elena Ulate-Kolitsky
Order of Authors:	Elena Ulate-Kolitsky Bernard Tougas Jacques Huot
Abstract:	In this paper, we report the first hydrogenation (activation) of Ti _{1.2} Fe _{0.8} alloy synthesized by induction-melting (9 kg ingot). The alloy presented a three-phases structure composed of a main TiFe phase, a secondary Ti ₂ Fe phase and a Ti-rich BCC phase. The alloy required cold rolling to achieve activation at room temperature. However, it did so with good kinetics, reaching saturation (2.6 wt.% H) in about 6 hours. After activation, the phases identified were TiFe, Ti ₂ FeH _x and an FCC phase. The Ti ₂ FeH _x and FCC are the stable hydrides formed by the secondary Ti ₂ Fe and BCC phases respectively. The stoichiometry of the Ti ₂ FeH _x was calculated to be between $x = 3.2 - 4.75$. As the microstructure obtained by an industrial-scale synthesis method (induction-melted) may be different than the one obtained by laboratory-scale method (arc-melting), a small 3-gram sample of Ti _{1.2} Fe _{0.8} was synthesized by arc-melting. The lab-scale sample activated (2 wt.% H in ~ 12 h) without the need of cold rolling. The phases identified for the lab-scale sample matched those found for the induction-melted sample. The phase fractions differed between the samples; the lab-scale sample presented a lower abundance and a finer distribution of the secondary phases. This explains the difference in the kinetics and H capacity. Based on these results it can be concluded that the alloy of composition Ti _{1.2} Fe _{0.8} can absorb hydrogen without the need for a heat treatment and that finer microstructures have a strong influence on the activation kinetics regardless of the secondary phases' phase fractions.

Cover Letter

International Journal of Hydrogen Energy

Cover letter

Elena Ulate-Kolitsky
PhD Student, Université du Québec à Trois-Rivières
Hydrogen Research Institute

10/December/2021

Dear Editors,

We wish to submit a new manuscript entitled "First hydrogenation of TiFe + 20 wt.% Ti ($Ti_{1.2}Fe_{0.8}$)". The manuscript presents the results from the work done as part of Ms. Ulate-Kolitsky's PhD project that focuses on the study of TiFe alloys for hydrogen storage. We confirm that this work is original and has not been published elsewhere nor is it currently under consideration for publication elsewhere.

In this paper we report the first hydrogenation (activation) of $Ti_{1.2}Fe_{0.8}$ alloy synthesized by induction-melting (9 kg ingot) and arc-melting (3 g pellet). The compositions studied yielded fast activation kinetics at room temperature and low pressure. The compositions also produced secondary phases that have only been reported once before as hydride forming phases. In this work the hydrogen capacity of the secondary phases is calculated from the unit cell volume expansion after hydrogenation. This gives more insight on what the nature of the secondary phases is. The contrast between the microstructures obtained by the synthesis methods also yielded an interesting comparison and discussion about the effect of microstructure.

Please address all correspondence concerning this manuscript to elena@irh.ca and to Jacques.huot@uqtr.ca.

Thank you for the consideration of this manuscript.

Sincerely,



Elena Ulate-Kolitsky

1 First hydrogenation of TiFe + 20 wt.% Ti ($\text{Ti}_{1.2}\text{Fe}_{0.8}$)

2 Ulate-Kolitsky E.¹, Tougas B.², Huot J.^{1*}

3 ¹Hydrogen Research Institute, Université du Québec à Trois-Rivières,

4 ²Centre de métallurgie du Québec,

5 elena@irh.ca

6 7 8 **Abstract**

9 In this paper, we report the first hydrogenation (activation) of $\text{Ti}_{1.2}\text{Fe}_{0.8}$ alloy synthesized by
10 induction-melting (9 kg ingot). The alloy presented a three-phases structure composed of a main
11 TiFe phase, a secondary Ti_2Fe phase and a Ti-rich BCC phase. The alloy required cold rolling to
12 achieve activation at room temperature. However, it did so with good kinetics, reaching saturation
13 (2.6 wt.% H) in about 6 hours. After activation, the phases identified were TiFe, Ti_2FeH_x and an
14 FCC phase. The Ti_2FeH_x and FCC are the stable hydrides formed by the secondary Ti_2Fe and BCC
15 phases respectively. The stoichiometry of the Ti_2FeH_x was calculated to be between $x=3.2-4.75$.
16 As the microstructure obtained by an industrial-scale synthesis method (induction-melted) may be
17 different than the one obtained by laboratory-scale method (arc-melting), a small 3-gram sample
18 of $\text{Ti}_{1.2}\text{Fe}_{0.8}$ was synthesized by arc-melting. The lab-scale sample activated (2 wt.% H in ~ 12 h)
19 without the need of cold rolling. The phases identified for the lab-scale sample matched those
20 found for the induction-melted sample. The phase fractions differed between the samples; the lab-
21 scale sample presented a lower abundance and a finer distribution of the secondary phases. This
22 explains the difference in the kinetics and H capacity. Based on these results it can be concluded
23 that the alloy of composition $\text{Ti}_{1.2}\text{Fe}_{0.8}$ can absorb hydrogen without the need for a heat treatment
24 and that finer microstructures have a strong influence on the activation kinetics regardless of the
25 secondary phases' phase fractions.

26
27 **Keywords:** TiFe; overstoichiometry; activation kinetics; Ti_2Fe ; stable hydrides.

28
29
30
31
32
33
34

35 Introduction

36

37 TiFe is an attractive hydride forming alloy for hydrogen storage due to its low cost and mild
38 operation conditions (room temperature and low pressure) [1, 2]. However, TiFe is highly sensitive
39 to air and forms a passivation layer that inhibits the activation. Generally, an activation heat
40 treatment is needed to speed up the activation kinetics of pure TiFe. This activation heat treatment
41 requires cycling between high temperature and room temperature under high hydrogen pressure
42 [3]. The focus of TiFe research is the improvement of the activation kinetics by different
43 approaches that will ultimately eliminate the need for an activation heat treatment. For example,
44 the use of mechanical processing techniques (ball milling, cold rolling, high-pressure torsion) [4-
45 12] and/or the addition of alloying elements [13-20] have both shown to improve the kinetics.

46

47 Several studies on the alloying of TiFe with Zr [21-24] and Zr-Mn [8, 25-27] have reported
48 the formation of a Ti₂Fe-like secondary phase. Little is known of this phase because of it is difficult
49 to synthesize. Reilly et al. were the first to try to obtain Ti₂Fe to study its hydrogenation properties.
50 However after synthesizing and annealing at 1000K the stoichiometric Ti₂Fe (63% Ti – 37% Fe),
51 the attempt was unsuccessful and the phases formed were TiFe and Ti. More recently Park et al.
52 synthesized by arc-melting and annealed at 1470K Ti_{1.2}Fe alloy (60% Ti – 40% Fe) [28]. In their
53 work they reported three phases TiFe (92%), Ti₂Fe (3%) and Ti₄Fe BCC (Body Centred Cubic)
54 (5%). The Ti_{1.2}Fe alloy was activated at low pressure and room temperature reaching 2.1 wt.% H
55 in 6 hours. One conclusion of their work was that the kinetics improvement was due to the
56 formation of the Ti₂Fe and Ti₄Fe(BCC) phases.

57

58 The possibility of using Ti as the alloying element instead of other more expensive transition
59 metals or rare earth elements to improve the activation kinetics of TiFe is of great interest because
60 it would decrease the alloy cost. Besides the alloying elements, the viability of using an industrial-
61 scale synthesis method for the production of the alloy is also of importance for commercialization.

62

63 In this paper, we report the activation behavior of an induction-melted (9 kg ingot) TiFe +
64 20 wt.% Ti (Ti_{1.2}Fe_{0.8}) alloy, and the phases present before and after hydrogenation. The same

65 composition was also synthesized by arc-melting (3 g pellet) in order to compare the
66 microstructures of each sample.

67

68 **Methodology**

69

70 Industrial grade Fe (1005), Ti (CP Grade 1) and Zr (99.5% pure Alfa Aesar) were used to
71 synthesize all samples. The compositions $Ti_{1.2}Fe_{0.8}$ was synthesized by induction melting (9 kg
72 ingot) and by arc melting (3 g pellet) under argon atmosphere. After synthesis, the samples were
73 transferred to a glovebox for further manipulation under argon. The pellets and ingot samples were
74 crushed in a hardened steel mortar and pestle.

75

76 The induction melted samples were cold rolled (5 passes) in air using a modified version of a
77 Durston DRM 130 model where the crushed sample was rolled vertically between stainless steel
78 plates to avoid contamination of the powder by the rollers.

79 The hydrogen storage properties were measured using a home-made Sieverts-type apparatus. The
80 initial hydrogen pressures for kinetic measurements were 20 bars for absorption and 0.1 bar for
81 desorption. All measurements were taken at room temperature.

82

83 The crystal structures were determined from X-ray powder diffraction (XRD) on a Bruker D8
84 Focus diffractometer with a $CuK\alpha$ radiation source. Lattice parameters were calculated by
85 Rietveld refinement using the TOPAS software (V6.0) [29]. Microstructural and chemical analysis
86 of the samples were performed on a Hitachi SU3500 scanning electron microscope (SEM)
87 equipped with an Oxford Max⁵⁰ Energy Dispersive X-ray spectrometer (EDS).

88

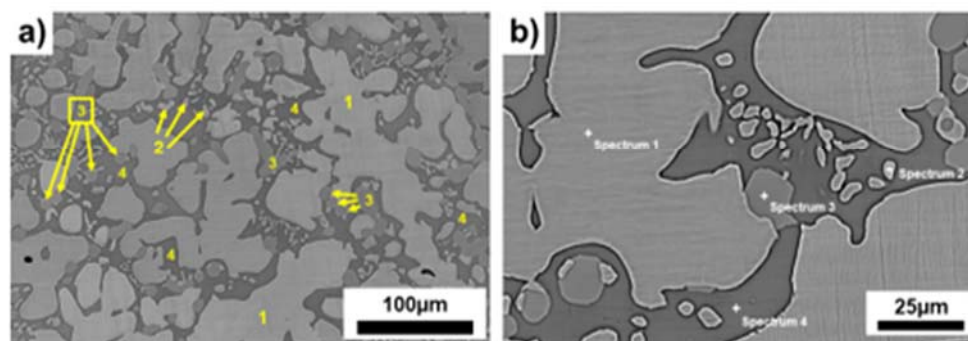
89 **Results and Discussion**

90

91 Figure 1a) shows the microstructure of the induction melted $Ti_{1.2}Fe_{0.8}$ 9 kg ingot. Three
92 regions are observed in the micrograph: a bright main region (1-2) and two grey regions. A grey
93 region (3) that consists of rounded areas that are in contact with the bright region and a dispersed
94 dark-grey region (4). The phase fractions were measured by image processing. The main bright
95 region accounts for 58% of the micrographs area and the secondary grey and dark-grey regions for

96 12 and 30% respectively. Figure 1b) shows a higher magnification image of the regions analyzed
 97 by EDX. The chemical composition of the overall alloy and each specific region was measured,
 98 and the results are presented in Table 1.

99



100

101 **Figure 1.** Backscattered electron micrograph of the induction melted $Ti_{1.2}Fe_{0.8}$ alloy a) low
 102 magnification and b) higher magnifications – EDX point spectrums.

103

104 **Table 1.** EDX analysis of the induction melted $Ti_{1.2}Fe_{0.8}$ alloy (uncertainty is ± 1 for all values).

	Region	Ti wt. %	Fe wt. %
Nominal composition	N/A	56	44
Overall composition	N/A	59	41
Spectra 1 and 2	Bright	49	51
Spectrum 3	Grey	63	37
Spectrum 4	Dark-grey	79	21

105

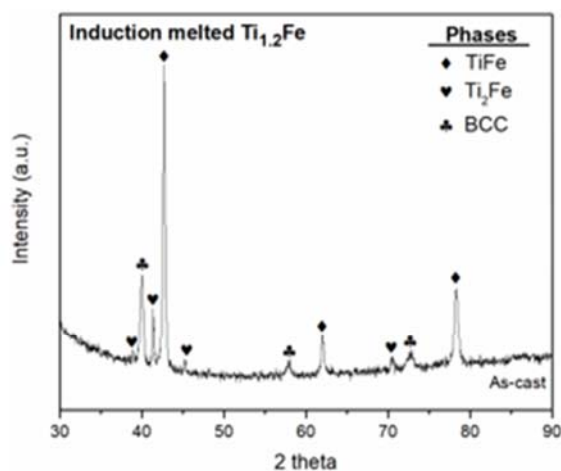
106 The overall composition measurement shows how the measured composition of the alloy is
 107 $Ti_{1.26}Fe_{0.74}$ instead of the nominal composition $Ti_{1.2}Fe_{0.8}$. This difference is not uncommon when
 108 working with industrial synthesis methods. Since the difference is small, we will use the nominal
 109 composition in our discussion. The main phase (Spectra 1 and 2) matches the composition for the

110 intermetallic TiFe. The grey phase (Spectrum 3) presents a composition close to Ti_2Fe and the
 111 dark-grey phase (Spectrum 4) is Ti-rich.

112

113 Figure 2 shows the XRD patterns of the $Ti_{1.2}Fe_{0.8}$ alloy in the as-cast condition. The phases
 114 identified are TiFe, Ti_2Fe and BCC. By correlating the phases identified by EDX, it can be assumed
 115 that the main region, grey region, and dark-grey region respectively correspond to TiFe, Ti_2Fe and
 116 BCC phases. Table 2 presents the results from the Rietveld refinement performed on the as-cast
 117 condition. The abundances of each phase from image analysis are included for comparison. The
 118 phase abundance on the refinement results is higher than the one measured by image analysis.
 119 However, it is important to keep in mind that Rietveld refinement reports the wt.%. If the phase
 120 fraction measured by image analysis is multiplied by the density of each phase ($TiFe\rho = 6.6\text{ g/cm}^3$,
 121 $Ti_2Fe\rho = 5.7\text{ g/cm}^3$, $BCC\rho(Ti_{18}\%Fe_{20}\%) = 5.2\text{ g/cm}^3$) and each result is divided by the sum, the
 122 phase fraction obtained is 63 wt.% TiFe, 11 wt.% Ti_2Fe and 26 wt.% BCC. This is an almost exact
 123 match to the Rietveld refinement.

124



125

126

Figure 2. X-ray diffraction patterns of the induction melted $Ti_{1.2}Fe_{0.8}$.

127

128

129

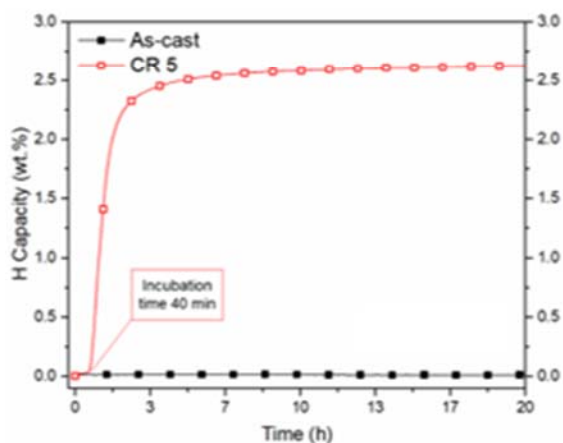
130 **Table 2.** Rietveld refinement of the as-cast induction melted $Ti_{1.2}Fe_{0.8}$ (the uncertainty on
131 the last significant digit is given by the number in parentheses).

Phase	Phase Fraction Image analysis (area %)	Phase Fraction Rietveld Refinement (wt.%)	Lattice parameters "a" (Å)
TiFe	58	64	2.9904 (2)
Ti ₂ Fe	12	10	11.328 (1)
BCC	30	26	3.1850 (3)

132

133 Figure 3 shows the activation curves of the $Ti_{1.2}Fe_{0.8}$ alloy. The as-cast sample did not
134 activate after over 20 hours under 2000 kPa of hydrogen pressure. The sample that was cold rolled
135 5 times in air (CR5) presented a fast activation kinetics reaching ~2.6 wt.% H with an incubation
136 period of ~40 minutes and saturation in ~6 hours.

137



138

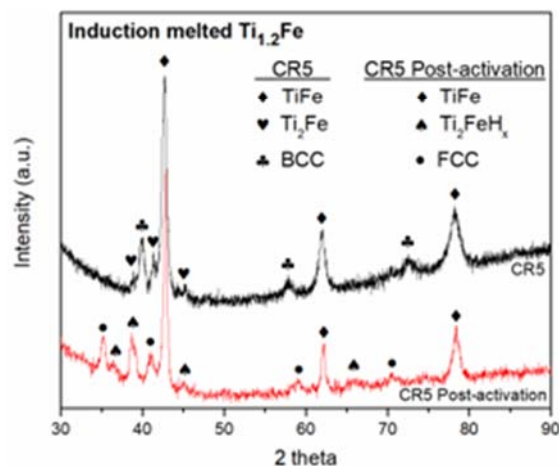
139 **Figure 3.** Activation curve of $Ti_{1.2}Fe_{0.8}$ with and without cold rolling.

140

141 Figure 4 shows the XRD patterns of the CR5 $Ti_{1.2}Fe_{0.8}$ alloy before and after activation. The
142 phases identified after cold rolling match those identified in the as-cast condition (TiFe, Ti₂Fe and
143 BCC) with the difference that the peaks are slightly broader, which is typical for samples that have
144 undergone mechanical deformation. The phases identified after activation are TiFe, Ti₂FeH_x and
145 FCC (Face Centered Cubic). The hydride phases Ti₂FeH_x and FCC are both stable hydrides formed

146 during activation. It is well known that the dihydride of a BCC phase is FCC. Thus, the origin of
 147 the FCC could be directly related to the presence of a BCC phase in the as-cast alloy. The stable
 148 hydrides identified match those previously reported on TiFe-based alloys with Ti
 149 overstoichiometry [26, 28].

150



151

152 **Figure 4.** X-ray diffraction patterns of the cold rolled 5 times CR5 induction melted $Ti_{1.2}Fe_{0.8}$
 153 alloys before and after activation.

154

155 Table 3 shows the crystal structure parameters of the refined Ti_2Fe and Ti_2FeH_x respectively
 156 for the CR5 before and after activation. The volume expansion of the Ti_2Fe phase in the CR5 post-
 157 activation condition was determined to be 21%. This expansion is close to the ones previously
 158 reported by Faisal et al. [21]. They reported the hydrogen storage behavior of a minor $(Ti,Zr)_2-Fe$
 159 phase present in two alloys by measuring a volume expansion of 16.4% and 24.4%. The
 160 stoichiometry of the Ti_2FeH_x was determined by the unit cell volume increase. The volume
 161 increase is 305 \AA^3 , since there are 32 formula units per unit cell, this gives a volume per formula
 162 unit of 9.5 \AA^3 . Assuming that a single hydrogen atom usually occupies a volume between 2 and 3
 163 \AA^3 , this gives a range of stoichiometry between $Ti_2FeH_{4.75}$ (3.09 wt.% H) and $Ti_2FeH_{3.2}$ (2.08 wt.%
 164 H).

165

166 **Table 3.** Crystal structure parameters of Ti_2Fe and Ti_2FeH_x phases identified in figure 4 (the
 167 uncertainty on the last significant digit is given by the number in parentheses).

CR5			CR5 Post-activation		
Phase	Lattice parameters (Å)	Unit cell volume (Å ³)	Phase	Lattice parameters (Å)	Unit cell volume (Å ³)
Ti_2Fe	11.320(3)	1451(1)	Ti_2FeH_x	12.064(5)	1756(2)

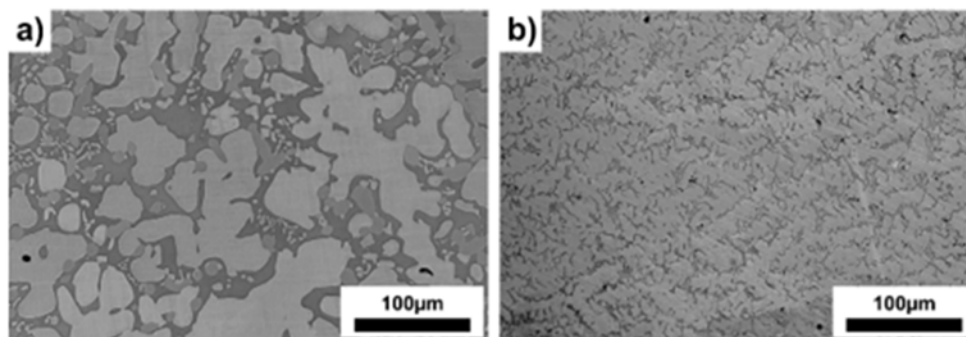
168

169 Now considering the phase fractions obtained by Rietveld refinement in table 2, the
 170 theoretical composition for $TiFe$ (1.86 wt.% H), FCC (3.7 wt.% H) and the stoichiometry
 171 calculated by unit cell volume increase for Ti_2FeH_x , the hydrogen intake contribution during
 172 activation of each phase can be calculated as follows: the 64% of $TiFe$ would contribute 1.19 wt.%
 173 H, the 10% of Ti_2FeH_x between 0.2 – 0.3 wt.% H and the 26% of BCC – 0.96 wt.% H, for a total
 174 of 2.35 – 2.45 wt.% H. These results are not far off from the 2.6 wt.% H measured during
 175 activation. The effect of the absorption of each phase is not seen in the activation curve, meaning
 176 that in figure 3 the activation curve presents only one slope. This points to the system acting as a
 177 single phase.

178

179 To see the effect of the microstructure, a small 3 g sample of $Ti_{1.2}Fe_{0.8}$ was prepared by arc-
 180 melting. Figure 5 shows a side-by-side comparison of the microstructure obtained by induction
 181 melting (a) and arc-melting (b). It is clear from the image analysis of figure 5 that the arc-melted
 182 sample presents a much finer microstructure with a higher area abundance of the bright main phase,
 183 77 % compared to the 58 % measured for the induction melted sample.

184



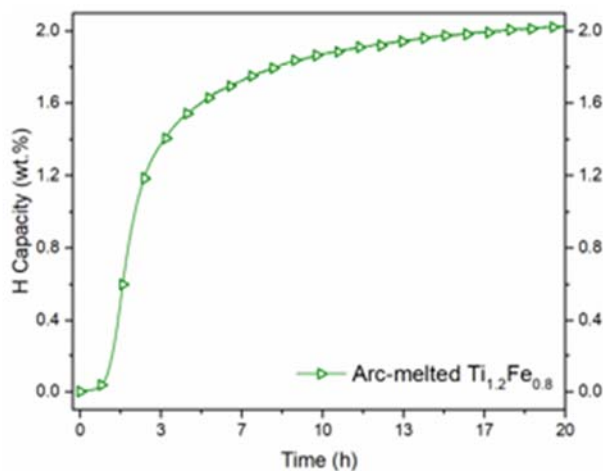
185

186 **Figure 5.** Backscattered electron images of induction melted (a) and arc-melted (b) $Ti_{1.2}Fe_{0.8}$.

187

188 Figure 6 shows the activation curve of the arc-melted sample. It activated without the need
 189 of any heat treatment or mechanical processing, reaching a capacity of 2 wt.% H in ~12 hours. The
 190 ability to activate without the need for cold rolling is attributed to the fine microstructure generated
 191 by arc-melting. Nevertheless, the presence of the secondary phases is essential for activation
 192 without heat treatment.

193



194

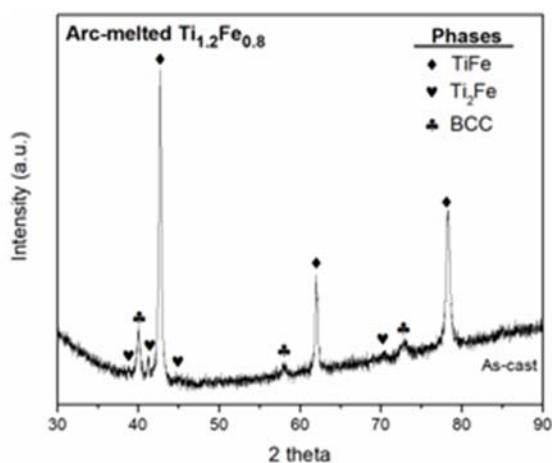
195

196 **Figure 6.** Activation curve of the arc-melted $Ti_{1.2}Fe_{0.8}$.

196

197 Figure 7 shows the XRD patterns of the arc-melted $Ti_{1.2}Fe_{0.8}$ alloy. The phases identified are
 198 TiFe, Ti_2Fe and BCC, matching those in the induction melted condition. The phase fractions

199 obtained by Rietveld refinement are 80 wt.% TiFe, 4 wt.% Ti₂Fe and 16 wt.% BCC. This shows
 200 how lower percentages of the secondary phases can be enough to achieve activation under mild
 201 conditions if the microstructure presents a finer scale. Regarding the difference in H capacity
 202 between the induction-melted sample (2.6 wt.% H) and the arc-melted sample (2 wt.% H) this is
 203 due to the difference in phase fraction of secondary phases. However most importantly is the phase
 204 fraction of TiFe which is the phase that ultimately provides reversible hydrogenation behavior.
 205 Therefore, the reversible capacity of the induction-melted sample is thought to be 1.19 wt.% H (64
 206 % TiFe) and 1.49wt.% for the arc-melted sample (80% TiFe).
 207



208

209 **Figure 7.** X-ray diffraction patterns of the induction melted $Ti_{1.2}Fe_{0.8}$.

210

211

212 Conclusions

213

- 214 • $Ti_{1.2}Fe_{0.8}$ forms secondary phases with the same crystal structure (Ti₂Fe and BCC) as those reported when alloying TiFe with Zr and Mn.
- 215 • Induction melted $Ti_{1.2}Fe_{0.8}$ alloy requires cold rolling to activate under mild conditions. It then reaches a capacity of 2.6 wt.% H with good kinetics. Arc-melted $Ti_{1.2}Fe_{0.8}$ sample was able to activate without the need for mechanical processing reaching 2.0 wt.% H in ~12 h.
- 217 • The three-phase system (TiFe, Ti₂Fe and BCC) activates as a single-phase system regardless of the formation of two stable hydrides (Ti₂FeH_x and FCC).

218

219

220 Acknowledgements

221

222 Ulate-Kolitsky E. would like to acknowledge the student grant provided by the Réseau
223 Québécois sur l'Énergie Intelligente (RQEI).

224

225 References

226

- 227 [1] J. Bellosta von Colbe *et al.*, "Application of hydrides in hydrogen storage and compression:
228 Achievements, outlook and perspectives," *International Journal of Hydrogen Energy*, vol.
229 44, no. 15, pp. 7780-7808, 2019.
- 230 [2] G. K. Sujan, Z. Pan, H. Li, D. Liang, and N. Alam, "An overview on TiFe intermetallic for
231 solid-state hydrogen storage: microstructure, hydrogenation and fabrication processes,"
232 *Critical Reviews in Solid State and Materials Sciences*, pp. 1-18, 2019.
- 233 [3] J. J. Reilly and R. H. Wiswall, "Formation and properties of iron titanium hydride,"
234 *Inorganic Chemistry*, vol. 13, no. 1, pp. 218-222, 1974/01/01 1974.
- 235 [4] P. Lv, M. N. Guzik, S. Sartori, and J. Huot, "Effect of ball milling and cryomilling on the
236 microstructure and first hydrogenation properties of TiFe+4 wt.% Zr alloy," *Journal of*
237 *Materials Research and Technology*, vol. 8, no. 2, pp. 1828-1834, 2019.
- 238 [5] R. A. Silva *et al.*, "Room temperature hydrogen absorption by Mg and Mg TiFe
239 nanocomposites processed by high-energy ball milling," *International Journal of*
240 *Hydrogen Energy*, vol. 43, no. 27, pp. 12251-12259, 2018.
- 241 [6] R. B. Falcão *et al.*, "An alternative route to produce easily activated nanocrystalline TiFe
242 powder," *International Journal of Hydrogen Energy*, vol. 43, no. 33, pp. 16107-16116,
243 2018.
- 244 [7] F. Guo, K. Namba, H. Miyaoka, A. Jain, and T. Ichikawa, "Hydrogen storage behavior of
245 TiFe alloy activated by different methods," *Materials Letters: X*, vol. 9, 2021, doi:
246 10.1016/j.mlblux.2021.100061.
- 247 [8] E. Ulate-Kolitsky, B. Tougas, B. Neumann, C. Schade, and J. Huot, "First hydrogenation
248 of mechanically processed TiFe-based alloy synthesized by gas atomization," *International*
249 *Journal of Hydrogen Energy*, vol. 46, no. 10, pp. 7381-7389, 2021, doi:
250 10.1016/j.ijhydene.2020.11.237.

- 251 [9] L. E. R. Vega *et al.*, "Mechanical activation of TiFe for hydrogen storage by cold rolling
252 under inert atmosphere," *International Journal of Hydrogen Energy*, vol. 43, no. 5, pp.
253 2913-2918, 2018.
- 254 [10] K. Edalati, J. Matsuda, A. Yanagida, E. Akiba, and Z. Horita, "Activation of TiFe for
255 hydrogen storage by plastic deformation using groove rolling and high-pressure torsion:
256 Similarities and differences," *International Journal of Hydrogen Energy*, vol. 39, no. 28,
257 pp. 15589-15594, 2014.
- 258 [11] K. Edalati, J. Matsuda, M. Arita, T. Daio, E. Akiba, and Z. Horita, "Mechanism of
259 activation of TiFe intermetallics for hydrogen storage by severe plastic deformation using
260 high-pressure torsion," *Applied Physics Letters*, vol. 103, no. 14, 2013, doi:
261 10.1063/1.4823555.
- 262 [12] V. B. Oliveira *et al.*, "Hydrogen Absorption/Desorption Behavior of a Cold-Rolled TiFe
263 Intermetallic Compound," *Materials Research*, vol. 24, no. 6, 2021, doi: 10.1590/1980-
264 5373-mr-2021-0204.
- 265 [13] C. Gosselin and J. Huot, "Hydrogenation Properties of TiFe Doped with Zirconium," (in
266 eng), *Materials (Basel)*, vol. 8, no. 11, pp. 7864-7872, Nov 20 2015.
- 267 [14] C. Gosselin and J. Huot, "First Hydrogenation Enhancement in TiFe Alloys for Hydrogen
268 Storage Doped with Yttrium," *Metals*, vol. 9, no. 2, 2019.
- 269 [15] P. Lv, Z. Liu, and V. Dixit, "Improved hydrogen storage properties of TiFe alloy by doping
270 (Zr+2V) additive and using mechanical deformation," *International Journal of Hydrogen
271 Energy*, vol. 44, no. 51, pp. 27843-27852, 2019.
- 272 [16] W. Ali *et al.*, "Hydrogenation properties of Ti-Fe-Mn alloy with Cu and Y as additives,"
273 *International Journal of Hydrogen Energy*, vol. 42, no. 4, pp. 2229-2238, 2017, doi:
274 10.1016/j.ijhydene.2016.09.037.
- 275 [17] H. Leng *et al.*, "Effect of cobalt on the microstructure and hydrogen sorption performances
276 of TiFe_{0.8}Mn_{0.2} alloy," *International Journal of Hydrogen Energy*, vol. 45, no. 38, pp.
277 19553-19560, 2020.
- 278 [18] H. Leng, Z. Yu, J. Yin, Q. Li, Z. Wu, and K.-C. Chou, "Effects of Ce on the hydrogen
279 storage properties of TiFe_{0.9}Mn_{0.1} alloy," *International Journal of Hydrogen Energy*,
280 vol. 42, no. 37, pp. 23731-23736, 2017.

- 281 [19] T. Yang *et al.*, "Effect of chromium, manganese and yttrium on microstructure and
282 hydrogen storage properties of TiFe-based alloy," *International Journal of Hydrogen*
283 *Energy*, vol. 45, no. 21, pp. 12071-12081, 2020.
- 284 [20] K. B. Park *et al.*, "Effect of Fe substitution by Mn and Cr on first hydrogenation kinetics
285 of air-exposed TiFe-based hydrogen storage alloy," *Materials Characterization*, vol. 178,
286 2021, doi: 10.1016/j.matchar.2021.111246.
- 287 [21] M. Faisal, J.-Y. Suh, and Y.-S. Lee, "Understanding first cycle hydrogenation properties
288 of Ti-Fe-Zr ternary alloys," *International Journal of Hydrogen Energy*, vol. 46, no. 5, pp.
289 4241-4251, 2021, doi: 10.1016/j.ijhydene.2020.11.025.
- 290 [22] L. Zeng, G. Xu, L. Liu, W. Bai, and L. Zhang, "Experimental investigation of phase
291 equilibria in the Ti-Fe-Zr system," *Calphad*, vol. 61, pp. 20-32, 2018, doi:
292 10.1016/j.calphad.2018.02.005.
- 293 [23] T. Velikanova and K. Korniyenko, "Iron – Titanium – Zirconium," in *Iron Systems, Part*
294 *5*, (Landolt-Börnstein - Group IV Physical Chemistry, 2009, ch. Chapter 34, pp. 702-720.
- 295 [24] G. Zhou, D. Zeng, and Z. Liu, "Phase equilibria in the Fe-Ti-Zr system at 1023K," *Journal*
296 *of Alloys and Compounds*, vol. 490, no. 1-2, pp. 463-467, 2010, doi:
297 10.1016/j.jallcom.2009.10.046.
- 298 [25] A. K. Patel, A. Duguay, B. Tougas, C. Schade, P. Sharma, and J. Huot, "Microstructure
299 and first hydrogenation properties of TiFe alloy with Zr and Mn as additives," *International*
300 *Journal of Hydrogen Energy*, 2019.
- 301 [26] E. Ulate-Kolitsky, B. Tougas, and J. Huot, "Hydrogenation of Ti_xFe_{2-x} -based alloys with
302 overstoichiometric Ti ratio ($x = 1.1, 1.15$ and 1.2)," *International Journal of Hydrogen*
303 *Energy*, vol. 46, no. 77, pp. 38363-38369, 2021, doi: 10.1016/j.ijhydene.2021.09.077.
- 304 [27] J. Manna, B. Tougas, and J. Huot, "First hydrogenation kinetics of Zr and Mn doped TiFe
305 alloy after air exposure and reactivation by mechanical treatment," *International Journal*
306 *of Hydrogen Energy*, 2020.
- 307 [28] K. B. Park *et al.*, "Characterization of microstructure and surface oxide of $Ti_{1.2}Fe$
308 hydrogen storage alloy," *International Journal of Hydrogen Energy*, vol. 46, no. 24, pp.
309 13082-13087, 2021, doi: 10.1016/j.ijhydene.2021.01.105.
- 310 [29] TOPAS. (2021). Bruker, Alan A. Coelho, V6.

Declaration of Interest Statement (use official Word Template)

Declaration of interests

The authors declare that they have no known competing financial interests or personal relationships that could have appeared to influence the work reported in this paper.

The authors declare the following financial interests/personal relationships which may be considered as potential competing interests: